

Threshold-Switchable Particles to Treat Internal Hemorrhage

By:

Alexander John Donovan

B.S., Biological Chemistry; B.A., Chemistry; University of Chicago, Chicago, IL 2008

Thesis

Submitted in Partial Fulfillment of the Requirements

For the Degree of Doctor of Philosophy in Chemical Engineering

In the Graduate College of the

University of Illinois at Chicago, 2017

Defense Committee:

Ying Liu, Chair and Advisor

Vikas Berry

Vivek Sharma

Xiaoping Du, Department of Pharmacology

Ursula Perez-Salas, Department of Physics

ACKNOWLEDGEMENTS

I am forever indebted to my advisor Prof. Ying Liu for her extraordinary mentorship, counsel, and support throughout my tenure at UIC. She has tirelessly promoted my curiosity for chemical engineering research, as well as related interests in intellectual property, technical writing, and entrepreneurship. Thanks to her stewardship, she has allowed me opportunities and equipped me with the knowledge and skills that I never would have imagined I would gain.

Secondly, I would like to graciously thank my thesis committee: Prof. Ying Liu, Prof. Vikas Berry, Prof. Xiaoping Du, Prof. Vivek Sharma, and Prof. Ursula Perez-Salas, who have allowed my knowledge to flourish with their formidable intellectual presence, exceptional advisement, and encouraging dialogue.

In addition, I am greatly indebted to everyone who participated in the five-year DoD-sponsored TSP collaboration, including Prof. James H. Morrissey and Dr. Stephanie A. Smith at UIUC, Prof. Rustem Ismagilov at CalTech, Prof. Galen Stucky at UCSB, and Prof. Christian J. Kastrup at UBC Vancouver, for stimulating discussion and supplying constructive criticisms of new research findings during monthly Skype meetings, being exceptional hosts for important clotting experiments, and contributing their unrivaled knowledge to the composition of several manuscripts. Likewise, I am grateful to Profs. Xiaoping Du (UIC Pharmacology), Lijun Rong (UIC Immunology), and Vivek Sharma for challenging discussions and providing valuable resources for experiments.

Moreover, I owe tremendous gratitude to Magdalena Szymusiak, Hao Shen, Vishal Sharma, Ross Ransom, Joseph Kalkowski, Catalina Mogollon, Tiep Pham, Chang Liu, Pin Zhang and all of the other Liu Group members, past and present, who have participated in both the most exciting moments of research and its most trying.

Development of a threshold-switchable procoagulant nanoparticle employing inorganic polyphosphate was sponsored by the US Army Medical Research and Materiel Command (WQ81XWH-11-2-0021). The U.S. Army Medical Research Acquisition Activity, 820 Chandler Street, Fort Detrick MD 21702-5014 is the awarding and administering acquisition office. HR-STEM and EELS characterization of ADGs made use of the JEOL JEM-ARM200CF in the Electron Microscopy Service (Research Resources Center, UIC). The acquisition of the UIC JEOL JEM-ARM200CF was supported by a MRI-R2 grant from the National Science Foundation [DMR-0959470]. The contents of this thesis do not necessarily reflect the position or the policy of the government, and no official endorsement should be inferred.

CONTRIBUTION OF AUTHORS

Chapter 1 underscores the challenges in developing a universal, on-demand hemostatic agent, and the promise which lies in utilizing nanotechnology tools to develop an arsenal with tailored or stimuli responsive characteristics for hemorrhagic therapy. **Chapter 2**, in large part, was originally published as A.J. Donovan, J. Kalkowski, S.A. Smith, J.H. Morrissey, and Y. Liu. “Size-controlled synthesis of granular polyphosphate nanoparticles at physiologic salt concentrations for blood clotting.” *Biomacromolecules*, **2014**, 15 (11): 3976-3984. The author of this dissertation contributed substantially to the design and implementation of experiments in addition to the composition of the manuscript. **Chapter 3**, in large part, was also published previously as A.J. Donovan, J. Kalkowski, M. Szymusiak, C. Wang, S.A. Smith, R.F. Klie, J.H. Morrissey, and Y. Liu. “Artificial dense granules: a procoagulant liposomal formulation modeled after platelet polyphosphate storage pools.” *Biomacromolecules* **2016**, 17(8): 2572-2581. The experiments were principally devised and performed by the author of the dissertation, and the manuscript was largely written by him. **Chapter 4** discusses preliminary results relating to employing inorganic polyphosphate (polyP) to form polyelectrolyte complex coacervates for protein delivery, with Factor VIII (FVIII) and bovine serum albumin (BSA) data presented. **Chapter 5** offers a practical experimental trajectory for developing an antihemorrhagic medicine from artificial platelet dense granules (ADGs). **Chapter 6** provides a summary of the development of a prospective threshold-switchable procoagulant agent, and the obstacles remaining toward the emergence of a veritable, on-demand hemostatic agent. Unless otherwise noted above, Alexander J. Donovan is the sole author of this dissertation.

TABLE OF CONTENTS

ACKNOWLEDGEMENTS.....	ii
CONTRIBUTION OF AUTHORS.....	iv
TABLE OF CONTENTS.....	v
LIST OF TABLES.....	ix
LIST OF FIGURES.....	x
LIST OF ABBREVIATIONS.....	xi
SUMMARY.....	xvi
CHAPTER 1. INTRODUCTION.....	1
1.1 An Urgent, Unmet Need for an Effective Therapy for Incompressible Hemorrhage.....	1
1.2 The Blood Coagulation Cascade.....	5
1.2.1 The Tissue Factor Pathway of Blood Coagulation.....	6
1.2.2 The Contact Pathway of Blood Coagulation.....	6
1.2.3 The Common Pathway of Blood Coagulation.....	7
1.3 Current Treatment Options.....	9
1.4 Inorganic Polyphosphate (PolyP)'s Role in Blood Clotting.....	11
1.5 Nanotherapeutic Platforms.....	14
1.5.1 Lipid Based Platforms.....	15
1.5.1.1 Liposomes.....	15
1.5.2 Polymeric Nanoparticles.....	17
1.6 Experimental Techniques.....	18
1.6.1 Dynamic Light Scattering (DLS).....	18
1.6.2 Transmission Electron Microscopy (TEM).....	20
1.6.3 Biocompatible High Resolution Scanning Transmission Electron Microscopy (HR-STEM).....	20

CHAPTER 2. THERMODYNAMIC SELF-ASSEMBLY OF INORGANIC POLYPHOSPHATE GRANULES IN AQUEOUS ELECTROLYTE SOLUTIONS.....	21
2.1 Introduction.....	22
2.2 Experimental Section.....	23
2.2.1 <i>Materials & Reagents.....</i>	23
2.2.2 <i>PolyP nanoprecipitation.....</i>	24
2.2.3 <i>Determination of PolyP Solubility.....</i>	24
2.2.4 <i>PolyP Nanoparticle (NP) Stability.....</i>	24
2.2.4.1 <i>Stability in Aqueous Buffer.....</i>	24
2.2.4.2 <i>Stability in BSA Suspensions.....</i>	25
2.2.5 <i>Complex Coacervation of polyP and BSA.....</i>	25
2.2.6 <i>Turbidometric measurements for polyP-BSA Complexes.....</i>	25
2.2.7 <i>Transmission Electron Microscopy.....</i>	26
2.2.7.1 <i>Sample Preparation.....</i>	26
2.2.8 <i>Preparation of Large Unilamellar Vesicles (LUV) for Clotting Assays.....</i>	26
2.2.9 <i>Clotting Assays.....</i>	27
2.3 Results and Discussion.....	27
2.4 Conclusion.....	66
CHAPTER 3. BIOINSPIRED ARTIFICIAL PLATELET NANOPARTICLES.....	67
3.1 Introduction.....	67
3.2 Experimental Section.....	70
3.2.1 <i>Materials and reagents.....</i>	70
3.2.2 <i>Synthesis of Sterically Stabilized Liposomes.....</i>	70
3.2.3 <i>Synthesis of ADGs.....</i>	71
3.2.4 <i>FXII Autoactivation Assay with Detergent.....</i>	71

3.2.5 FXII Autoactivation Assay with PLC from <i>C. welchii</i>	71
3.2.6 Determination of PolyP NP Encapsulation Efficiency.....	72
3.2.7 Monitoring Digestion of ADGs by bvsPLA ₂ and PLC via DLS.....	72
3.2.8 ADG Contact Activity in Human Plasma.....	72
3.2.9 Conventional Transmission Electron Microscopy.....	73
3.2.9.1 Sample Preparation.....	73
3.2.9.2 High-Resolution Scanning Transmission Electron Microscopy (HR-STEM).....	73
3.3 Results and Discussion.....	74
3.4 Conclusion.....	106
CHAPTER 4. INORGANIC POLYPHOSPHATE FOR GENERIC PROTEIN DELIVERY.....	108
4.1 Introduction.....	108
4.2 Experimental Section.....	110
4.2.1 Materials and Reagents.....	110
4.2.2 Co-nanoprecipitation of PolyP and FVIII.....	111
4.2.3 Synthesis of DLPC/DPPC/PEG _{2k} DPPE Liposomes.....	111
4.2.4 Encapsulation of polyP-FVIII NPs in Sterically Stabilized Liposomes.....	112
4.2.5 Ultracentrifugation of ADG/FVIII NPs.....	112
4.2.6 FVIII Encapsulation Efficiency.....	112
4.2.7 Microplate-Based Clotting Assay in FVIII-Deficient Human Plasma with PLC...112	
4.3 Results and Discussion.....	113
4.4 Conclusion & Future Directions.....	122
CHAPTER 5. FUTURE DIRECTIONS TOWARD A BIOINSPIRED NANOPARTICLE HEMOSTAT.....	124
5.1 Introduction.....	124

5.2. Synthesis of Novel ADG Iterations.....	125
5.2.1 Improve ADG Structural Integrity.....	125
5.2.2 Enhance Homing to the Injury Site & Promoting Synergistic Activity with Human Platelets.....	127
5.2.3 Encapsulation of Small Molecules, Peptides, and Proteins to Enhance Procoagulant Effect.....	129
5.3 Assaying Hemostatic Efficacy in More Complex Models of Traumatic Hemorrhage.....	130
5.3.1 In Vitro Clotting Assays.....	130
5.3.2 Animal Models of Internal Hemorrhage.....	132
5.4 Conclusion.....	133
CHAPTER 6. CONCLUSIONS.....	135
VITA.....	138
COPYRIGHT PERMISSIONS.....	139
REFERENCES.....	141

LIST OF TABLES

CHAPTER 1 INTRODUCTION

CHAPTER 2 THERMODYNAMIC SELF-ASSEMBLY OF INORGANIC POLYPHOSPHATE GRANULES IN AQUEOUS ELECTROLYTE SOLUTIONS

Table 2.1 The solubilities of PolyP in 5 mM CaCl₂ (aq) based on pH and polymer length.....33

Table 2.2 Absence of multiple scattering effects in BSA suspensions containing PolyP.....42

Table 2.3 PolyP250 NP effective diameter is hysteretic.....50

Table 2.4 Average zeta potential and effective diameter of PolyP NPs precipitated at 125 μM monoP in 5 mM CaCl₂, 8 mM Tris·HCl, pH 7.4.....61

Table 2.5 Average zeta potential and effective diameter of 125 μM PolyP1000+ NPs synthesized at various precipitating conditions.....61

CHAPTER 3 BIONSPIRED ARTIFICIAL PLATELET NANOPARTICLES

CHAPTER 4 INORGANIC POLYPHOSPHATE FOR GENERIC PROTEIN DELIVERY APPLICATIONS

Table 4.1. Centrifugation parameters for removing free FVIII from ADG-FVIII NPs....117

CHAPTER 5 FUTURE DIRECTIONS TOWARD A BIOINSPIRED NANOPARTICLE HEMOSTAT

Table 5.1 ADG coagulometric experiments.....132

CHAPTER 6 CONCLUSIONS

LIST OF FIGURES

CHAPTER 1 INTRODUCTION

Figure 1.1 The Contact and Tissue Factor Pathways of Blood Coagulation.....8

Figure 1.2 Nanotherapeutic Platforms.....13

CHAPTER 2 THERMODYNAMIC SELF-ASSEMBLY OF INORGANIC POLYPHOSPHATE GRANULES IN AQUEOUS ELECTROLYTE SOLUTIONS

Figure 2.1. The precipitative effects of different metal cations on very long chain polyP.....28

Figure 2.2. 5 mM CaCl_2 yields divergent precipitative effects on polyP depending on the polymer length29

Figure 2.3. Solubility of polyP of different polymer lengths30

Figure 2.4. Scattering intensity of heterodisperse, platelet-sized polyP (“BKGP70,” range 20-125 phosphate units) in 5 mM CaCl_2 at pH 5.4 and 7.4.....33

Figure 2.5. PolyP250 nanoparticle stability in aqueous buffer34

Figure 2.6. PolyP250 nanoparticle stability in suspensions containing BSA.....35

Figure 2.7 Lognormal size distributions for (1) BSA suspension without Ca^{2+} pretreatment; (2) BSA suspension with 1.2 mM CaCl_2 ; (3) immediate addition of polyP 250 NPs in 35 mg/ml BSA without CaCl_2 pre-equilibration; and (4) immediate addition of polyP 250 NPs in 35 mg/ml BSA with 1.2 mM CaCl_236

Figure 2.8. Stability of polyP1000+ NPs in acidic and basic conditions38

Figure 2.9. Scattering count rates at pH 5.4 and 7.4.....39

Figure 2.10. Polydispersity index of polyP1000+ NPs at pH 5.4 and 7.4.....40

Figure 2.11. Hydrodynamic diameter of polyP-BSA complexes at various polyP45:BSA molar ratios.....44

Figure 2.12. PolyP-BSA complex optical turbidity at 405 nm (A_{405}) for various polyP:BSA ratios.....45

Figure 2.13. PolyP250 NP initial effective diameter versus monoP and Ca^{2+} Concentrations.....47

Figure 2.14. PolyP250 NP initial effective diameter as a function of supersaturation ratios and Ca^{2+} concentrations.....	48
Figure 2.15. PolyP NP solubility hysteresis.....	49
Figure 2.16. PolyP NP morphology, structure & elemental composition.....	52
Figure 2.17. PolyP NPs as contact activators.....	55
Figure 2.18. Lognormal particle size distribution of polyP1000+ in 5 mM Mg^{2+} only.....	58
Figure 2.19. Particle size distribution of polyP1000+ precipitates in $\text{Fe}^{2+}/\text{Fe}^{3+}$	59
Figure 2.20. Initiation of the contact pathway by polyP based on polymer length and concentration.....	63
Figure 2.21. A: Microfluidic device for measuring procoagulant behavior of polyP NPs at physiologic and pathophysiologic shear rates ($1\text{-}128\text{ s}^{-1}$) simultaneously.....	64
CHAPTER 3 BIONSPIRED ARTIFICIAL PLATELET NANOPARTICLES	
Figure 3.1 ADG design and structure.....	74
Figure 3.2 ADG morphology: core-shell structure and elemental composition.....	75
Figure 3.3 TEM of ADGs and artificial acidocalcisomes.....	77
Figure 3.4 HAADF images of the ADGs (1-3), as well as the bare particles (4-6) protected by the graphene sandwich approach.....	79
Figure 3.5 Intensity-weighted, lognormal particle size distribution of ADGs by DLS prepared for HR-STEM.....	81
Figure 3.6. Scattering intensity of ADGs after phospholipase digestion.....	82
Figure 3.7 Stability of ADGs in suspension.....	83
Figure 3.8 Verification of the ADG encapsulation efficiency by measuring ADG diameter shifts after exposure to detergent and changes in calcium concentration.....	84
Figure 3.9. Colloidal stability of granular polyP NPs in the presence of non-ionic detergent.....	86
Figure 3.10. Illustration of phospholipase-induced degradation of the lipid envelope.....	88

Figure 3.11. Autoactivation of FXII zymogen via detergent-triggered solubilization of ADG vesicular envelope	89
Figure 3.12. FXII autoactivation after ADG preincubation with PLC.....	90
Figure 3.13. FXII autoactivity assay of bare polyP NPs	93
Figure 3.14: PLC concentration dependence of ADG-induced FXII autoactivity. A: ADGs pre-incubated with increasing amounts of PLC	94
Figure 3.15 : Empty sterically stabilized liposomes in the presence of phospholipase.....	95
Figure 3.16. Subthreshold phospholipase concentrations do not trigger ADG-induced FXII zymogen conversion.....	96
Figure 3.17. Mean particle diameter of platelet-sized polyP NPs precipitated in 1.5 mM CaCl_2 , 10 μM ZnCl_2 , conditions mimicking the ionic concentrations for the FXII autoactivation assay, at nearly neutral and slightly acidic pH.....	99
Figure 3.18. Scattering intensity of $\text{Ca}^{2+}/\text{Zn}^{2+}$ -polyP NPs at physiologic and dense-granular pH environments.....	100
Figure 3.19. Colloidal stability of ADGs and empty liposomes in 35 mg/ml BSA, 1.2 mM Ca^{2+} , approximating the solvent environment of human blood plasma.....	102
Figure 3.20 Trimodal particle size distributions of ADGs and empty liposomes 40 min after addition to the BSA suspension.....	103
Figure 3.21. Contact activity of ADGs in human plasma. A: Absolute clotting time in human plasma.....	104
Figure 3.22. Clotting times given as percent reduction from the control.....	105
CHAPTER 4 INORGANIC POLYPHOSPHATE FOR GENERIC PROTEIN DELIVERY APPLICATIONS	
Figure 4.1. Colloidal stability of bare polyP-FVIII and ADG-FVIII NPs in 5 mM CaCl_2	114
Figure 4.2 Free un-encapsulated FVIII in ADG-FVIII NPs Suspensions Determined by Bradford Assay	115
Figure 4.3 Free un-encapsulated FVIII in ADG-FVIII NPs Suspensions Determined by Bradford Assay.....	118

Figure 4.4. Clotting activity of ADG-FVIII NPs before centrifugation (ADG-FVIII BC) in FVIII-Deficient plasma after PLC digestion.....119

Figure 4.5. Clotting activity of ADG-FVIII NPs after centrifugation (ADG-FVIII AC) in FVIII-deficient plasma after PLC digestion.....120

CHAPTER 5 FUTURE DIRECTIONS TOWARD A BIOINSPIRED NANOPARTICLE HEMOSTAT

CHAPTER 6 CONCLUSIONS

ABBREVIATIONS

NP.....	Nanoparticle
polyP.....	Inorganic polyphosphate
ADG.....	Artificial dense granule
PEG.....	Poly(ethylene glycol)
L- α -PC.....	L- α -phosphatidylcholine
DLS.....	Dynamic light scattering
cmc.....	critical micelle concentration
TEM.....	Transmission electron microscopy
STEM.....	Scanning transmission electron microscopy
EELS.....	Electron energy loss spectroscopy
BSA.....	Bovine serum albumin
LUV.....	Large unilamellar vesicle
PNP.....	Pooled normal plasma
FV.....	Factor V zymogen
FVa.....	Activated Factor V
FVIII.....	Factor VIII zymogen
FVIIIa.....	Activated Factor VIII
FX.....	Factor X zymogen
FXa.....	Activated Factor X
FXI.....	Factor XI zymogen
FXIa.....	Activated Factor XI
FXII.....	Factor XII zymogen
FXIIa.....	Activated FXII
sPLA ₂	Secreted phospholipase A ₂

PLC.....Phospholipase C
bvsPLA₂.....Secreted phospholipase A₂ from honey bee venom

SUMMARY

An artificial platelet nanotechnology with threshold-switchable procoagulant functionality is devised, employing one of the human body's intrinsic hemostatic agents, inorganic polyphosphate (polyP). Inspired by the manner in which the anionic polyelectrolyte is stored in human platelets and how it exerts its hemostatic effects, polyP is nanoprecipitated in aqueous, polyvalent metal salt solutions. The particle formation is characterized by dynamic light scattering (DLS), and the particle morphology, structure, and elemental composition is determined by transmission electron microscopy (TEM) and energy-dispersive X-Ray spectroscopy (EDS). The ability for the polyP nanoparticles (NPs) to initiate blood coagulation in human plasma is accomplished by a standard turbidometric experiment assaying for contact pathway activation, validating that polyP NPs manifest robust procoagulant ability compared against the molecularly dissolved polymers of the same molecular weight.

PolyP granules are stored in lipid bilayer shells approximately 250 nm across. These core-shell granular nanoparticles are referred to as dense granules in human platelets because of the presence of high molecular weight elements and their appearance under an electron microscope. A route to achieve a similar nanostructure is realized by brief ultrasonication of granular polyP NPs with sterically stabilized liposomes to give an Artificial Dense Granule (ADG). DLS was utilized to qualify colloidal stability and polyP encapsulation efficiency. High resolution imaging and two-dimensional spectroscopy are employed to verify the ADG core-shell structure and elemental distribution. A central design element of ADGs is to rapidly release the polyP cargo in the presence of high concentrations of phospholipase enzymes typically overexpressed in the blood stream adjacent to hemorrhagic bleeding sites. As a proof of concept,

it is demonstrated that ADGs may initiate the contact pathway of blood coagulation in isolated protein assays and in human plasma only at above-threshold enzyme concentrations.

In addition to its hemostatic functionality, polyP also serves as a generic molecular chaperone. Leveraging polyP's role as a protein binder, polyP nanoprecipitation is further investigated for its ability to assist as a protein delivery vehicle using bovine serum albumin (BSA) and recombinant human factor VIII (rFVIII) as model proteins. By two complex coacervation methods, it is shown that BSA and polyP may be forming a colloidal polyelectrolyte complex mediated by calcium cations. However, further work is necessary to confirm the resulting particle's morphology and the protein distribution.

Although the groundwork has been created for a threshold-switchable procoagulant nanoparticle, additional ADG iterations must be created that are more structurally stable and more closely mimic actual human platelets. Further, these novel prototypes must be more rigorously tested in *in vitro* models of blood clotting to include the tissue factor and common pathways of blood clotting, assayed in normal and pathophysiologic flow conditions, and in *in vivo* models of incompressible hemorrhage. A set of synthetic and experimental strategies will be presented in order to arrive at a bona fide, threshold-switchable nanoparticle hemosta

CHAPTER 1. INTRODUCTION

1.1 An Urgent, Unmet Need for an Effective Therapy for Incompressible Hemorrhage

Young adults across a spectrum of demographic groups face a significant mortality risk from traumatic injury.^{1, 2} Indeed, even in the developed world, trauma is the most probable cause of death for individuals younger than 45.¹ In especially severe scenarios, e.g. a battlefield injury or car accident, the traumatic injury results in significant hemorrhage. Without timely medical intervention to prevent or at least mitigate blood loss, patient fatality is certainly a possibility.³ Conventional corrective measures entail invasive surgical protocols in a hospital setting. Although surgery is a powerful mitigative tool to resolve hemorrhagic bleeding, the procedure requires transport to a medical facility and a trained clinician capable of performing the operation. As such, surgery often proves an ineffective intervention especially in combat scenarios with catastrophic hemorrhagic injuries, where the time window before treatment is initiated must be abbreviated as much as possible.⁴ Alternative therapies incorporating biocompatible, procoagulant polymeric materials such as HemCon® and QuikClot® into topical wound dressings have been developed to address external trauma on demand over the last decade.⁵⁻⁷ Further, recombinant proteins and clotting factors that exert procoagulant and antifibrinolytic effects, e.g. thrombin,^{8, 9} fibrinogen,¹⁰ tranexamic acid,¹¹ and recombinant Factor VIIa (rFVIIa) have been utilized as hemostatic agents. However, with the exception of rFVIIa and some coagulation factor concentrates such as Factor VIII (FVIII) and Factor IX (FIX), their use has been limited solely to external bleeding presentations. Moreover, in the case of rFVIIa, judicious monitoring by a physician is required to mitigate thromboembolic events.¹²

A burgeoning risk for military personnel in combat is trauma manifesting as incompressible and internal hemorrhage. These bleeding events are often associated with the

greatest morbidity,¹³ as current treatment regimens outside of surgery only address external injuries where external compression of the wound leads to a diminution of bleeding.¹ Therefore, there exists a public health need to develop novel procoagulant medicines with the potential to treat traumatic injuries presenting as non-compressible, internal bleeding expediently and on demand, especially when the proper resources, such as a specially equipped medical facility and trained clinicians, cannot be feasibly recruited.

Progress in drug delivery over approximately the last twenty five years, especially with its emphasis on increasingly small, engineered functional materials, has indicated that the ultimate manifestation of this succeeding generation blood clotting therapy to combat internal, incompressible hemorrhage may be a nanotechnology. The thesis of nanotherapeutics in treating human disease more effectively lies in its ability to leverage a nanoscale vector to protect and transport a pharmaceutical ingredient to its target organs, promising reduced side effects, higher efficacy, improved pharmacokinetics and pharmacodynamics, administration route versatility, intelligent characteristics and more.¹⁴⁻¹⁶

Nanoscale drug delivery systems, composed of media such as nanoemulsions¹⁷ or suspensions of liposomes,¹⁸ micelles,¹⁹ and polymersomes,²⁰ typically incorporate amphiphiles such as phospholipids and diblock copolymers to stabilize drug depots, as in the case of an emulsion system, or for self-assembly into structures segregating their pharmaceutical cargos. Further modifications to the nanoparticle or interface, such as inclusion of polyethylene glycol (PEG) to enhance circulation half-life and prevent phagocytosis by the immune system,²¹ and decoration with proteins, peptides, immunoglobulins and other moieties, has been argued to enhance therapeutic efficacy and reduce adverse events due their target homing ability.

Cancer chemotherapy has been the major beneficiary of this research output, with several nanotherapies having been sanctioned by the Food and Drug Administration (FDA), its European and Canadian counterparts, and other governmental regulatory bodies since the early 1990s.²² Y.C. Barenholz *et. al* is credited with the first successful commercialization of nanomedicine in which he encapsulated the potent chemotherapy doxorubicin into a PEGylated liposome by a salt gradient method.²³ Doxil®, the tradename of liposomal doxorubicin, entered the marketplace in 1995 with an intravenous indication for Kaposi's sarcoma, a disease often manifesting in immune-compromised individuals such as AIDS patients.²¹ Although other therapeutic areas beyond the oncology field are encouraged by nanomedicine's promise, they still are yet to gain anything substantial from the technology.²² Nanotherapeutics is still a fledgling area of research, and the regulatory process for approval of new chemical entities is long, costly and complex.²⁴ Despite these current obstacles, a possible path to address incompressible, internal hemorrhage may lie in employing nanotechnology tools in development of the next medicine.

A nanoparticle capable of efficaciously promoting hemostasis, a nanoparticle “hemostat,” in a patient presenting with internal, incompressible hemorrhage in a minimally invasive and directed fashion arguably should exploit the human body's intrinsic coagulation response. These networks are highly nonlinear and modulated by a myriad of positive and negative feedback mechanisms.²⁵ Naturally then, incorporating coagulation factors like thrombin or other endogenous biomolecules that already participate in hemostasis would be the first and most logical candidates to consider.²⁶

Inorganic polyphosphate (polyP) is an unbranched macromolecule of energy dense phosphate groups prevalent across the entire biome.²⁷ Initially observed by scientists several decades ago, its multivariate roles in biological systems have been poorly characterized until

recently.^{28, 29} Despite its apparent lack of chemical information density compared with other fundamental biomolecules such as nucleic acids and polypeptides, polyP is now believed to be central to a multitude of high-level phenomena including inflammation,³⁰ hemostasis,³¹⁻³⁴ and energy metabolism.³⁵ More recently, Ursula Jakob at the University of Michigan has shown that polyP behaves as a quasi-universal, non-protein chaperone, binding to countless polypeptides.³⁶ At physiological or slightly acidic pH, the polyelectrolyte is highly negatively charged and readily chelates a host of polyvalent ions such as calcium, magnesium, zinc and other transition metal ions.³⁷ Accordingly, polyP is frequently concentrated in electron dense bodies several hundred nanometers in diameter comingled with these ions. In unicellular organisms such as protozoa, these bodies are called “acidocalcisomes.”³⁸ DoCampo argues that “acidocalcisome”-like organelles are found in more complex species, including human blood platelets,³⁹ where Ruiz *et al.* first described them as “platelet dense granules” due to their appearance on an electron micrograph.⁴⁰

A novel, procoagulant nanotechnology employing polyP is presented called an “Artificial Dense Granule,” or ADG, that attempts to mimic the threshold-switchable, hemostatic effects of its human counterpart. The polyelectrolyte is condensed with metal ions and loaded into a PEGylated liposome using a facile and economical approach. The polyelectrolyte’s precipitation is systematically determined by dynamic light scattering (DLS). The particle’s morphology and composition are also characterized by electron microscopy and spectroscopic methods, respectively. *In vitro* models using clotting factors and human plasma are used to demonstrate ADG’s capacity to initiate clotting. It is then demonstrated that polyP nanoparticles can function as vehicles for protein transport and can potentially encapsulate high levels of procoagulant polypeptides such as BSA or Hemophilia Factor VIII (FVIII) for adjuvant hemostatic therapy.

In the proceeding introductory remarks, the body's hemostatic mechanisms will be reviewed through a survey of the tissue factor and contact pathways of blood coagulation. The current armamentarium of available treatments and procoagulants for hemorrhagic bleeding including polyP will follow. Subsequently, the array of relevant nanotechnologies will be expounded, including a discussion of their strengths and weaknesses, in order to support the claim that a nanoparticle platform containing a procoagulant agent is a natural candidate for the treatment of incompressible, internal hemorrhage in a directed and minimally invasive fashion.

1.2 The Blood Coagulation Cascade

Hemostasis encompasses an organism's defensive measures to attenuate and cease bleeding.⁴¹ These processes have evolved to mobilize extremely robust and rapid responses;⁴² however, overreaction to procoagulant stimuli may lead to thrombosis, pathological blood coagulation that may interfere with normal blood flow.⁴³ After traumatic injury the human body therefore attempts to expeditiously restore hemostasis while simultaneously preventing thrombosis.⁴⁴ This balance is only possible by a nonlinear network incorporated with negative and positive feedback mechanisms, which have the potential to explosively amplify signals by sensing minute changes in the environment.⁴² Coagulation is the human body's evolved response to bleeding, and is manifested as the gelation of blood into a fibrin clot.⁴⁵ The physical transformation of blood to achieve hemostasis is directed by a nonlinear biochemical response characterized by the "waterfall" activation of proteins called serine proteases.⁴⁶ Serine proteases are a class of proteolytic polypeptides that hydrolyze other proteins. In the blood clotting cascade an inactive clotting factor protein, or zymogen, is activated after proteolysis by another serine protease. The activated clotting factor then hydrolyzes its downstream zymogen.⁴⁷ As this proteolytic process proceeds, the procoagulant signal is exponentially amplified from an initially

low concentration of prohemostatic stimuli. The blood coagulation cascade is bifurcated into the extrinsic, or tissue factor pathway, and intrinsic, or contact pathway,⁴⁸ both of which will be outlined below.

1.2.1 The Tissue Factor Pathway of Blood Coagulation

The tissue factor pathway of blood clotting derives its name from the transmembrane protein, tissue factor (TF), expressed on subendothelial cells, which comes into contact with the zymogen Factor VII (FVII) after traumatic injury.⁴¹ Complexation of the zymogen with TF forms the activated complex, tissue factor-activated Factor VII (TF-FVIIa), which serves to propagate the procoagulant stimulus downstream through proteolytic cleavage of serine proteases such as Factor IX (FIX) and Factor X (FX).⁴⁹

1.2.2 The Contact Pathway of Blood Coagulation

Also referred to as the intrinsic pathway of blood clotting, for the role endogenous actors play in activating coagulation through this cascade, the contact pathway was largely thought to be nonessential for ensuring normal hemostasis. This argument is supported by the fact that congenital abnormalities in clotting factors central to the contact pathway, including Hageman Factor, or Factor XII (FXII), prekallikrein, and high molecular weight kininogen (HMWK), do not significantly alter clotting times results on routine laboratory tests.⁵⁰ The contact pathway of blood clotting is initiated by negatively charged surfaces such as glass, oxidized fatty acids, activated platelet membranes, or foreign particles like kaolin or ellagic acid that act as a template for the assembly of multiple proteins called the primary complex.⁵¹ The primary complex, consisting of FXIIa, kallikrein, and HMWK, proteolytically cleaves FXI.⁵⁰ FXIa subsequently activates FIX, the last step before initiation of the common pathway of blood clotting, characterized by the activation of thrombin and formation of the fibrin clot.⁴⁸

1.2.3 The Common Pathway of Blood Coagulation

The common pathway entails the formation of three major protein complexes and the polymerization of fibrin into a stable clot.⁴⁸ The tenase complex serves to activate Factor X and has two manifestations: the extrinsic tenase is an assembly of FVIIa, FIXa, and calcium ions, while the intrinsic pathway originating from the activation of the contact pathway consists of activated Factor VIIIa (FVIIIa), calcium ions, and a negatively charged phospholipid templating surface, typically phosphatidylserine (PS).⁵² Upon activation FXa recruits additional calcium ions and PS to form the prothrombinase complex with Factor Va, promoting the proteolytic cleavage of prothrombin to thrombin.⁵³ Thrombin cleaves peptide bonds proximal to the amino terminus of fibrinogen, converting it into monomeric fibrin. Fibrin polymerization and crosslinking is subsequently promoted by the activity of Factor XIIIa to generate a stable fibrin clot.⁵⁴

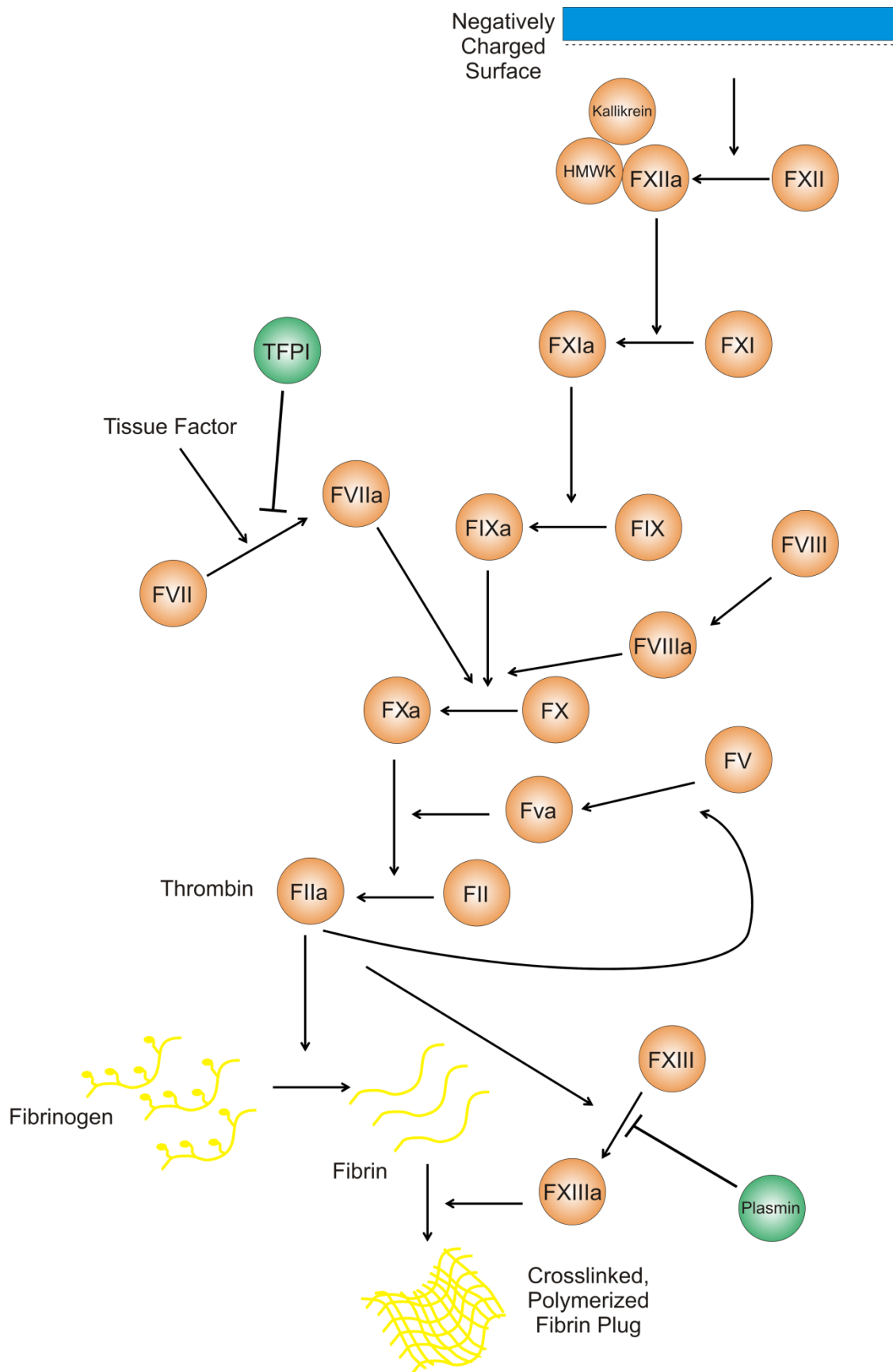


Figure 1.1. Blood Coagulation: A Highly Nonlinear Enzymatic Network. Blood coagulation balances hemostasis while minimizing thrombosis by proper regulation of a highly nonlinear network of proteolytic enzymes called serine proteases. Signals are explosively amplified and regulated by feedback networks to modulate fibrin polymerization in time and space. The cascade is conventionally divided into the tissue factor (extrinsic), contact (intrinsic), and final common pathways.

1.3 Current Treatment Options

The arsenal of commercially available therapies to combat traumatic hemorrhage encompasses a wide array of clotting proteins, synthetic procoagulants, antifibrinolytics that inhibit the breakdown of fibrin clots, and topical wound dressings. Protein engineering is one technology that has been extensively employed to synthesize recombinant human coagulation factors for administration. Initially targeting congenital coagulopathies, the Danish biopharmaceutical company Novo Nordisk engineered a recombinant version of activated human FVII, rFVIIa (trade name: NovoSeven®) to be given intravenously. rFVIIa activates platelet-expressed FX in the absence of TF.⁵⁵ The ability for rFVIIa to directly initiate the final common pathway via FX implies that rFVIIa can reduce bleeding times in patients deficient in several clotting factors such as FVII, FVIII, and FIX, which all modulate FX activity.⁵⁶ There is some evidence to suggest that rFVIIa may act as an effective prohemostatic agent even in the absence of any underlying bleeding disorder; however, clinical evidence for its efficacy remains equivocal.⁵⁷ Lyophilized thrombin, the last serine protease before fibrin polymerization, has been both engineered by recombinant DNA technology and purified from other sources (e.g. bovine), for hemostatic therapy. However, its indication has been limited for treatment of external bleeding events, given the significant probability of thrombosis if injected and, for bovine

thrombin, the robust immune response engendered by introduction of a foreign protein.^{8, 9} Even fibrinogen, the zymogen precursor to fibrin, has been topically administered in lieu of upstream clotting factors.⁵⁸

In addition to procoagulant therapies such as rFVIIa and thrombin, which promote fibrin clot formation, additional medications that slow or inhibit the breakdown of fibrin clots may also be considered after traumatic injury.⁵⁹ As the human body attempts to restore normal blood flow after hemorrhage, it must balance procoagulant and anticoagulant forces through its positive and negative feedback mechanisms in order to prevent thrombosis and achieve hemostasis.⁴⁴ As thrombin is polymerizing fibrin into a crosslinked mesh, upstream clotting factors indirectly driving thrombin formation, such as FXIIa, also convert a zymogen named plasminogen into activated plasmin, to counteract excessive clot formation. The hydrolysis of polymerized fibrin by plasmin is called fibrinolysis, and is characterized by plasmin binding to specific positively charged amino acids on fibrin.⁶⁰ In order to accelerate clotting plasmin and plasminogen inhibitors, e.g. tranexamic acid, have been successfully administered to treat hemorrhage after traumatic injury or used by surgeons to limit loss of blood.^{61, 62}

In addition to the armamentarium of procoagulant agents, antifibrinolytics, engineered clotting factor proteins, and wound dressings of biocompatible, biodegradable polymers have gained regulatory approval by the FDA. HemCon® is indicated for external, compressible hemorrhage and consists of a chitosan mesh fabricated as a surgical dressing.⁵ Chitosan is a biocidal polysaccharide composed of positively charged glucosamine units that interact electrostatically with red blood cells, which have a net negative surface charge. Although not a wound dressing, QuikClot® is another topical hemostat which reduces bleeding times by initiating the contact pathway of clotting. It consists of the pulverized silicate mineral kaolin,

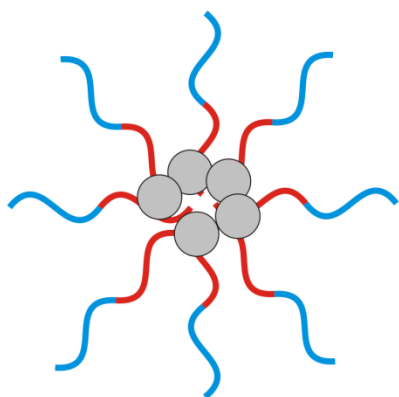
which acts a negatively charged templating surface for the activation of the intrinsic pathway's primary complex of FXII, prekallikrein, and HMWK.⁶³ HemCon® and QuikClot® have proven successful on the battlefield and in surgery; however, they lack versatility in treating the full range of bleeding presentations, including incompressible, internal hemorrhage, in which a tourniquet would be necessary.⁶⁴

1.4 Inorganic Polyphosphate (PolyP)'s Role in Blood Clotting

PolyP, with its dearth of complexity in its primary structure, was frequently conjectured to be obsolete in hosting a major role in physiological processes and sidelined by more complex biomolecules such as polynucleotides and proteins billions of years ago.^{28, 29} Contrarian views, especially by Arthur Kornberg, who developed the groundbreaking canonical model on DNA replication, argued later in his career that polyP had been neglected by the biochemistry community and offered evidence to suggest his theory.^{27-29, 65-67} Despite the low data density contained within the polymer's linear sequence of repeated phosphoanhydride bonds, the polyelectrolyte is able to manifest itself into a variety of secondary structures such as spherical nanoscale granules and two-dimensional surfaces which are at the center of a myriad of biological events typically requiring proteins.^{38, 68} Ruiz, DoCampo *et al.* identified polyP in the electron dense bodies contained within human platelet dense granules that are recruited into the blood circulation after initiation of primary hemostasis.⁴⁰ Smith *et al.* showed that polyP is procoagulant and antifibrinolytic by acting on several actors in the coagulation cascade,³¹ and its ability is modulated by the polymer's molecular weight.³³ Smaller polymer chains, approximately 70 phosphate residues, most potently inhibit tissue factor pathway inhibitor (TFPI) and accelerate the proteolytic conversion of FV to FVa.³¹ Polymers of the largest molecular weight behave like kaolin and other negatively charged foreign substances in initiating

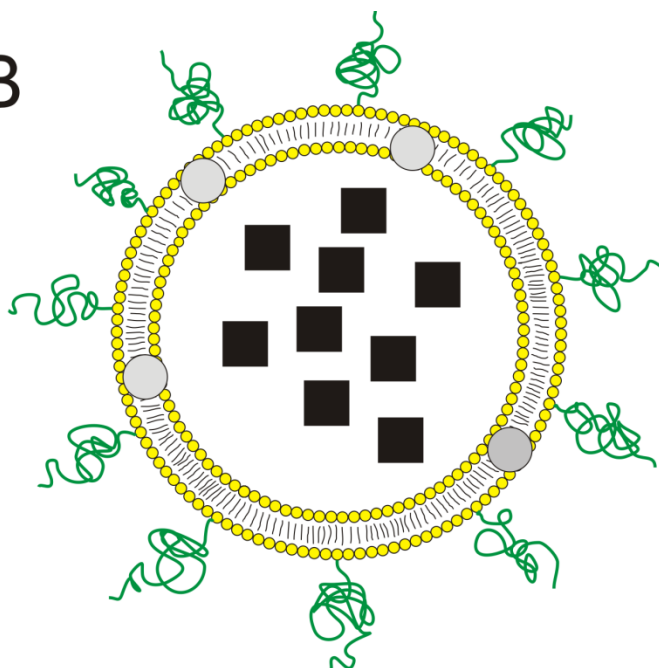
the contact pathway of coagulation.³³ Intermediate polymer sizes act on FXIII to enhance thrombus (fibrin clot) cross-linking, and electron micrographs suggest that the polymer may enhance clot density additionally by intercalating into the clot itself.³² The fact that polyP is able to exert manifold effects on blood clotting and other nonlinear processes suggests that secondary organization of the polymer into granules or two dimensional surfaces may play a role. Indeed, Coen Maas and colleagues provide the first evidence in an article in *Blood* that granular polyP nanoparticles are the agents involved in the activation of FXII *in vivo*.⁶⁹

A



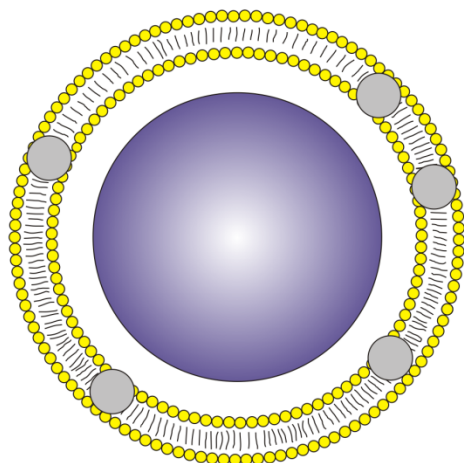
Polymeric
Micelle

B



Stealth
Liposome

C



Core-Shell Polymer
Lipid Hybrid
Nanoparticle

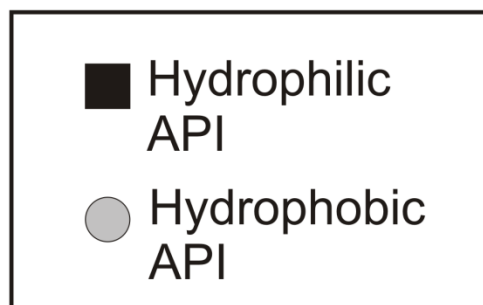


Figure 1.2. Nanotherapeutic Platforms. A. Micelle. Amphiphilic block copolymers and phospholipids may self-assemble into micelles upon changes in solvent quality and can encapsulate hydrophobic drugs in the micellar cores. **B. Vesicles.** Self-assembled bilayer vesicles of lipids can encapsulate hydrophilic compounds in the core and hydrophobic compounds in the bilayer region. Anti-immunogenic phospholipid vesicles possess long circulation half-lives due to the inclusion of small amounts of PEGylated phospholipids. Amphiphilic polymers may also form vesicle structures called polymersomes. **C. Core-Shell Polymer Lipid Hybrid Nanoparticle.** Polymeric nanoparticles can be loaded into lipid self-assemblies such as liposomes for enhanced drug loading. These particles possess attributes common to both lipid-based and synthetic polymeric drug delivery systems.

1.5 Nanotherapeutic Platforms

Nanotherapeutic platforms can be broadly divided according to the composition of their delivery vectors: (1) lipid-based drug delivery systems such as lipid micelles, liposomes, solid lipid nanoparticles (SLNs), and liquid crystalline nanoparticles; (2) polymeric particles such as spherical or cylindrical micelles and polymersomes; (3) hybrid platforms with lipid and polymeric constituents such as polymer-lipid nanoparticles (PLNPs); and (4) metallic colloids such as gold nanospheres or nanorods. Nanoscale drug delivery systems have conventionally focused on employing biocompatible and biodegradable ingredients such as natural phospholipids, and synthetic amphiphilic block copolymers. Many biocompatible polymers, such as poly(ethylene glycol) (PEG) and poly(lactic-*co*-glycolic acid) (PLGA) are already recognized by the FDA as *generally recognized as safe* (GRAS).⁷⁰ A survey of the current state of the literature relating to lipid-based, polymeric, and hybrid nanoparticles will be discussed here.

1.5.1 Lipid Based Platforms

Lipid-based delivery platforms can take the form of immiscible suspensions of stabilized oil droplets in aqueous media, for example an oil-in-water (O/W) or water-in-oil-in-water (W/O/W) emulsion system; or they can employ amphiphilic phospholipids which spontaneously self-assemble into nanostructures such as spherical micelles or liposomes (vesicles with an aqueous core and a bilayer shell). Liposomes are the most popular type of lipid vesicles, widely used for drug delivery.

1.5.1.1 Liposomes

Cells from all kingdoms of life, including Archaea, Prokaryota, and Eukaryota, encapsulate their contents in a phospholipid bilayer envelope called the cell membrane. The Cambridge University electron microscopist, A.D. Bangham, when he first viewed a stained phospholipid micrograph in 1965, noticed the resemblance between the phospholipid vesicles and cell membranes.^{71, 72} Phospholipids, with their hydrophobic acyl tails and hydrophilic phosphate head groups spontaneously assemble into bilayer structures in water above their critical micelle concentration (cmc) to form vesicles nanometers to microns across with one or multiple lamella.⁷³ With their superficial similarity to cells and tremendous versatility in the diversity of molecules with which they can encapsulate, owing to the presence of compartments for the sequestration of hydrophilic,²³ hydrophobic,⁷⁴ and even amphipathic moieties,⁷⁵ liposomes rapidly emerged as the vanguard in nanotherapeutic drug delivery platforms.⁷⁶

Stealth liposomes are phospholipid vesicles formed with PEG-conjugated phospholipids such mPEG₂₀₀₀-DSPE. Numerous research groups have reported that the addition of PEGylated phospholipids, at concentrations as low as 5% on a molar basis, may increase both the colloidal stability via steric repulsion and the pharmacokinetic stability by presenting a sufficiently

chemically inert and hydrophilic surface to the immune system.⁷⁷ Macrophages are white blood cells which are recruited by the body to engage foreign entities such as virions and bacteria via engulfment, or phagocytosis, and for subsequent degradation.⁷⁸ These immune system guardians display hydrophilic surface molecules on their membranes and detect harmful external actors that are more hydrophobic than themselves.⁷⁹ PEG is considered sufficiently hydrophilic in most cases so that it is invisible to macrophage attack.⁸⁰ These stealth characteristics endow PEGylated vesicles with improved pharmacokinetic attributes and enable sustained drug release schedules over hours to a day.⁷⁷

Although passively targeted liposomal drug delivery systems (DDSs) have demonstrated considerable success compared with other nanotechnology platforms, efforts to enhance therapeutic efficacy and mitigate adverse effects via the addition of intelligent homing characteristics remain an active area of research. Development of accessible, robust lipid conjugation chemistries has permitted the construction of a diverse library of covalently functionalized molecules. Activation of phosphoethanolamine with maleimide enables facile reaction with thiol-containing macromolecules, including polypeptides with cysteine residues under benign aqueous conditions.⁸¹ Conjugation of phospholipids with immunoglobulins in particular has given rise to a new paradigm in liposomal drug delivery—immunoliposomes, as they have become known, are phospholipid vesicles decorated with antibodies that specifically direct themselves toward cells expressing their target antigens.¹⁸ In combination with the anti-immunogenic effects of PEG, one can imagine that a stealth immunoliposome decorated with anti-HER2 (anti-human epidermal receptor 2 IgG), for example, may be a promising candidate for treating select breast cancers overexpressing the growth receptor on their cell membranes.⁸² The anti-HER2 IgG and PEG would allow for accumulation of the immunoliposome after

prolonged circulation and further release of an oncolytic medicine such as tamoxifen tailored to breast cancers to treat the tumor. Such a delivery platform may yield similar or enhanced efficacy with reduced side effects of conventional cancer chemotherapy.^{83, 84} A stealth immunoliposome with prohemostatic effects could encapsulate procoagulants such as condensed stores of polyP and leverage proteins such as p-selectin and integrins for binding with human blood platelets and accumulation proximate to the trauma site. Such a formulation may be more promising compared to injection of recombinant clotting factors due its targeted approach.

1.5.2 Polymeric Nanoparticles

Polymeric drug delivery systems are an exciting alternative to lipid-based therapeutic platforms, as they promise greater mechanical properties⁸⁵ and kinetic stability⁸⁶ and offer a greater range of functionality due to the expanding library of biocompatible and biodegradable synthetic polymers.⁸⁷ Concomitant with the growing number of polymeric building blocks is the universe of possible coupling chemistries available to further enhance targeting and stealth behavior in a manner not possible with liposomes.⁸⁸ Despite these pronouncements, regulatory progress in polymeric nanotherapeutics has failed to materialize, although several investigational new drug (IND) applications have been filed.²²

Amphiphilic block copolymers that behave like phospholipids in water are frequently exploited for nanoparticle synthesis.¹⁹ Diblock copolymers such as poly(ethylene glycol)-*block*-poly(capro-lactone) (PEG-*b*-PCL) form micelles in water, with the hydrophilic PEG chains forming the aqueous shell and the PCL forming the collapsed, hydrophobic core. A solution of a hydrophobic drug and PEG-*b*-PCL can be mixed with an antisolvent such as DI-H₂O to form PEG-*b*-PCL nanoparticles encapsulating the drug. A change in solvent quality is used to *nanoprecipitate* the diblock polymer and hydrophobic drug after mixing with the antisolvent. In

other words, poorer solvent quality after addition of water raises the polymer and drug concentration above their solubility limits, initiating the process of drug nucleation and growth and polymer micellization, yielding a colloidal suspension of polymeric nanoparticles with encapsulated drug in the particle's hydrophobic core.⁸⁹

Beyond polymer amphiphiles, the process of nanoprecipitation can be applied more broadly to instances in which colloidal particles of any kind are formed after changes in solvent quality. For example, the solubility of polyelectrolytes, polymers with a net charge, is a function of the ionic strength. A systematic investigation of the polyelectrolyte solubility across a spectrum of salt concentrations may therefore prove useful in the optimization of any nanoparticle formation with the charged polymer. PolyP is a highly negatively charged polyanion. Such an approach may be fruitful with polyP, as its interaction with metal cations is already being well-discussed in the literature.³⁷

1.6 Experimental Techniques

1.6.1 Dynamic Light Scattering (DLS)

Dynamic light scattering (DLS) is a robust and established method to interrogate the properties of colloidal suspensions such as particle diffusivity and diameter. A force diagram of a colloidal nanoparticle shows that random thermal motion ($k_B T$) tends to dominate over volumetric forces such as gravity (mg), allowing the particle to remain suspended and not sediment, absent other forces. When a laser is aimed at a nanoparticle smaller than $1/10^{\text{th}}$ of the wavelength of the incident light, it will scatter the light isotropically (Rayleigh scattering). When the size of particles is larger than $1/10^{\text{th}}$ of the wavelength of the incident light, it is anisotropic Mie scattering. At a short time Δt later, the particle has drifted from its initial location due to Brownian motion, and the intensity of the scattered light is related to the initial scattering intensity by the diffusivity. The fluctuation of intensity in scattered light is correlated against

decay intervals. A sample with Brownian particles will yield an autocorrelation function that diminishes exponentially with increasing Δt . To determine the particle diffusivity, the associated exponential decay constant is extracted. To calculate the hydrodynamic diameter of a spherical particle, the Stokes-Einstein equation is employed. The Stokes-Einstein equation relates the hydrodynamic diameter of a hard sphere undergoing Brownian motion to the effective translational diffusivity with a geometric proportionality constant.

Beyond measurements of the translational diffusivity and the hydrodynamic diameter of colloidal suspensions, DLS in this thesis study was utilized to investigate the CMC and solubility of the polymers and compounds. The integrated raw intensity of the scattered light is proportional to the sixth power of the radius. Therefore, colloids scattered light much more strongly than molecularly-dissolved compounds. In this way, it can be easily determined when precipitation occurs through observation of the changes in raw scattered intensity. For example, dipalmitoylphosphatidylcholine (DPPC) will have a scattering count rate just above the baseline scattering of pure filtered DI-H₂O at extremely low (few picomolar) concentrations as individual molecules barely scatter any laser light; however, at 0.46 nM, the scattering count rate increases abruptly as DPPC forms micelles that are capable of scattering light more strongly than the individual DPPC molecules. A plot of the scattering count rate versus DPPC concentration will suggest two different regimes: (1) the scattering intensity of individual DPPC molecules fit to a line with nearly horizontal slope; and (2) a steady increase in the scattering count rate with increasing concentration manifested by the formation of micelles. The concentration serving as the boundary between these two conditions is referred to as the CMC.

1.6.2 Transmission Electron Microscopy (TEM)

Transmission electron microscopy (TEM) is a versatile technique to characterize a variety of biological materials at the nanoscale. As a conventional light microscope optically magnifies features of a specimen, its resolution is inherently limited by the wavelength of visual light. In contrast, electron microscopes leverage the particle-wave duality of matter to employ beams of electrons instead of photons, resulting in resolutions several orders of magnitude greater than visual microscopy, with some now able to even discern features of individual atoms due to their intense beam energies. In TEM, the electron beam is transmitted through the specimen dried onto a thin grid under high vacuum. The image is subsequently constructed from the transmitted interference pattern.

1.6.3 Biocompatible High Resolution Scanning Transmission Electron Microscopy (HR-STEM)

Conventional electron microscopy techniques and, even to a lesser extent, cryo-TEM (*cryogenic* transmission electron microscopy), are not versatile enough to image biological preparations at high resolutions under conditions similar to their native environments. Biological or biomimetic specimens often contain biomolecules with high energy bonds and ionizable groups, which makes these samples highly prone to electron-beam induced radiation damage.⁹⁰ Further, conventional TEM requires that the samples be dessicated and imaged under high vacuum, precluding the examination of colloidal suspensions under aqueous conditions. Biocompatible high resolution scanning transmission electron microscopy (HR-STEM) is a recently developed technique that is suitable for biological specimens in their native environments, which leverages the material properties of graphene, a two-dimensional nanomaterial composed of sp^2 -hybridized carbon atoms.⁹¹ The material allows electrons to pass

through but is practically impermeable to other atomic species including protons (hydrogen ions). In this fashion, a biological specimen could potentially be encapsulated by two layers of graphene monolayers and simultaneously visible to an electron beam for imaging. Furthermore, radiation damage and its ramifications would be significantly mitigated as the beam would moderately weaken in intensity as it passes through the delocalized pi electron cloud, and any hydrogen gas formed after ionization or bond cleavage would not readily diffuse out of the graphene sandwich. Lastly, the nanoparticle may be able to remain in its aqueous environment, as any water molecules would remain in the graphene liquid cell (GLC).

The process for encapsulating a biological or biomimetic specimen in a GLC entails the following: (1) A graphene monolayer is deposited onto a copper substrate by chemical vapor deposition (CVD); (2) the copper is removed by placing the graphene-coated copper in a solution of iron (II) sulfate, an etchant; (3) After removal, a coherent light source, e.g. a handheld laser, is utilized to identify the graphene monolayer by use of an evanescent wave (4) The graphene monolayer is transferred to DI H₂O for washing; (5) The sample is pipetted onto a graphene-coated TEM grid, flipped upside down, and placed on top of the monolayer graphene, and subsequently dried under vacuum. The biological sample is now encapsulated between two graphene sheets and ready for imaging in a STEM.

CHAPTER 2. THERMODYNAMIC SELF-ASSEMBLY OF INORGANIC POLYPHOSPHATE GRANULES IN AQUEOUS ELECTROLYTE SOLUTIONS

The text in this chapter was originally published in part as Donovan, A.J. *et al.* “Size-controlled synthesis of granular polyphosphate nanoparticles at physiologic salt concentrations for blood clotting.” *Biomacromolecules*, **2014**, 15 (11): 3976-3984.

2.1 Introduction

PolyP precipitates could wield different procoagulant effects than the molecularly dissolved polymer, possibly serving as an anionic contact “surface” for activation of FXII like kaolin and collagen.⁵⁰ Alternatively, these bodies could have evolved in evolution’s early stages merely as condensed stores of large concentrations of polyP for later downstream cellular functions requiring rapid nonlinear responses. PolyP has been known for approximately a century to reversibly bind to calcium, magnesium, iron, copper, zinc, barium and other metals.⁹² The calcium concentration within the platelet dense granules is as high as 2.2 M,⁹³ and the dissociation constants for Ca^{2+} and Mg^{2+} have been quantified.⁹⁴

Although successful synthesis of aluminum polyP nanoparticles has been reported, the established synthetic routes require harsh organic solvents, intensive separation processes, and lead to inadequate size control.⁹⁵ Momeni *et al.* investigated polyphosphate gels, or “coacervates,” for potential utilization as hemostatic agents and examined the chelation of Ca^{2+} , Ba^{2+} , and Sr^{2+} to polyP glasses of varied polymer lengths and its effects on solution pH and chain degradation of the polyP solution.^{96, 97} However, systematic measurements of polyP precipitation into particles with controlled sizes have never been reported. Moreover, the downstream therapeutic potential of polyP precipitation has not been adequately addressed in the literature.

Herein, we show that the precipitation of inorganic polyP into granular nanostructures is based on polymer length, with very long polymer lengths condensing much more robustly than shorter chains like those found in human platelet dense granules. Furthermore, these condensed polyP granules are stable in aqueous buffer and albumin suspensions on the same time scale as catastrophic bleeding events and possess potent procoagulant function, when assaying for activation of the contact pathway. Precipitation of inorganic polyP in aqueous calcium and/or magnesium could potentially serve as a facile therapy to mitigate the deleterious effects of serious trauma via the delivery of high concentrations of polyP stores locally to bleeding sites to rapidly induce coagulation.

2.2 Experimental section

2.2.1 Materials and reagents

Tris(hydroxymethyl)aminomethane, $\text{CaCl}_2 \cdot 6\text{H}_2\text{O}$, $\text{MgCl}_2 \cdot 6\text{H}_2\text{O}$, NaCl, KCl, and BSA were purchased from Sigma-Aldrich (St. Louis, MO). Water was de-ionized to 18.2 M Ω -cm (Nanopure II, Barnstead, Dubuque, IA). Citrated, pooled normal plasma was purchased from George King Bio-medical (Overland Park, KS). L- α -phosphatidylcholine (PC), L- α -phosphatidylserine (PS), and Avanti® Mini-Extruder with 200-nm pore diameter polycarbonate membrane were purchased from Avanti Polar Lipids (Alabaster, AL). All materials were purchased at standard grades and used as received. PolyP80 (76-84 repeating units), polyP250, (100-390 repeating units), polyP305 (242-383 repeating units), and polyP1000+ (more than 1000 repeating units) were size fractionated via preparative electrophoresis as previously described,³³ or by differential isopropanol precipitation of heterogeneous long chain polyP.

Natriumpolyphosphat P70 (BKGP70, 20-125 repeating units, mode ~45) was purchased from

BK Guilini GmbH (Ludwigshafen am Rhein, Germany). PolyP concentrations are given throughout in terms of the concentration of phosphate monomer (monoP).

2.2.2 PolyP nanoprecipitation

Aqueous size-fractionated polyP was micropipetted into 8 mM Tris·HCl, pH 7.4 solutions containing combinations of the following: 1.2 mM, 5.0 mM, or 7.5 mM CaCl₂; 0.4 mM MgCl₂; 4.35 mM KCl; and 150 mM NaCl. The nanoparticles were then vortexed for five seconds. Precipitation was characterized by DLS (Brookhaven NanoDLS, Brookhaven, NY).

2.2.3 Determination of PolyP Solubility

The measurements of polyP solubility are similar to the procedure used to determine the CMC of surfactants, copolymers, and phospholipids using DLS. PolyP samples were prepared as described above and injected into the DLS, beginning at exceedingly low concentrations (typically 100 nM – 1 μM monoP), where the scattering count rate resembled that of molecularly dissolved polyP. The polyP concentration was slowly titrated up until the scattering count rate increased and the correlation function was a well-behaved exponential decay on the baseline, suggesting that the polyP sample was supersaturated. The scattering count rate was then plotted against the logarithm of the monoP concentration, producing a plot with two clear regimes representing: (1) molecularly dissolved polyP, and (2) precipitated polyP. A linear regression was then performed on each regime and the point of intersection was found, which was defined as the solubility concentration. For consistency, all measurements were done on low laser intensity.

2.2.4 PolyP Nanoparticle (NP) Stability

2.2.4.1 Stability in Aqueous Buffer

NPs were synthesized using polyP250 (125 μM) in either 1.2 mM or 5 mM CaCl_2 buffered with 8 mM Tris·HCl, pH 7.4 as discussed previously. Immediately after vortexing, particle size was characterized by DLS using at least a one-minute scattering time every five minutes for 1 h at room temperature.

2.2.4.2 Stability in BSA Suspensions

A solution of BSA (70 mg/ml) containing 8 mM Tris·HCl, pH 7.4 was prepared both with and without 2.5 mM CaCl_2 the day before experiments were conducted. PolyP250 (125 μM) was nanoprecipitated in 5 mM CaCl_2 , 8 mM Tris·HCl, pH 7.4, and the particle diameter was determined immediately by DLS. The polyP NPs were then mixed 1:1 (v:v) with the BSA suspensions. The resulting BSA and CaCl_2 concentrations were thus 35 mg/ml and 1.25 mM, respectively. Particle size was measured using DLS every five minutes for 1 hour, and subsequently every 30 minutes until three hours had elapsed. The dispersion viscosity was calculated to be 1.2 centipoise,⁹⁸ and the refractive index was kept the same as water (1.331).

2.2.5 Complex Coacervation of polyP and BSA

Aqueous CaCl_2 , polyP and BSA were mixed in equal volumes yielding nanoscopic polyP-BSA complexes. Coacervation followed two protocols regarding the order of addition of components to investigate its ramifications on nanoparticle formation, stability, and protein interactions. The first complexation method examined the effects of adding BSA first to aqueous calcium: 500 μl BSA (15 μM -2.5mM) was first saturated with 500 μl 15 mM CaCl_2 , followed by addition of one 500 μl 15 mM polyP. Each mixing event was followed by a short duration (5-10s) of vortexing to ensure proper mixing. The second method entailed forming Ca-polyP complexes first, followed by addition of BSA (15 μM -2.5mM). Final concentrations of CaCl_2 and

polyP45 were both 5 mM. Final molar ratios of polyP45 to BSA (polyP:BSA ratio) ranged from polyP:BSA=0.13 to polyP:BSA=22.2.

2.2.6 Turbidometric measurements for polyP-BSA Complexes

Turbidity of the polyP:BSA complexes were determined by measuring absorbance at 405 nm (A_{405}) in a Finstruments Microplate Reader (MTX Lab Systems, Vienna, VA, USA). Briefly, immediately after coacervation, 100 μ l of each sample was pipetted in triplicate into a 96-well plate, and the A_{405} was averaged to give the optical turbidity for each sample.

2.2.7 Transmission Electron Microscopy

2.2.7.1 Sample Preparation

PolyP250 (125 μ M) was nanoprecipitated in 5 mM CaCl_2 , 8 mM Tris·HCl, pH 7.4 as described above. The sample (10 μ l) was micropipetted onto a 300-mesh carbon-coated Formvar® grid (Structure Probe Inc., West Chester, PA) and allowed to dry in air for 10 minutes. The remaining liquid was wicked away with a Kim® wipe and the process was repeated two more times to increase particle density and minimize aggregation. The sample was viewed in a JEOL JEM-1220 Transmission Electron Microscope (JEOL, Japan).

2.2.7.2 X-Ray Microanalysis

Energy-dispersive X-Ray microanalysis during TEM imaging was employed to obtain an elemental analysis of the granular polyP NPs by exploiting the characteristic emission spectra of the elements P, Ca, O, and others. PolyP250 NPs (10 μ l) were micropipetted onto 300-mesh Holey Formvar® carbon grid. The sample was dried for 15 minutes and examined in a JEOL JEM-3010 Transmission Electron Microscope (JEOL, Japan) and subjected to X-Ray spectroscopy.

2.2.8 Preparation of Large Unilamellar Vesicles (LUV) for Clotting Assays

LUVs (200 nm) of PC to PS (80:20 molar ratio) were made by extrusion.⁹⁹ Briefly, 158 μ l of 10 mg/ml L- α -PC and 42 μ l of 10 mg/ml L- α -PS dissolved in chloroform were pipetted into a glass scintillation vial and dried under Argon gas. The resulting lipid film was then placed under vacuum for an additional 1 hour to remove any residual chloroform. The lipid cake was subsequently rehydrated with 1 mL Tris buffer, pH 7.4 and passed through an extruder with a polycarbonate membrane with 200-nm pore size 11 times to generate monodisperse LUV. Liposome diameter and polydispersity were verified by DLS.

2.2.9 Clotting Assays

Clotting was evaluated using a microplate-based assay as previously described¹⁰⁰ with minor modifications. The citrated plasma was pre-warmed to 37°C for 20 minutes, and polyP was nanoprecipitated at room temperature and evaluated by DLS before proceeding with the assay. Wells contained 50 μ l of citrated pooled normal plasma, 50 μ l of polyP NPs in 5 mM CaCl₂, 8 mM Tris·HCl, pH 7.4, and coagulation was initiated with 50 μ l of 25 mM CaCl₂, 75 μ M LUV, 8 mM Tris·HCl, pH 7.4. Final excess free calcium was estimated to be 4.72 mM. LUVs containing a small amount of phosphatidylserine (~20 mol%) were added in contact activation assays, because the prothrombinase complex, consisting of Factor Va and Factor Xa, assembles on negatively charged phospholipid membranes in the presence of calcium. In the absence of negatively charged phospholipids, thrombin formation would be significantly hindered. Absorbance was read at 405 nm at room temperature on a FinstrimentsTM Microplate Reader (MTX Lab Systems Inc., Vienna, Virginia) every minute for 30 minutes. The sigmoidal absorbance traces were fitted to a standard Boltzmann growth function in Origin Pro 8.6 (OriginLab Corp., Northampton, MA). The x-coordinate of the inflection point (parameter x0) was defined as the time at which clotting occurred.

2.3 Results and Discussion

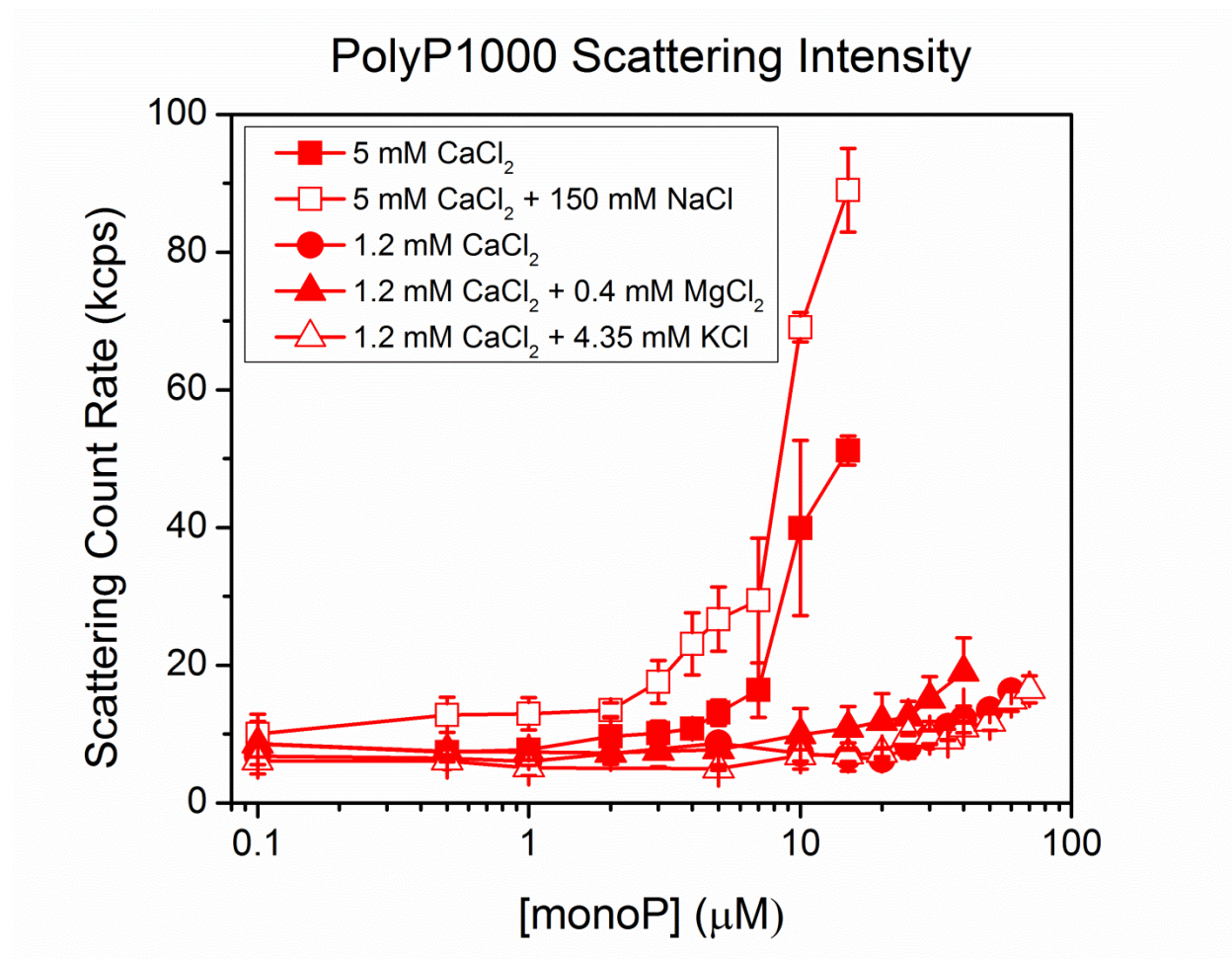


Figure 2.1. The precipitative effects of different metal cations on very long chain polyP.

Divalent metal cations such as Ca^{2+} and Mg^{2+} cause PolyP1000+ to robustly nanoprecipitate at physiological concentrations, as evidenced by the steep rise in the scattering intensity count rate, whereas monovalent cations such as Na^{+} and K^{+} at biologically relevant concentrations exert negligible effects on the polymer's solubility.

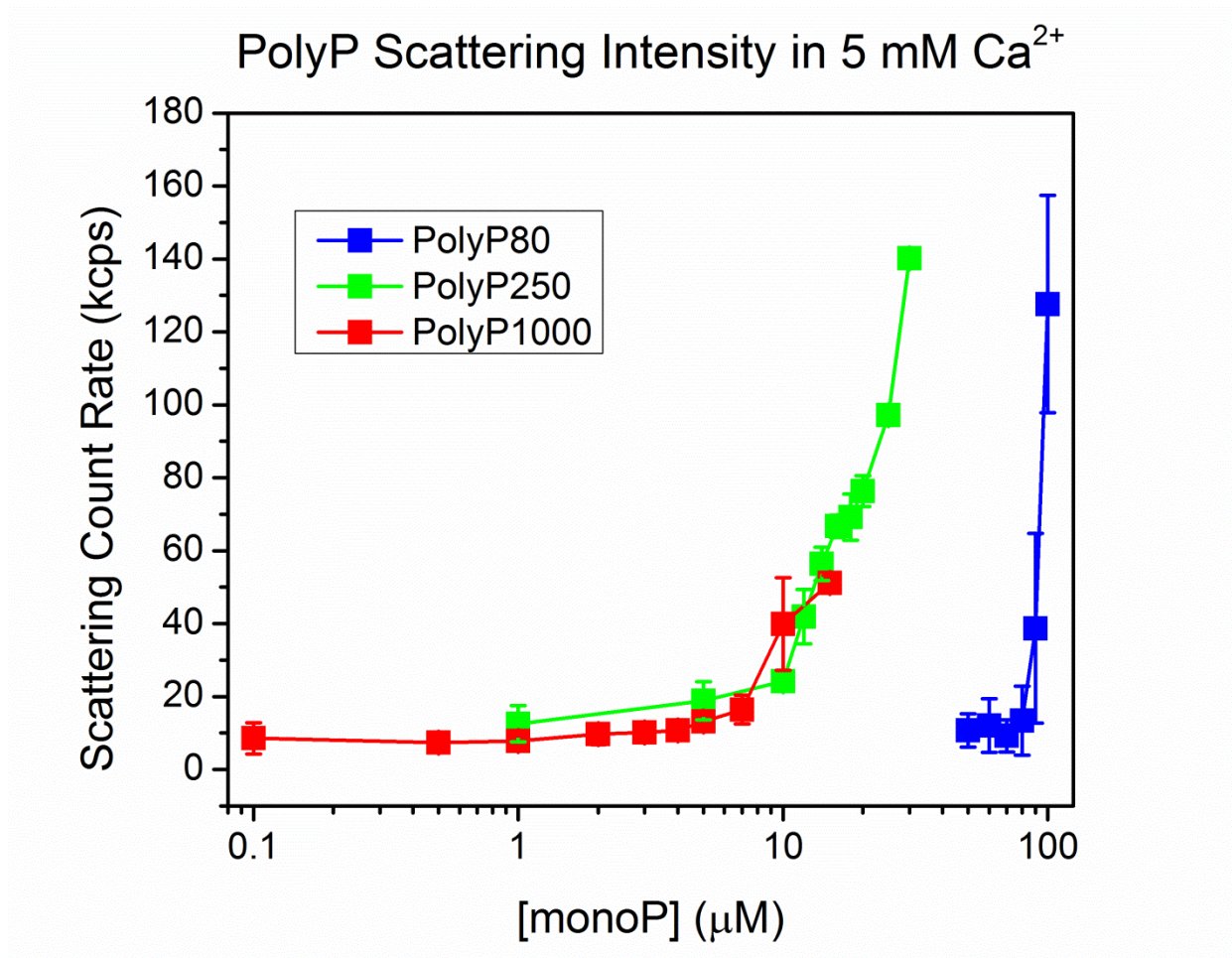


Figure 2.2. 5 mM CaCl₂ yields divergent precipitative effects on polyP depending on the polymer length. PolyP1000+ precipitates most robustly with a steep rise in scattering intensity at 4.3 μM monoP concentration. PolyP250 is more soluble than PolyP1000+, with the count rate increasing near 9.4 μM. Platelet-size polyP (PolyP80) is more soluble than both very long- and intermediate-chain length polyP, with the scattering intensity markedly increasing at a monoP concentration almost a magnitude higher than PolyP250.

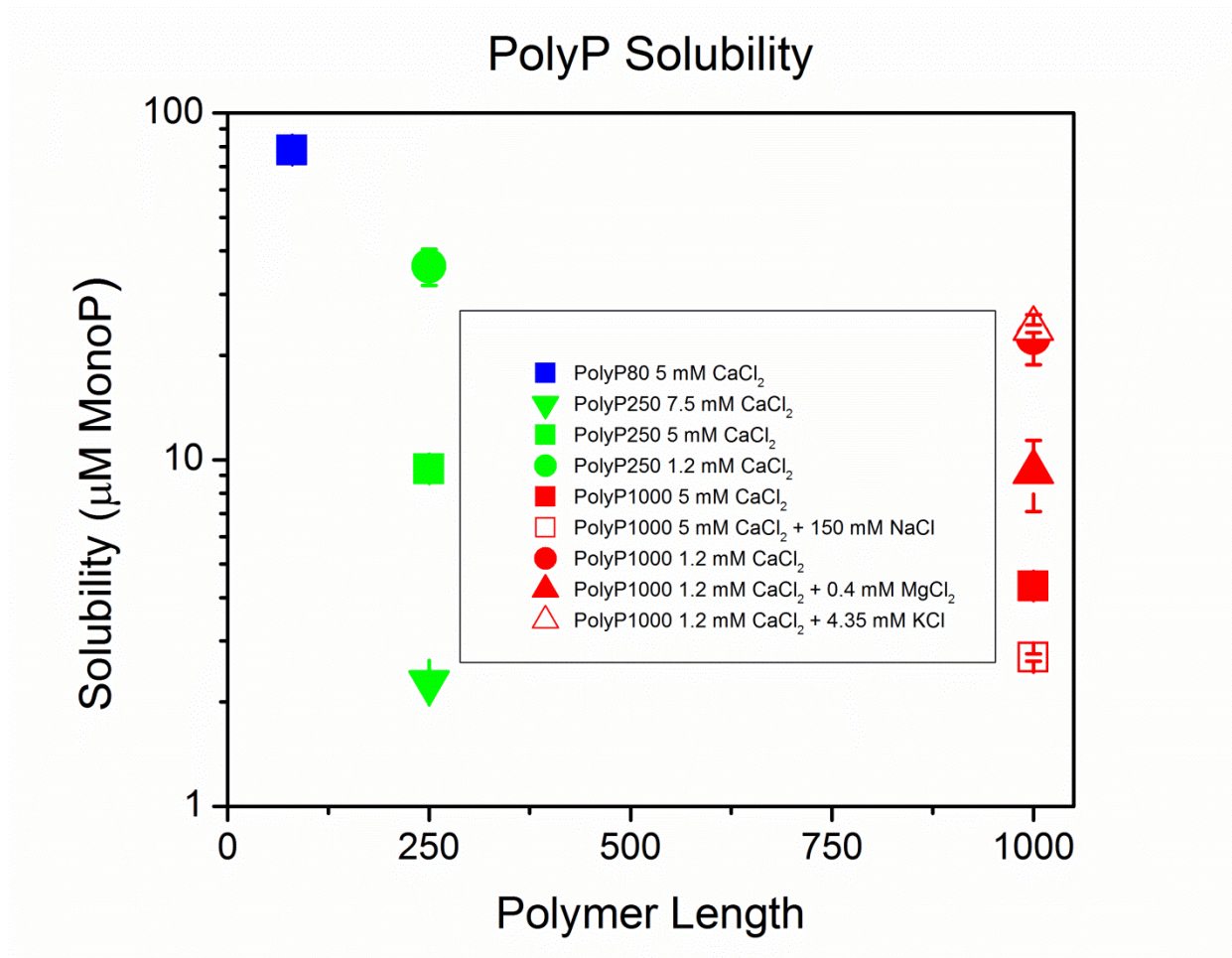


Figure 2.3. Solubility of polyP of different polymer lengths. PolyP's solubility in various aqueous salt solutions buffered with 8 mM Tris·HCl, pH 7.4 plotted against polymer length in monoP units. There is a strongly non-linear relationship, with very long chains (i.e. PolyP1000+) being much more readily precipitated than shorter polymers, e.g. polyP80. Divalent metal cations like Ca^{2+} and Mg^{2+} , which are known to chelate strongly to phosphate-containing compounds, exert precipitative effects at biologically relevant concentrations, while monovalent ions such as Na^+ and K^+ induce little or no significant effects on polyP's solubility.

In this study, the solubilities of polyP of differing polymer lengths were first investigated by employing DLS. Analogous to determining the critical micelle concentration of a surfactant,

the light scattering count rate begins to markedly increase when polyP begins to precipitate into NPs. The scattering intensity of very long chain polyP (PolyP1000+, similar to the long chains in prokaryotes) in aqueous solutions containing various concentrations of mono- and divalent cations is shown in **Figure 2.1**. PolyP precipitated in the presence of divalent metal cations at biologically relevant concentrations (5 and 1.2 mM CaCl_2 , and 1.2 mM CaCl_2 + 0.4 mM MgCl_2); however, monovalent cations exerted far less precipitative effects than their divalent counterparts. At 5 mM CaCl_2 , concentrations typical of conventional clotting assays, polyP nanoprecipitated much more easily than at physiological concentrations (1.2 mM CaCl_2). K^+ at normal physiological concentration does not statistically change the scattering intensity profile, while Na^+ at a relatively high ionic strength of 150 mM combined with 5 mM CaCl_2 causes the scattering intensity to increase at a modestly lower monoP concentration. Ca^{2+} and Mg^{2+} function synergistically to promote nanoprecipitation. The solubility in 1.2 mM CaCl_2 + 0.4 mM MgCl_2 is more than 60% lower than in 1.2 mM CaCl_2 alone.

Nanoprecipitation was also a function of polymer length, with very long chains precipitating much more robustly than intermediate-length polyP (PolyP250) or platelet-size polyP (PolyP80) at 5 mM CaCl_2 (**Figure 2.2**). The solubility for each precipitative condition was determined by finding the intersection of the two linear regressions representing molecularly dissolved polyP and polyP NP regimes as plotted in **Figure 2.3**. The solubilities for polyP1000+ and polyP250 at 5 mM CaCl_2 were 4.3 and 9.4 μM , respectively, while platelet-sized polyP's solubility at the same condition was about 78 μM . Although not measured, it is safe to assume that PolyP80's solubility concentration is at or above 78 μM in 1.2 mM CaCl_2 . Upon platelet activation, the concentration of polyP in whole blood can reach up to 2-7 μM ,³³ which suggests that platelet polyP likely exerts its procoagulant effects while remaining largely molecularly

dissolved. However, the next experiments demonstrate that polyP nanoparticles exhibit dilution hysteresis, keeping open the possibility that condensed polyP precipitates remain in NP format after secretion from activated platelets, despite being below the thermodynamic solubility limit. In addition, the local concentration of secreted polyP could be orders of magnitude higher than 2-7 μM inside platelet-rich thrombi.

The solubility of platelet-sized polyP in 5 mM CaCl_2 as a function of pH was also investigated. polyP is stored intracellularly under mildly acidic conditions ($\sim \text{pH } 5.4$) together with extremely concentrated levels of calcium cations, serotonin, and pyrophosphate under the tight regulation of a H^+ -ATPase pump in human platelet dense granules.¹⁸ Given that this is the case in prokaryotic organisms as well, one could speculate that polyP may be more easily precipitated under acidic conditions. However, at least for platelet-sized polyP, the solubility is nearly identical at both mildly acidic and basic conditions (see **Figure 2.4** and **Table 2.1**).

The observed scattering behavior of polyP at nM to μM monoP is more consistent with nanoprecipitation of the polyelectrolyte, rather than a transition to coil overlap. In other words, the concentration regime is too low to suggest that the measured solubility is a progression from a dilute to semi-dilute regime in the vicinity of the overlap concentration, C^* .¹⁰¹

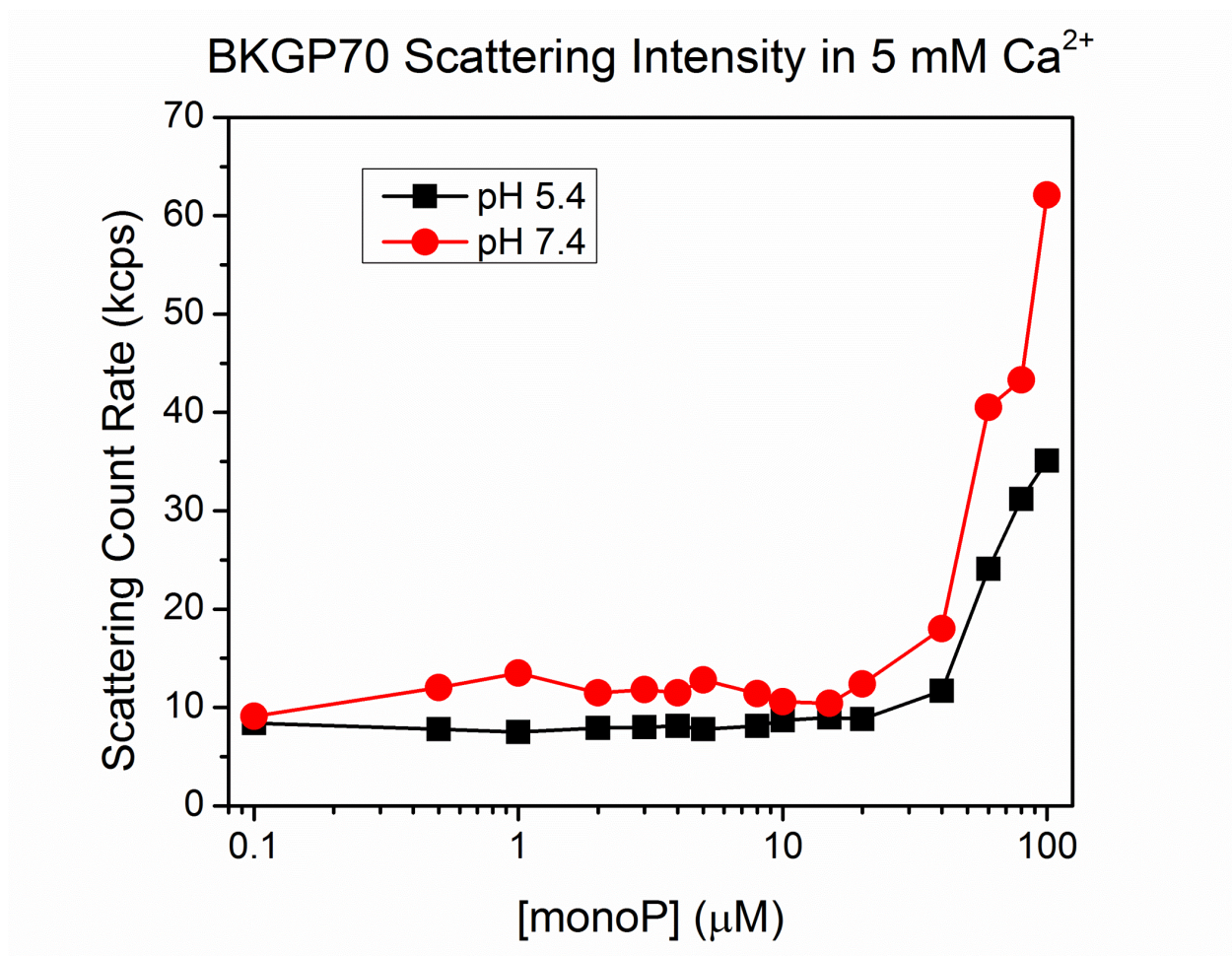


Figure 2.4. Scattering intensity of heterodisperse, platelet-sized polyP (“BKGP70,” range 20-125 phosphate units) in 5 mM CaCl₂ at pH 5.4 and 7.4. The scattering intensity begins to rise at roughly the same concentration, even though the overall scattering count rate is slightly higher at pH 7.4.

PolyP Polymer Length (Range)	Solubility (μM) in 5 mM CaCl ₂ , pH 7.4 ±S.D.	Solubility (μM) in 5 mM CaCl ₂ , pH 5.4
PolyP80 (76-84)	78±6	--
BKGP70 (20-125)	34.5	33.8
PolyP250 (100-390)	9.4±0.7	--
PolyP1000+ (>1000)	4.3±0.1	--

Table 2.1. The solubilities of polyP in 5 mM CaCl₂ (aq) based on pH and polymer length.

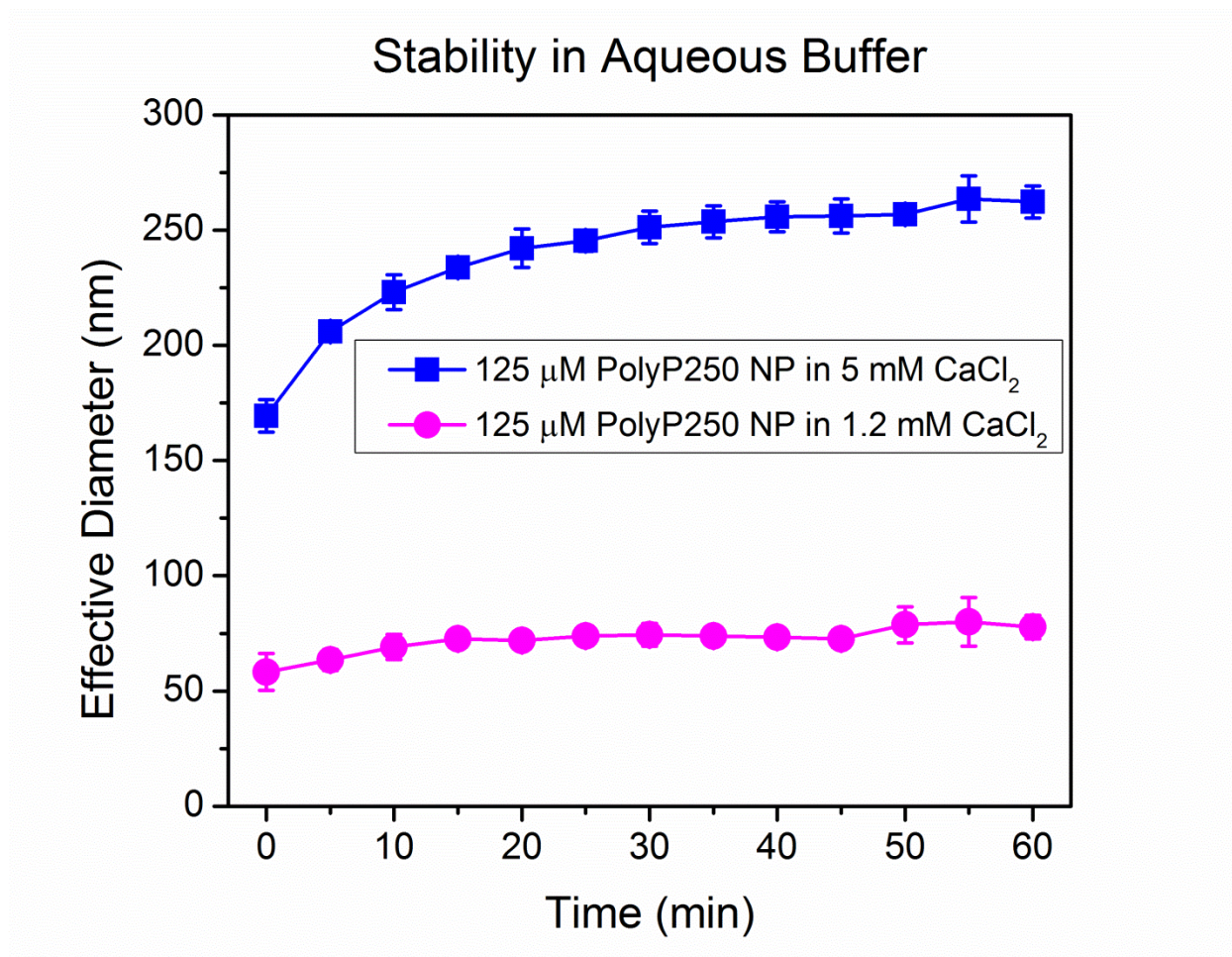


Figure 2.5. PolyP250 nanoparticle stability in aqueous buffer. 125 μ M PolyP250 was nanoprecipitated in 8 mM Tris·HCl, pH 7.4 containing 1.2 mM or 5 mM CaCl_2 . Average effective diameter was assessed every five minutes for one hour, a typical timescale for a bleeding event. At 5 mM CaCl_2 , the initial particle diameter was 169 nm and slowly grew to be approximately 260 nm after one hour. At 1.2 mM CaCl_2 the particles were initially 58 nm and steadily increased to ca. 80 nm. The growth behavior of both suspensions appears to follow power-law kinetics typical of many metastable colloidal dispersions.

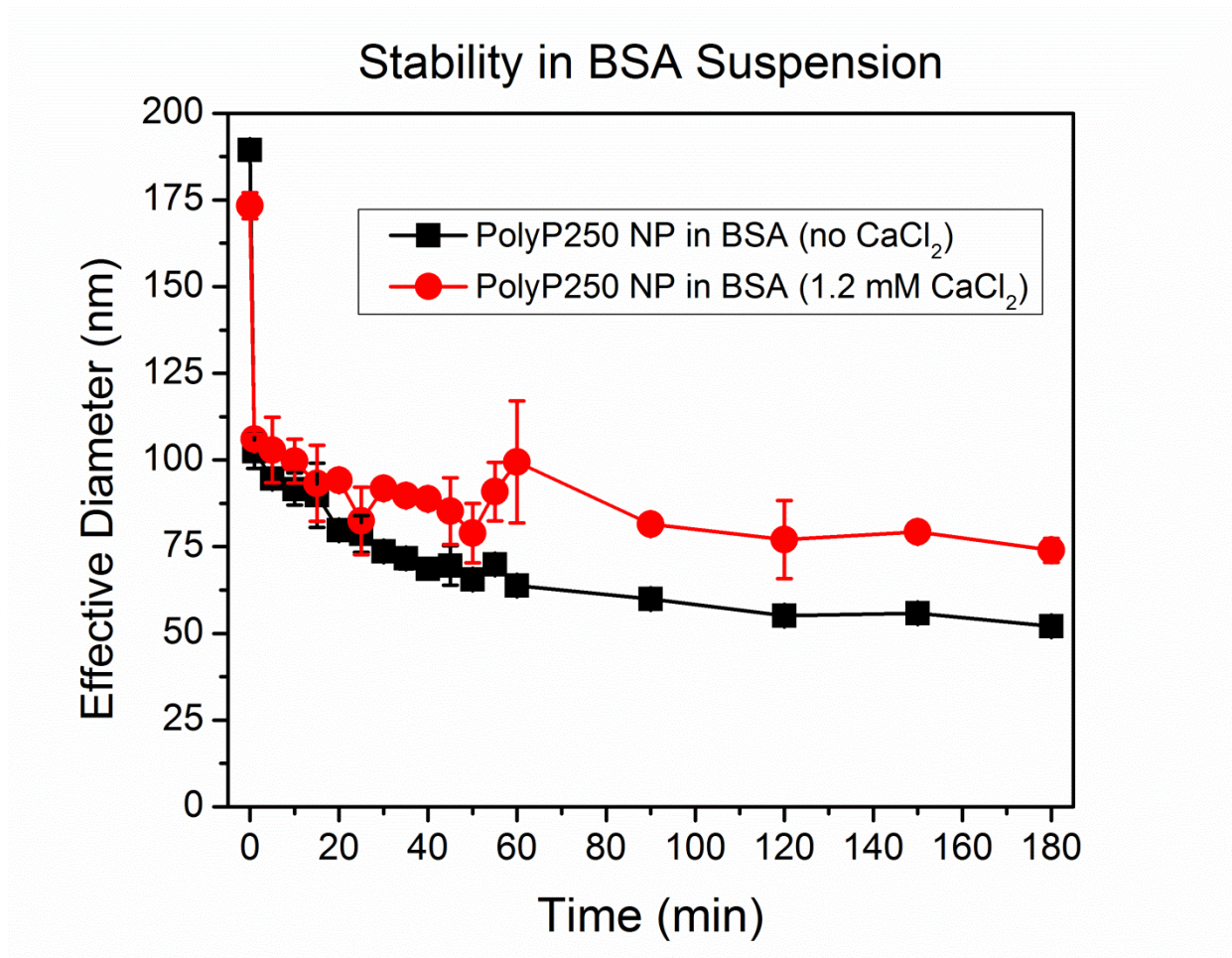


Figure 2.6. PolyP250 nanoparticle stability in suspensions containing BSA. 125 μ M polyP250 was precipitated in aqueous buffer containing 5 mM CaCl₂ as described previously and then mixed 1:1 (v:v) with 70 mg/ml BSA suspension buffered to pH 7.4 with or without 1.2 mM CaCl₂. Final BSA and CaCl₂ concentrations were 35 mg/ml and 1.2 mM, respectively. In both cases, the polyP250 NPs shrank from approximately 170-180 nm before mixing with the BSA solution, to 100 nm immediately after mixing with the BSA solution. This was not due to changes in dispersion viscosity or multiple scattering effects (confirmed by more measurements presented in Supporting Information, **Table S1**). After 3 hours, the polyP NPs in BSA without CaCl₂ equilibration shrank to approximately 50 nm in diameter, while the NPs in the BSA equilibrated with 1.2 mM CaCl₂ were roughly the same size (ca. 80 nm). It is hypothesized that

BSA may be initially forming a complex with polyP (the rapid shrinkage upon addition to the suspension) and then competitively binding Ca^{2+} , unless it has been pre-equilibrated.

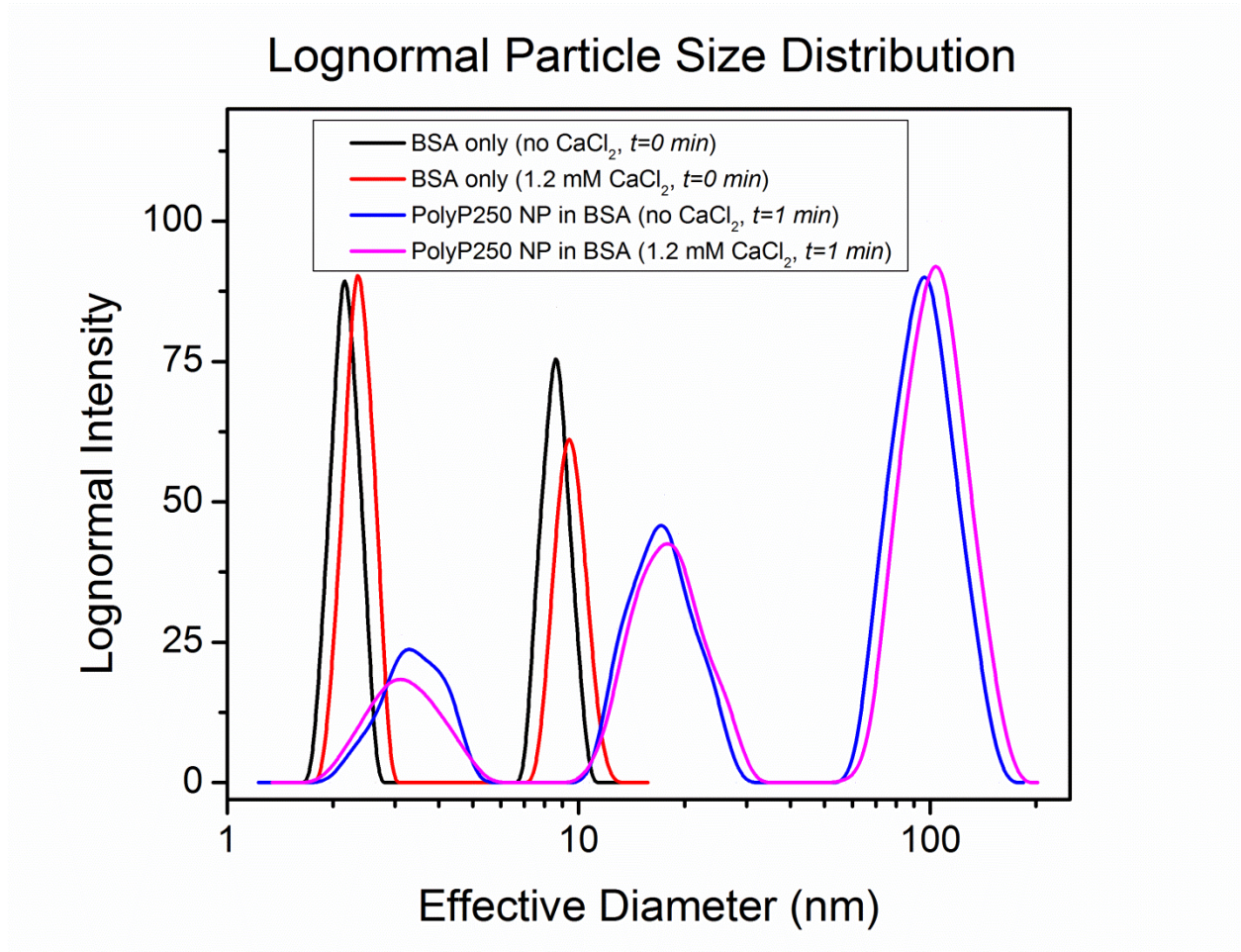


Figure 2.7 Lognormal size distributions for (1) BSA suspension without Ca^{2+} pretreatment; (2) BSA suspension with 1.2 mM CaCl_2 ; (3) immediate addition of polyP 250 NPs in 35 mg/ml BSA without CaCl_2 pre-equilibration; and (4) immediate addition of polyP 250 NPs in 35 mg/ml BSA with 1.2 mM CaCl_2 .

PolyP250 was chosen as a paradigmatic polymer to study nanoparticle stability. First, nanoparticle growth kinetics were examined in an aqueous buffer containing biologically relevant concentrations of ionic calcium for one hour, a time scale approximating a traumatic bleeding event and the half-life of polyP in plasma or serum.¹⁰⁰ PolyP250 was nanoprecipitated in 8 mM Tris·HCl, pH 7.4 with 1.2 mM and 5 mM CaCl₂ (**Figure 2.5**). Particle aggregation behavior follows power law kinetics, typical of metastable colloidal dispersions. Initial particle diameters were 169 nm and 58 nm for 5 mM and 1.2 mM CaCl₂, respectively. This suggests that the phosphate-to-calcium ratio may be the major driving force in the thermodynamic equilibrium of polyP nanoprecipitation. Stoichiometry and polyP supersaturation ratio as it relates to nanoparticle formation will be discussed systematically below. The stability of polyP1000+ NPs precipitated at mildly acid conditions was also examined (see **Figure 2.4**), resembling the environment in acidocalcisomes. The growth behavior manifests power law kinetics identical to physiologic pH. However, the scattering count rate remains more stable.

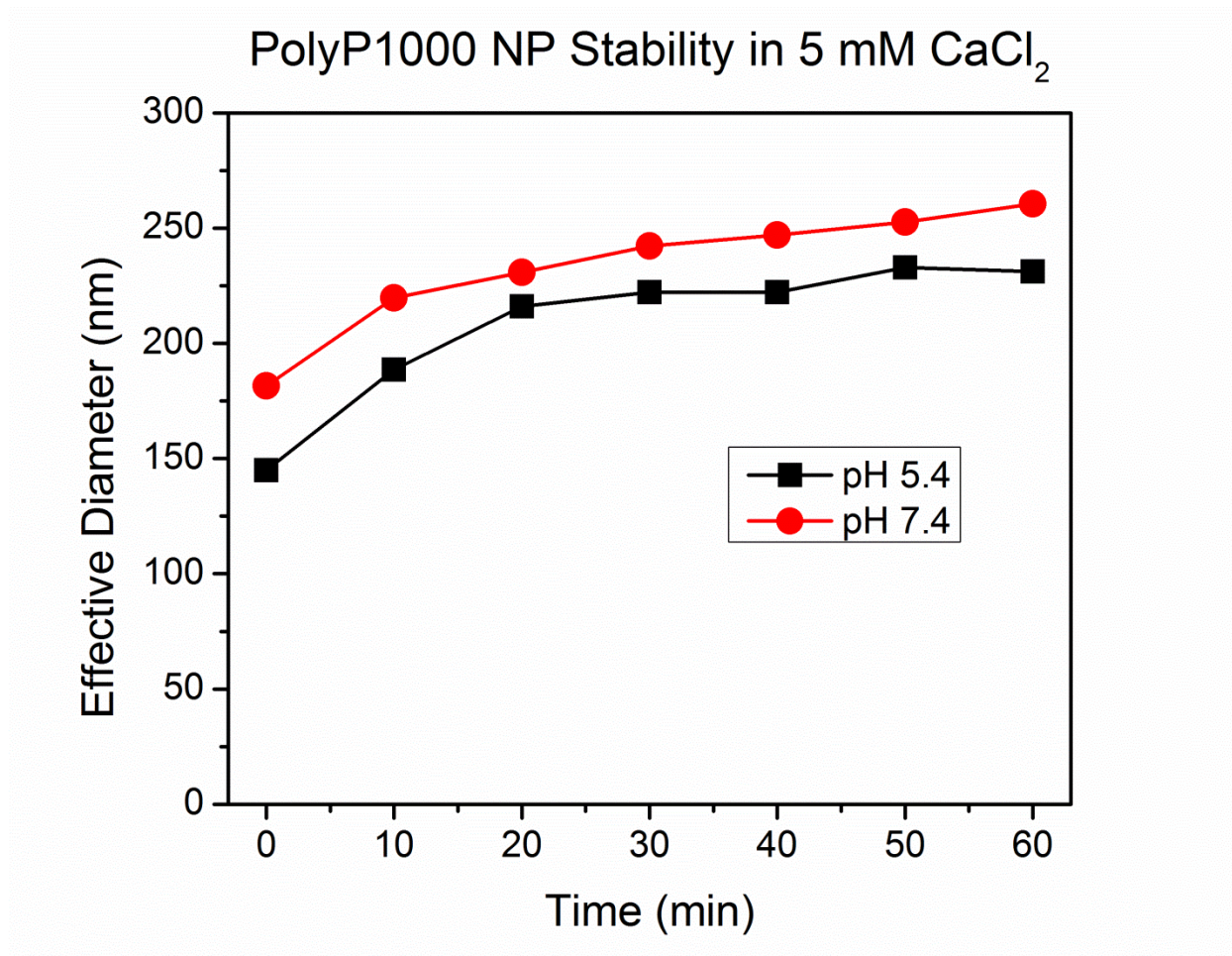


Figure 2.8. Stability of polyP1000+ NPs in acidic and basic conditions. 125 μ M PolyP1000+ was precipitated in 5 mM CaCl₂ in DI H₂O, pH 5.4 or 8 mM Tris·HCl, pH 7.4. Both precipitating conditions lead to initial particle diameters of 150-200 nm and manifest typical power law growth kinetics. The initial difference in size may be due to polyP's pK_a.

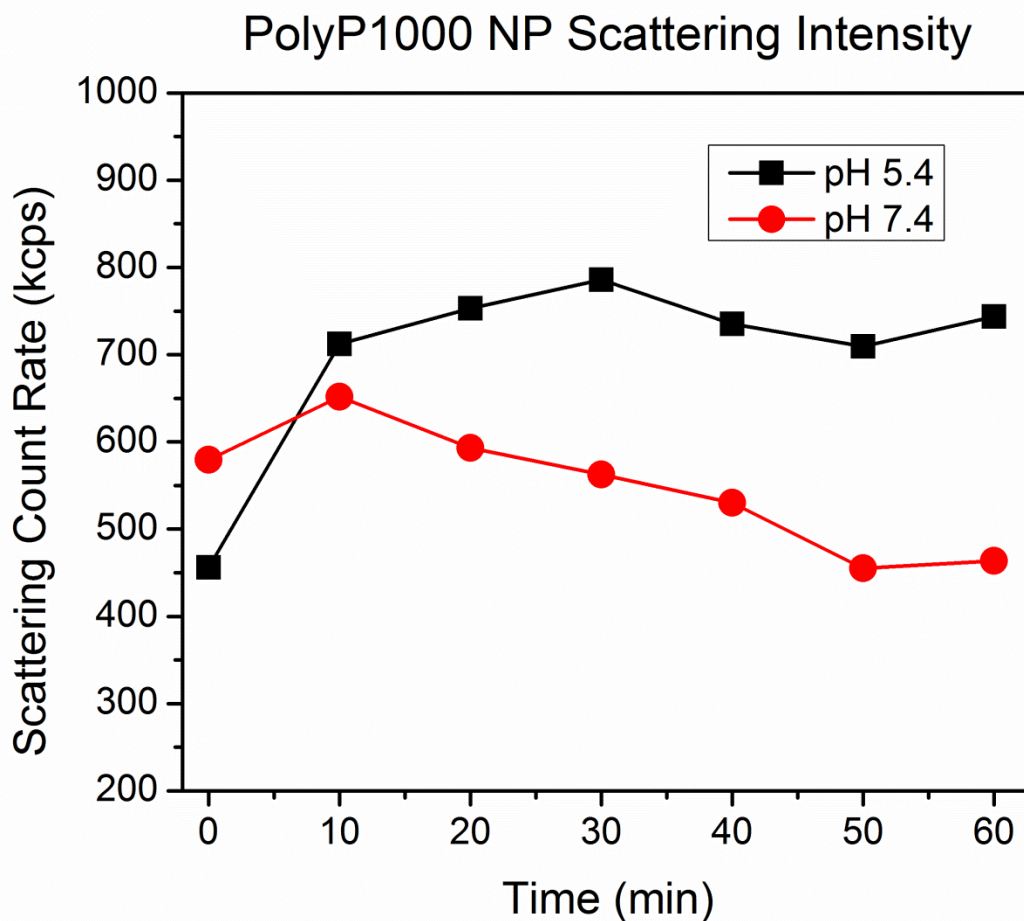


Figure 2.9. Scattering count rates at pH 5.4 and 7.4. The scattering count rate increases in the first 10 min then stabilizes at acidic pH, while at blood's pH the count rate marginally decreases.

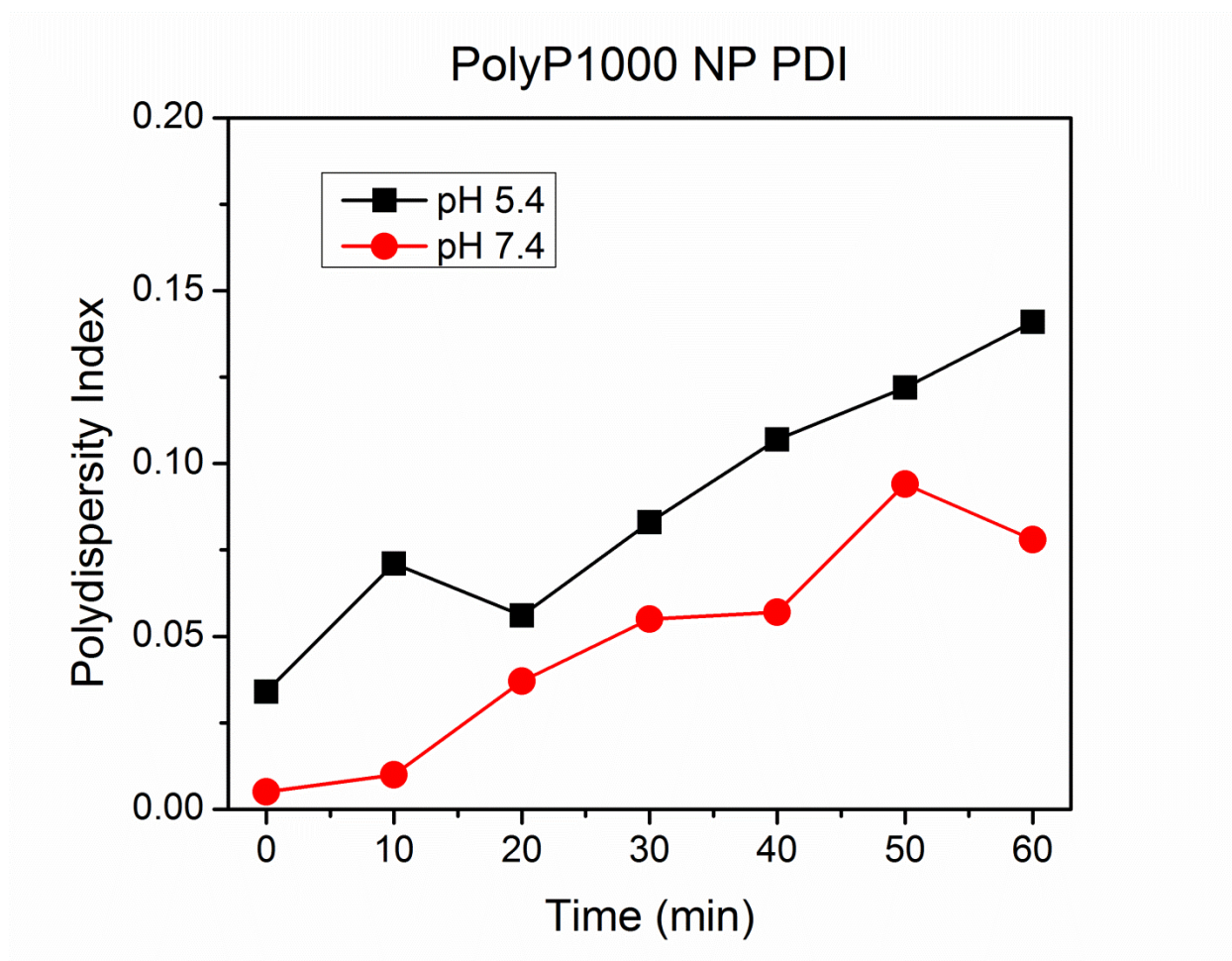


Figure 2.10. Polydispersity index of polyP1000+ NPs at pH 5.4 and 7.4. The polydispersity index (PDI) in 8 mM Tris·HCl, pH 7.4 is exceedingly low, comparable to colloidal standards, remaining less than 0.10 after 1 hr. The particles are slightly more polydisperse at acidic pH.

Aqueous buffer is only a poor approximation of the environment in circulation as it lacks many of the proteins and peptides that contribute to hemostasis and that regulate pH and plasma ionic strength. In addition to examining the nanoparticle growth behavior in aqueous buffer, stability was also investigated in Tris-buffered suspensions containing 35 mg/ml BSA, to better approximate the conditions found in human serum. Serum albumin is the most abundant protein in circulation. It binds to myriad pharmaceuticals and foreign substances,¹⁰² tightly regulates

serum pH,¹⁰³ and robustly and competitively binds to metal cations,¹⁰⁴⁻¹⁰⁹ most notably Ca^{2+} , Zn^{2+} , and Cu^{2+} . Due to BSA's functionality, two conditions were considered for polyP250 NP stability: (1) BSA not pre-equilibrated with CaCl_2 , and (2) BSA pre-equilibrated with 1.2 mM CaCl_2 . Briefly, 125 μM polyP250 NPs were nanoprecipitated in 5 mM CaCl_2 as described previously and mixed 1:1 (v:v) with the BSA suspensions. The particle size evolution was then monitored for three hours (**Figure 2.6**). At both salt conditions, the particles immediately shrank from 170-180 nm to approximately 100 nm when they were added to the BSA suspensions. The shrinkage is too rapid to suggest that this is due to enzymatic degradation. Moreover it is not an artifact of multiple scattering or changes in dispersion viscosity (**Table 2.2**). PolyP250 NPs in BSA not pretreated with CaCl_2 continued to shrink to ca. 50 nm after three hours, whereas the polyP250 NPs in BSA pre-equilibrated with 1.2 mM CaCl_2 maintained approximately the same particle diameter, with the final size after three hours being ca. 80 nm. It is conjectured that serum albumin may extract Ca^{2+} from the polyP- Ca^{2+} complex. However, much further study is needed to prove this claim conclusively.

Sample	PolyP250 NP Effective Diameter (nm)	Dispersion viscosity η^* (centipoise)	BSA volume fraction (ϕ)
125 μ M PolyP250 NP in 5 mM CaCl_2 buffer	165.3	0.89	0.00
PolyP250 NP in BSA (1X = 35 mg/mL)	100.4	1.02	0.0531
PolyP250 NP in BSA (2X diluted)	83.5	0.953	0.0266
PolyP250 NP in BSA (4x diluted)	88.0	0.921	0.0133
PolyP250 NP in BSA (8X diluted)	86.7	0.905	0.00664

* $\eta = \eta_s(1 + 2.5\phi + 6.2\phi^2)$ for dilute BSA suspensions²⁶.

Table 2.2. Absence of multiple scattering effects in BSA suspensions containing PolyP. The effective diameter of 125 μ M PolyP250 NPs in 5 mM CaCl_2 , 8 mM Tris·HCl, pH 7.4 before and after addition to suspensions of Tris-buffered 35 mg/mL BSA suspensions. To verify that multiple scattering was not occurring, the BSA+polyP250 NP samples were serially diluted up to 8 times with 5 mM CaCl_2 , 8 mM Tris·HCl, pH 7.4. As is evident above, the polyP NPs shrink in size by approximately 40% after addition to the BSA suspensions independent of the dispersion viscosity or scattering intensity count rate.

Figure 2.7 shows the lognormal particle population for the following conditions: (1) BSA without Ca^{2+} pre-equilibration; (2) BSA with 1.2 mM CaCl_2 pre-equilibration; (3) immediate addition of 125 μ M polyP250 NPs to BSA not pre-equilibrated with Ca^{2+} ; and (4) immediate addition of polyP250 NPs to BSA pre-equilibrated with 1.2 mM CaCl_2 . BSA without PolyP in the presence or absence of calcium displayed two peaks. The first peak centered around 3 nm represents the hydrodynamic diameter of the BSA monomer. The second peak at

approximately 15 nm constitutes multimeric BSA. The hydrodynamic radius has been previously reported in the literature to be 3.42 nm.¹¹⁰ Quasielastic light scattering data demonstrates that the BSA monomer is a prolate ellipsoid. BSA dimerizes side-to-side, with significant overlap, leading to the dimer being less than twice the size of the monomer.¹¹¹

Addition of CaCl_2 has minimal effects on the size distribution of the BSA protein. The particle populations representing conditions (3) and (4) show that there is an additional peak with a mean diameter of approximately 100 nm. This peak must be the effective diameter of the polyP250 NPs. Moreover, the middle peak representing the BSA dimer has shifted to the right—further evidence that polyP may be interacting directly with BSA and forming an adduct mediated by calcium. The striking discrepancy in the hydrodynamic diameter of the polyP NPs in aqueous buffer and in BSA suspension deserves special scrutiny. Further study is needed to measure PolyP- Ca^{2+} binding constants at these conditions to corroborate the hypothesis that the evolution in polyP particle diameter, characterized first by a steep drop and then a gradual shrinkage over a time scale of hours, is due to a competitive equilibrium process governed by the differential Ca^{2+} binding affinities of BSA and polyP.

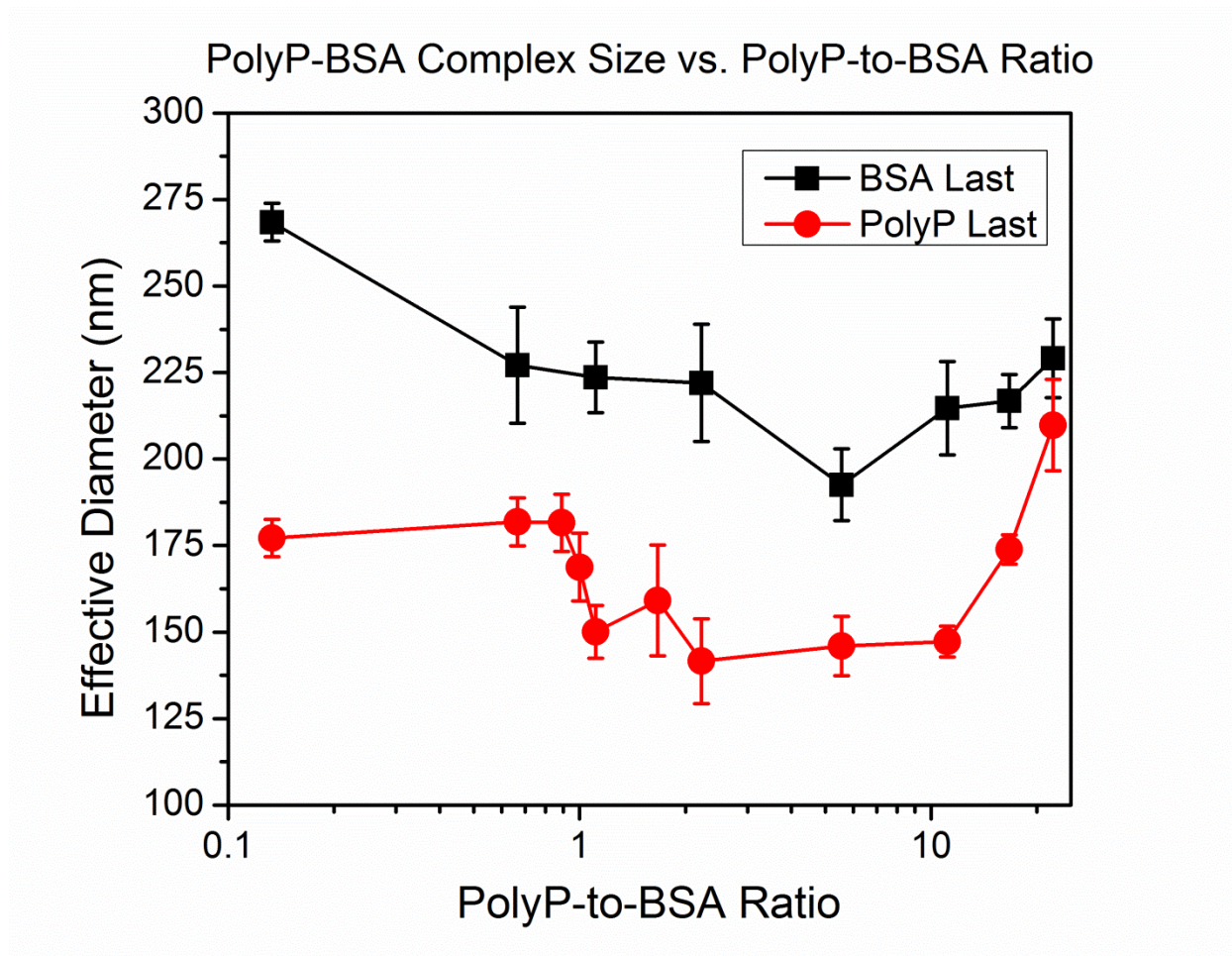


Figure 2.11. Hydrodynamic diameter of polyP-BSA complexes at various polyP-to-BSA molar ratios. As well as precipitating polyP in BSA suspensions pre-equilibrated with CaCl_2 (noted as *PolyP Last*), the order of addition was reversed to interrogate the assembly thermodynamics by pipetting BSA suspension into a suspension of granular polyP NPs in CaCl_2 (noted as *BSA Last*). The polyP-BSA particle size does not significantly differ from granular polyP NPs in 5 mM CaCl_2 across the entire the spectrum of polyP-to-BSA ratios evaluated.

The phenomenon of BSA and polyP interaction in the presence of calcium cations is further explored in more dilute BSA suspensions. PolyP-BSA complexes were synthesized by addition of molecularly dissolved polyP to BSA pre-equilibrated in aqueous calcium chloride. In

the second protocol, the order was reversed so that BSA was added to a suspension of granular polyP NPs. The thermodynamics of self-assembly may be altered by reversing the order of polyelectrolytes. The final calcium and polyP concentrations for both protocols were maintained at 5 mM, while the BSA concentration was varied. PolyP-BSA complexes were formed at molar ratios of polyP45 to BSA from 0.13 to 22.2. **Figure 2.11** gives the hydrodynamic diameter of polyP-BSA complexes synthesized by both protocols. The size of polyP-BSA complexes across the entire range of polyP-to-BSA ratios does not differ appreciably from granular polyP NPs nanoprecipitated in 5 mM CaCl_2 , suggesting that the thermodynamics of self-assembly do not vary upon reversing the order of addition of the polyelectrolytes.

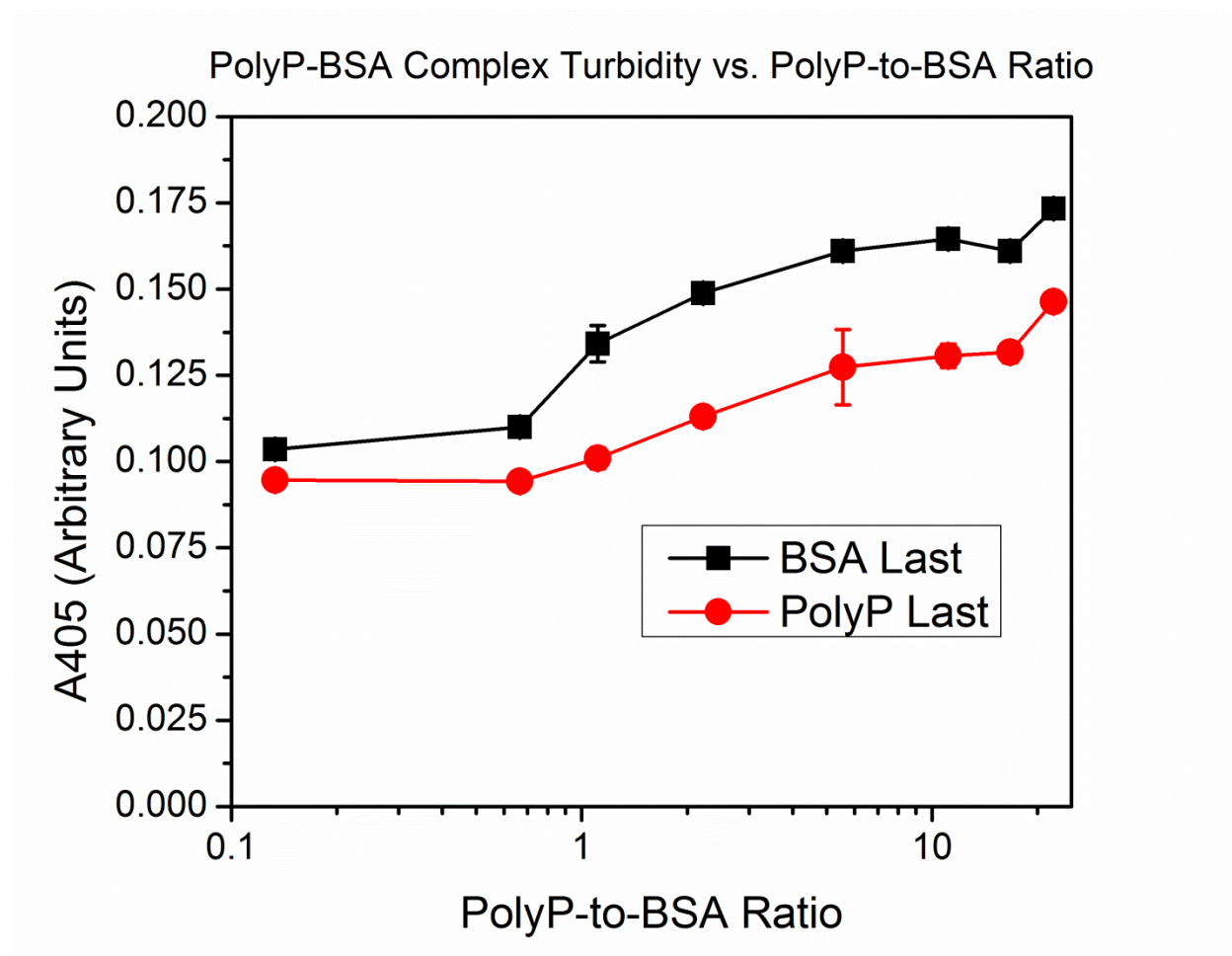


Figure 2.12. PolyP-BSA complex optical turbidity at 405 nm (A_{405}) for various polyP-to-BSA ratios. Increasing the BSA concentration while maintaining the same concentrations of polyP and CaCl_2 (*decreasing* the polyP-to-BSA ratio) causes the light scattering to diminish. BSA may be competing with polyP for calcium cation chelation and leading to dissolution of the polyP granules.

The optical turbidity at 405 nm (A_{405}) for the polyP-BSA complexes was also studied to gain further insights into competitive calcium binding by the two anionic polyelectrolytes and its ramifications on particle formation and dissolution. **Figure 2.12** shows that polyP-BSA samples with higher BSA concentrations and equivalent polyP and calcium cation concentrations (lower polyP-to-BSA ratios) for both protocols scatter less light. This may indicate that the presence of BSA is involved in a competitive equilibrium process with polyP centered on calcium cation coordination. In other words, BSA may perturb the ionic calcium concentration to an extent that it shifts the thermodynamics of polyP granule self-assembly to particle dissolution toward the molecularly dissolved form.

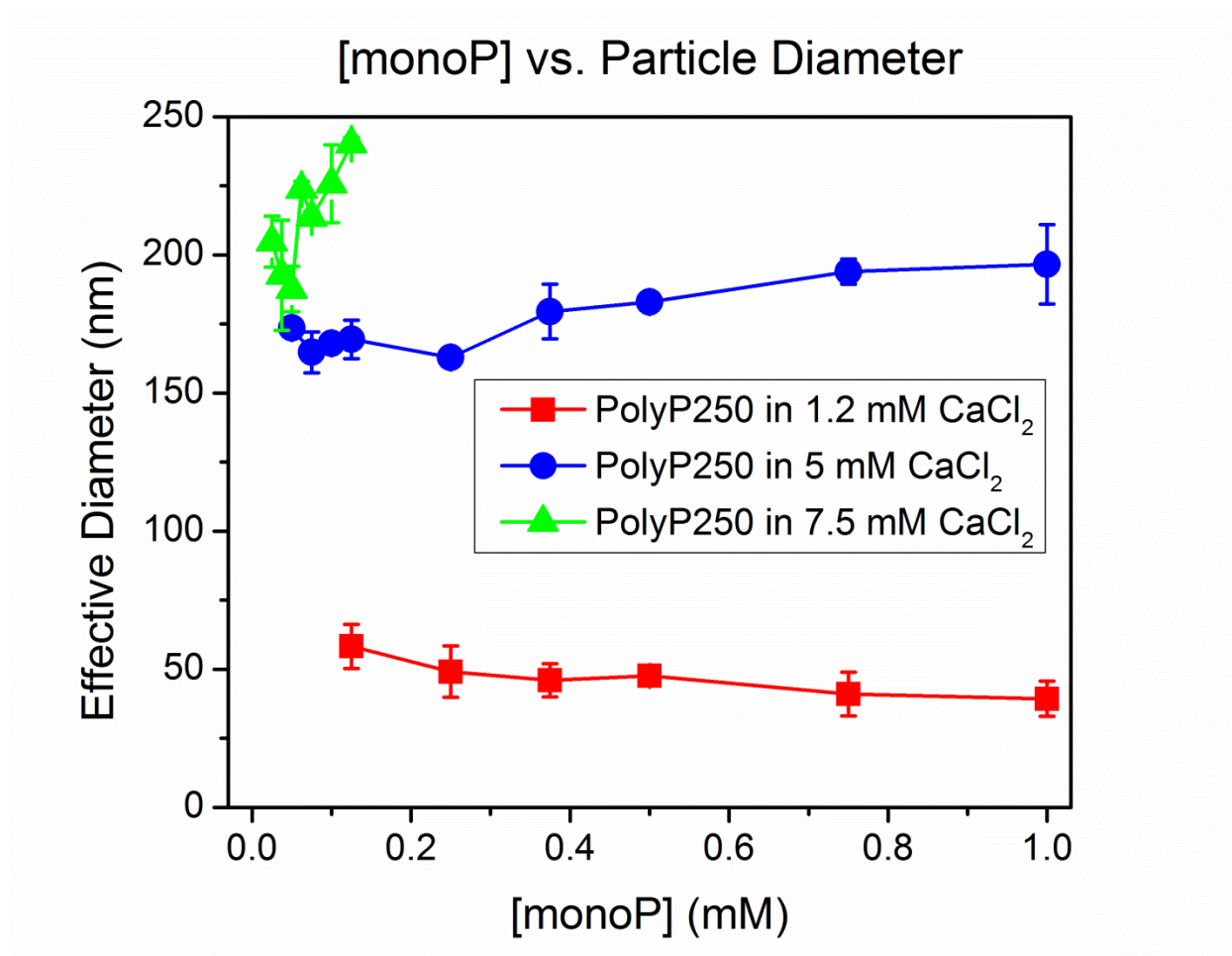


Figure 2.13. PolyP250 NP initial effective diameter versus monoP and Ca^{2+} concentrations.

Initial polyP250 NP sizes were measured with up to 1 mM monoP concentration at three different calcium concentrations: 1.2, 5, and 7.5 mM Ca^{2+} . No trends are manifest except for a dependence on calcium concentration.

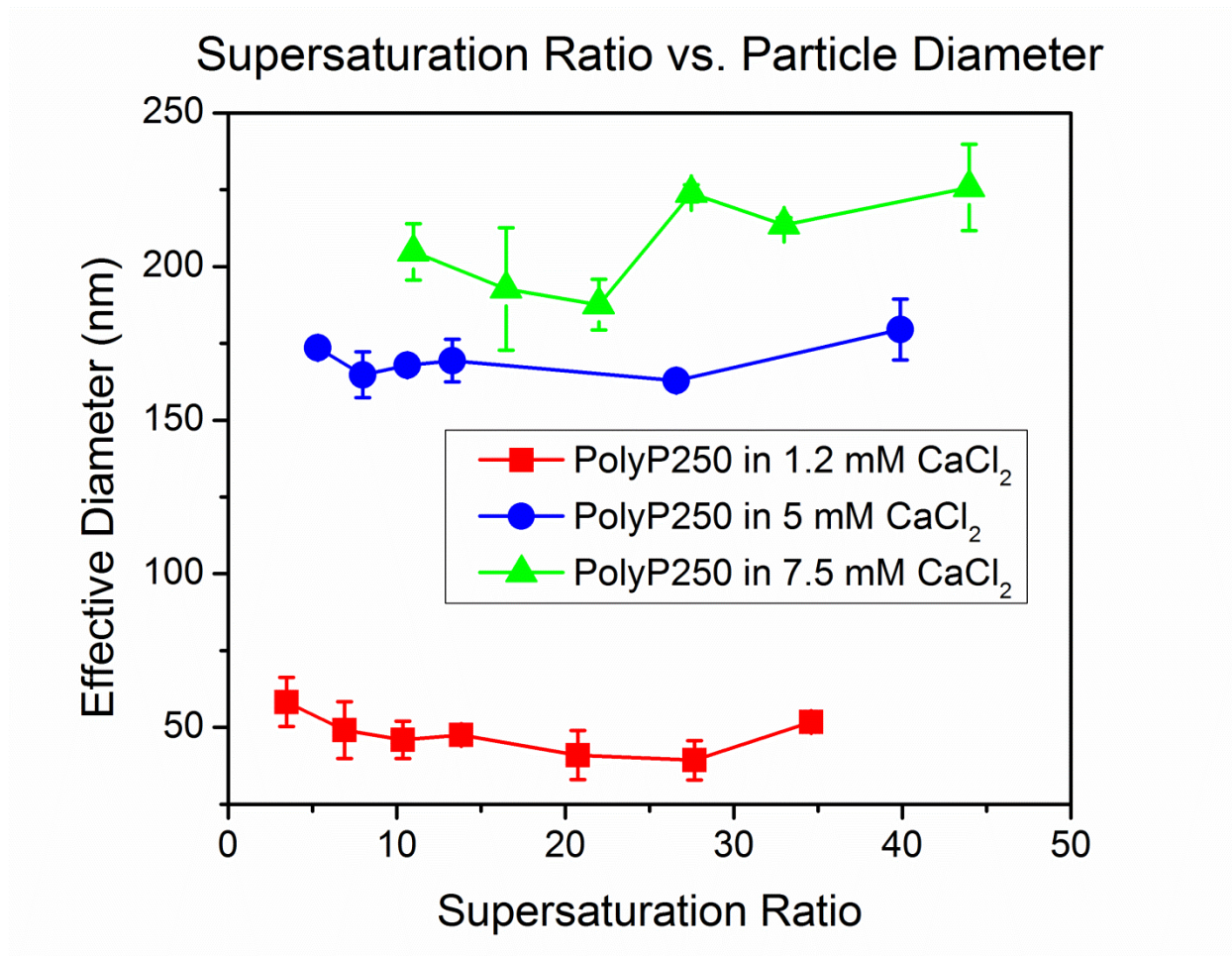


Figure 2.14. PolyP250 NP initial effective diameter as a function of supersaturation ratios and Ca^{2+} concentrations. When the monoP concentrations are divided by the solubility of polyP250 at the respective calcium concentrations, it appears that at moderate supersaturation ratios (~ 1 -50), the polyP particle diameter is only a function of the calcium concentration.

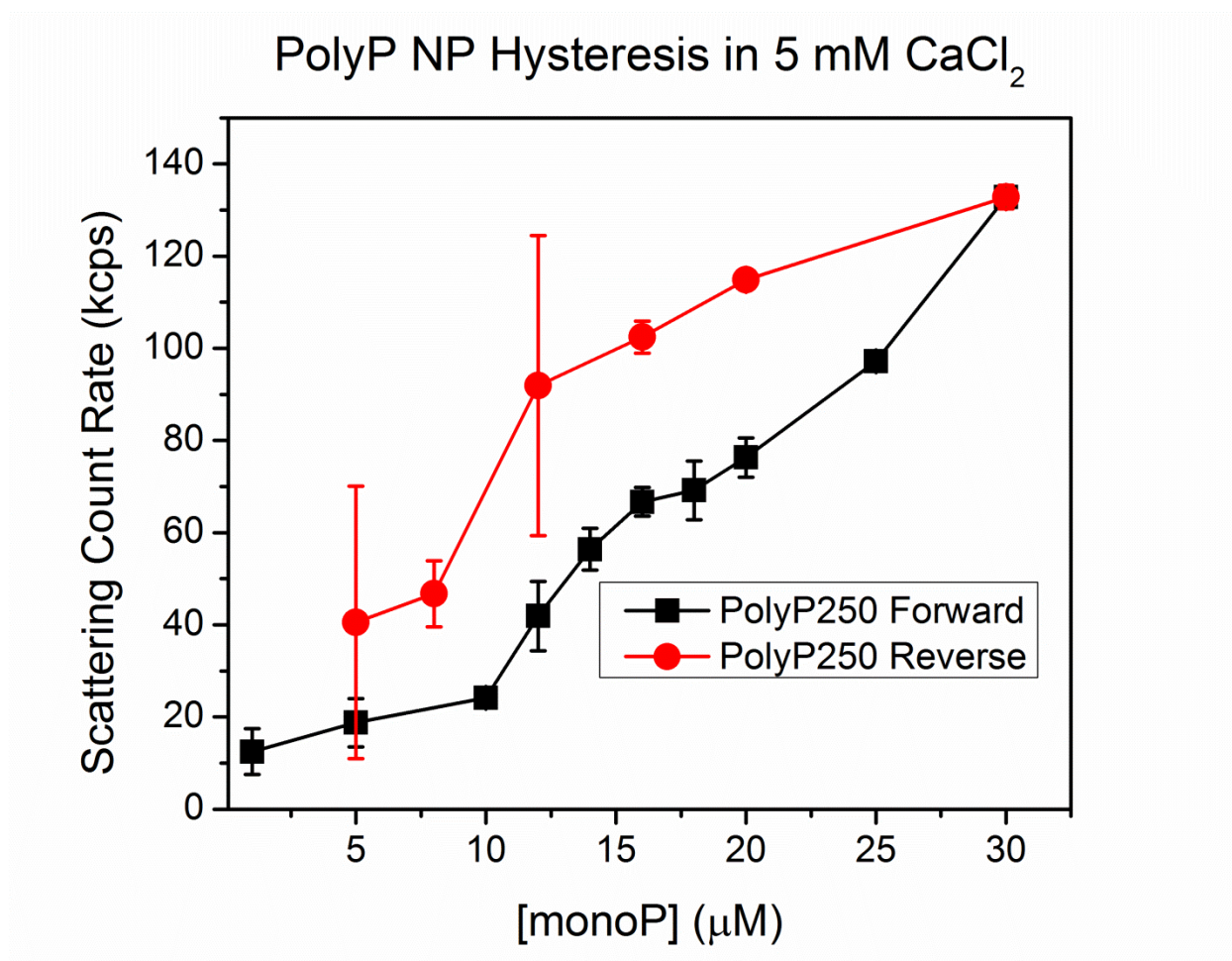


Figure 2.15. PolyP NP solubility hysteresis. 30 μM polyP250 was nanoprecipitated in 5 mM CaCl_2 , generating a supersaturated colloidal dispersion of polyP250 NPs. The suspension was then serially diluted with 5 mM CaCl_2 , 8 mM Tris·HCl, pH 7.4 in order to decrease monoP concentration, while maintaining constant $[\text{Ca}^{2+}]$. As is evident from the reverse solubility curve (shown in red above), the scattering intensity remains elevated, even approaching polyP250's solubility (9.4 μM) in 5 mM CaCl_2 despite a thermodynamic driving force for resolubilization. This suggests that polyP colloidal dispersions manifest hysteresis, a characteristic that may have profound ramifications for potential downstream therapeutic usage of polyP NPs as clotting agents.

The initial effective diameter of the polyP granular NPs was systemically investigated against the polymer's supersaturation ratio at three different calcium concentrations: 1.2 mM (calcium concentration in human serum), 5 mM (calcium concentration in *in vitro* coagulation assays), and 7.5 mM. **Figure 2.13** shows the particle size plotted against monoP concentrations up to 1 mM for intermediate-length polyP (polyP250). PolyP precipitated in 5 mM CaCl₂ at monoP concentrations of 250 μ M or greater had to be diluted with more Tris-buffered 5 mM CaCl₂ solution before being characterized by DLS (polyP NP diameter is hysteretic after dilution; see **Table 2.3**). No trends between particle diameter and monoP concentration are manifest at first glance until the monoP concentration is divided by the solubility of polyP250 at the given calcium concentration and plotted nondimensionally as the supersaturation ratio, as in **Figure 2.14**. At low to moderate supersaturation ratios (\sim 1-50) the particle size is only a function of the calcium concentration.

Sample	Effective Diameter (nm)	Dilution Factor
125 μ M PolyP250	158	1
62.5 μ M PolyP250	146	2
25 μ M PolyP250	161	5
12.5 μ M PolyP250	147	10

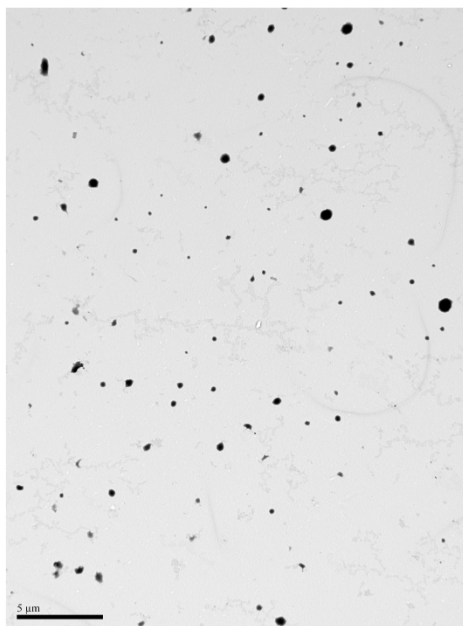
Table 2.3. PolyP250 NP effective diameter is hysteretic. 125 μ M polyP250 was precipitated in 5 mM CaCl₂, 8 mM Tris·HCl, pH 7.4 and immediately diluted 2X, 5X, and 10X. The effective diameter does not appreciably change above the solubility for polyP250 (9.4 μ M).

After it was established that the solubility of polyP250 was 9.4 μ M in 5 mM CaCl₂, 8 mM Tris·HCl, pH 7.4, a sample well above the solubility concentration (in this case 30 μ M) was diluted progressively with more 5 mM CaCl₂ to decrease the polyP concentration and keep the

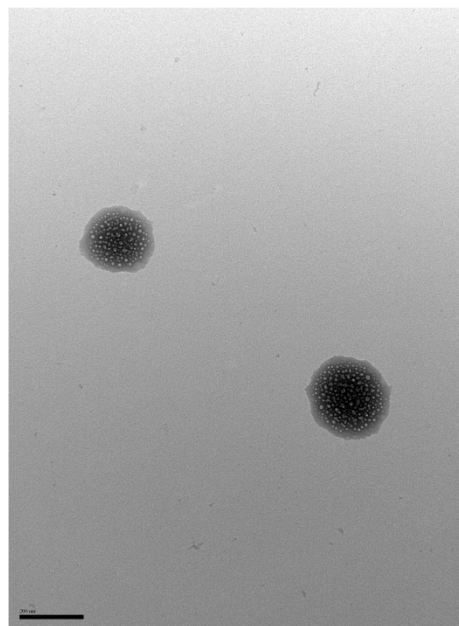
calcium concentration constant, and the scattering intensity was measured after each dilution. As can be seen in **Figure 2.15**, the system exhibits hysteresis: the count rate remains much higher even below the solubility concentration despite a thermodynamic driving force for some of the particles to resolubilize. Evidence that polyP NP formation manifests dilution-dependent hysteresis has potentially profound ramifications: for example, a bolus of condensed polyP could be delivered to a trauma site at locally high concentrations and be dispersed further downstream in the circulation without losing its NP format due to its hysteretic behavior, maintaining its associated biological functionality as a procoagulant and proinflammatory agent. However, in human serum other mechanisms may come into play, such as binding of polyP to membrane-associated proteins on vessel walls adjacent to thrombi, which may prevent polyP NPs from being convected away from the wound site, thereby curtailing a potentially disastrous or even fatal scenario.

We have found that polyP exerts its most robust procoagulant effects at roughly 10 to 500 μM when assayed at 5 mM CaCl_2 .³³ Indeed, this concentration range almost exactly corresponds to a supersaturation ratio of 1-50 for PolyP250 at 5 mM Ca^{2+} . However, at physiological calcium concentration, the particle diameter for this polymer length is roughly constant between 36 μM – 1.8 mM. One could speculate that organisms have specifically developed techniques to store and condense polyP in subcellular compartments such as acidocalcisomes and platelet dense granules in a controlled manner by exploiting polyP's roughly constant particle diameter at low to moderate supersaturation ratios. Upon secretion, these polyP precipitates could potentially serve as concentrated stores of the polymer for biochemical processes requiring rapid, non-linear, or threshold-switchable behavior such as coagulation or quorum sensing.

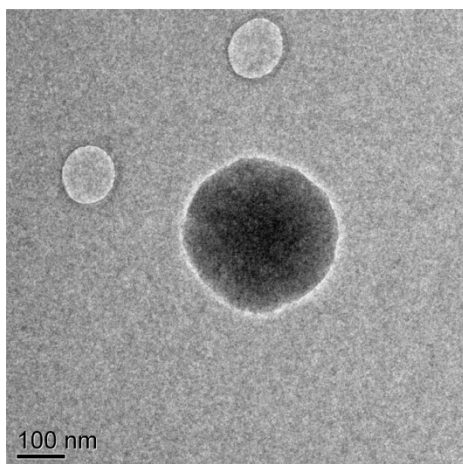
A



B



C



D

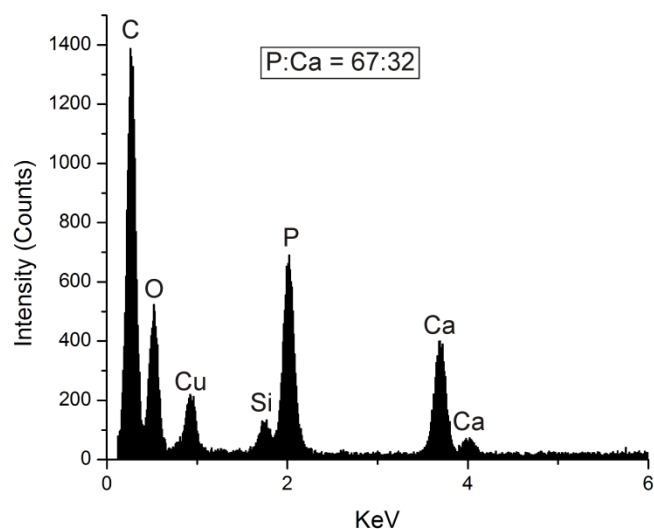


Figure 2.16. PolyP NP morphology, structure & elemental composition. *A*: PolyP forms monodisperse particles in solution. 125 μM polyP250 was precipitated in 5 mM CaCl_2 , 8 mM Tris·HCl, pH 7.4. PolyP250 forms monodisperse particle populations in the presence of 5 mM CaCl_2 . Scale bar: 5 μm . *B*: PolyP NPs appear spongy after prolonged electron beam exposure just like acidocalcisomes and platelet dense granules. Even though polyP250 NPs

are uniformly electron dense, after sustained exposure to the electron beam, white spots begin to appear so that the particles appear like round sponges or porous balls. This same phenomenon was also observed in Ruiz *et al.*'s investigation¹¹² of polyP-containing dense granules in platelets. **C: A granular polyP250 nanoparticle.** A single polyP 250 NP is shown at higher magnification revealing that the granule is roughly spherical and approximately 200-250 nm in diameter, in good agreement with DLS data. Scale bar: 100 nm. **D: Elemental composition of the synthetic polyP250 NPs.** Copper, carbon, and silicon are from the grid. The ratio of the phosphorous to the calcium peak is 67:32. Ruiz *et al.* performed the equivalent analysis with human platelet dense granules, and their resulting X-Ray microspectrum is quasi-identical, except for the presence of a small K peak.¹¹² However, potassium was not used here for polyP nanoprecipitation.

Transmission electron microscopy was used to examine the polyP particle structure, elemental composition, and morphology. **Figure 2.16A** is an electron micrograph taken at low magnification with a large population of polyP250 NPs, showing that the granules are spherical in shape and relatively monodisperse, despite the presence of some larger aggregates. The particle diameter is a function of the calcium concentration; inevitably, some aggregation is bound to occur during the drying process and grid preparation. When the particles undergo substantial exposure from the electron beam, the polyP250 NPs develop white spherical spots, resulting in the granules resembling round sponges or soccer balls, despite their uniform electron density as seen in **Figure 2.16B**. Indeed, Ruiz *et al.* has shown using TEM that polyP bodies in acidocalcisomes and human platelet dense granules also appear spongy after bleaching with the electron beam, resembling the polyP NPs synthesized here.¹¹²

Figure 2.16C shows a single polyP250 nanoparticle at high magnification. The polyP granule is spherical and approximately 200-250 nm in diameter, corroborating DLS data. **Figure 2.16D** is an X-Ray microspectrum of the particle in *C* showing its elemental composition. Copper, carbon, and silicon are from the grid. It is very typical for X-Ray microspectra to have small peaks (~1-2%) of Si and alkali earth metals arising from the detector itself or, more rarely, from silicon-containing oils deposited on the Formvar® grids during the manufacturing process. In fact, a small Si peak was also observed in the X-Ray microanalysis of human platelet dense granules in the past.¹⁸ The P:Ca ratio is 67:32. Ruiz *et al.*, in their investigation of human platelet dense granules, also determined the elemental composition of the polyP bodies, yielding very similar results.¹¹² The P:Ca was 1.76 with trace amounts of K⁺. However, dense granules are mildly acidic subcellular compartments, which may lead to a different P:Ca stoichiometry, and platelets contain substantial cellular stores of potassium.¹¹³ Potassium was not used here to precipitate polyP into synthetic polyP granules.

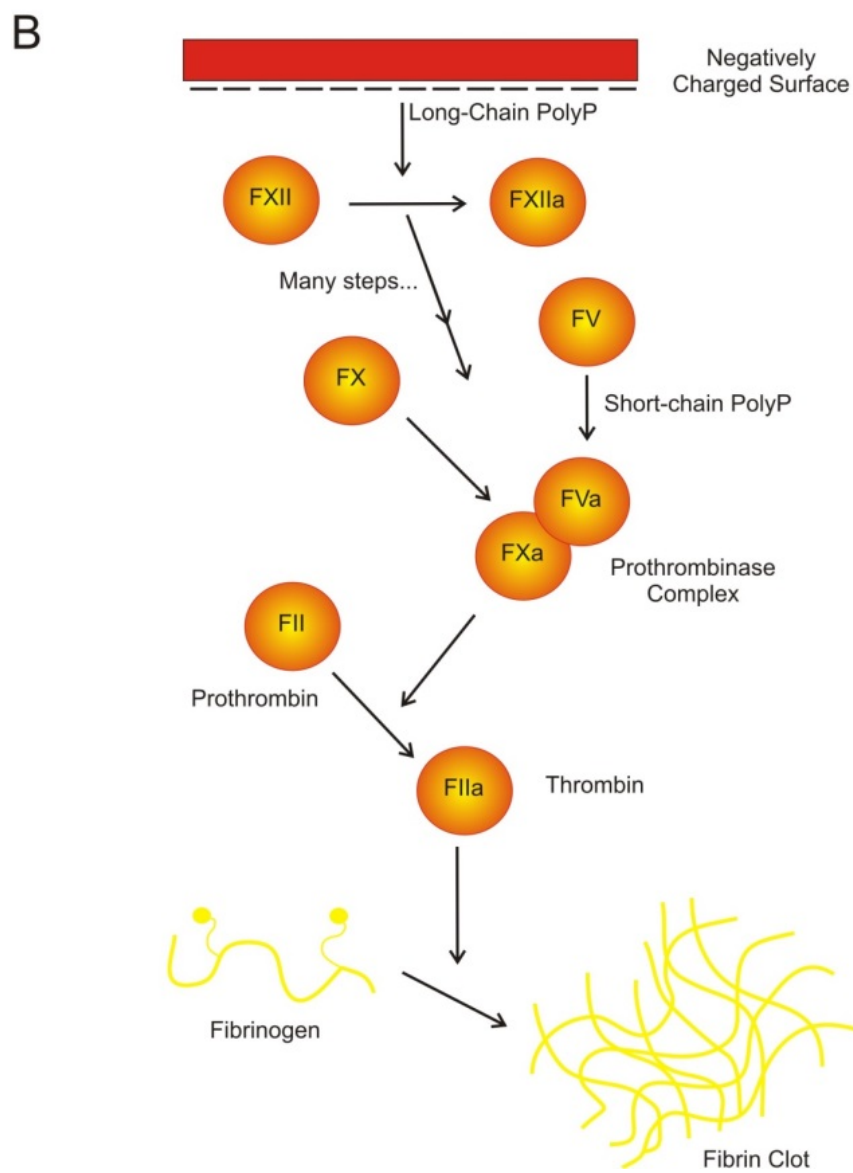
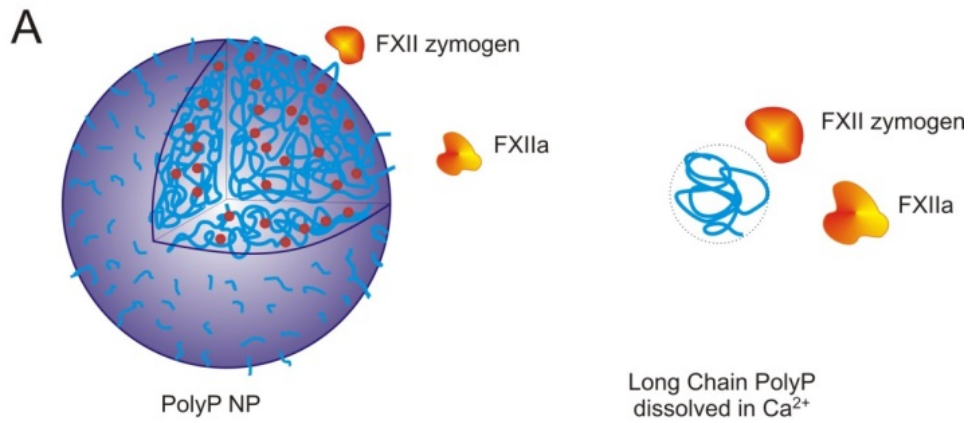


Figure 2.17. PolyP NPs as contact activators. A. Possible mechanisms by which polyP exerts its contact pathway activity. PolyP could serve as a surface for FXII activation as a colloidal particle like kaolin (left) or as a soluble anionic polymer like dextran sulfate (right) with a threshold molecular weight needed to elicit a conformational change in the FXII zymogen. **B: Schematic of the intrinsic pathway of blood coagulation.** A negatively charged surface serves as the site for assembly of the primary complex consisting of FXII, kallikrein, and high molecular weight kininogen. Long-chain polyP is able to support activation of the contact pathway, while shorter polymer lengths (like those in human platelets) are weak contact activators. PolyP also exhibits procoagulant effects further downstream in the final common pathway of blood clotting.

Smith *et al.* demonstrated that polyP is a potent activator of the contact pathway of coagulation, and its activity is related nonlinearly with its polymer length,³³ with long polymers being more robust activators than shorter chains, which exert their effects at different points in the cascade such as via acceleration of FV activation and alteration of fibrin clot architecture and morphology. **Figure 2.17B** shows a schematic representation of the intrinsic pathway of coagulation and the points in which polyP exerts its effects. It is well accepted in the literature that anionic “surfaces” such as collagen, glass or kaolin are required to form the primary complex consisting of FXII (Hageman Factor) and its activation partners, plasma prekallikrein and high molecular weight kininogen (HMWK)⁵⁰. However, countless other soluble substances serve as scaffolds for the (auto)activation of FXII. Examples include ellagic acid, lipopolysaccharides, dextran sulfate, and phospholipids.¹¹⁴ It has been reported previously that there exists a threshold molecular weight for activation of the intrinsic pathway for polystyrene

polymers and dextran derivatives, with contact activity for both polymer types rising sharply ~25,000 Da.¹¹⁵ Others have communicated that the threshold molecular weight for dextran sulfate is as low as 10,000 Da.¹¹⁶ Nonetheless, the mechanism by which polyP acts on FXII has yet to be clearly elucidated.

Previous studies assaying the procoagulant effects of polyP were performed under conditions where the polymer would presumably exist in its molecularly dissolved state. Typically, polyP was incubated together with pooled normal plasma (PNP) for 3-5 minutes prior to recalcification. Since the plasma is citrated, there would be very little ionic calcium available to chelate polyP, and thus no calcium-dependent precipitation would take place. The activation of contact enzymes and the generation of FXIIa are calcium-independent; therefore prior studies investigating polyP's contact activity are confined to an examination of the polymer in the absence of calcium-dependent precipitation. Moreover, plasma contains countless proteins and peptides such as serum albumin which may prevent or hinder its precipitation after recalcification. Due to polyP's role in the early stages of natural selection, pre-dating the arrival of polypeptides and quite possibly serving as the precursor to deoxyribonucleic and ribonucleic acid, it is only natural that polyP would serve as the paradigmatic anionic scaffold for serum and cytosolic proteins, emerging as a favored binding partner for peptides with cationic amino acid residues.

Figure 2.20 shows the clotting time of polyP molecules or nanoparticles when assaying for contact activity using citrated PNP. The polyphosphates (PolyP80, PolyP305, and PolyP1000+) were first added to 5 mM CaCl₂, 8 mM Tris·HCl, pH 7.4 at three times the final assay concentration and characterized by DLS (data not shown). Once the polyP was incubated with the calcium solution, it was added to the PNP and immediately recalcified to initiate

coagulation. Platelet-size polyP (polyP80) weakly shortened time to clot formation, saturating near 10-50 μM monoP. PolyP305 and polyP1000+, on the other hand, were robust contact activators, drastically reducing clotting times even at sub-micromolar concentrations. Interestingly, the clotting activities of the two longer polymer sizes are quasi-identical (the error bars overlap for every concentration except one).

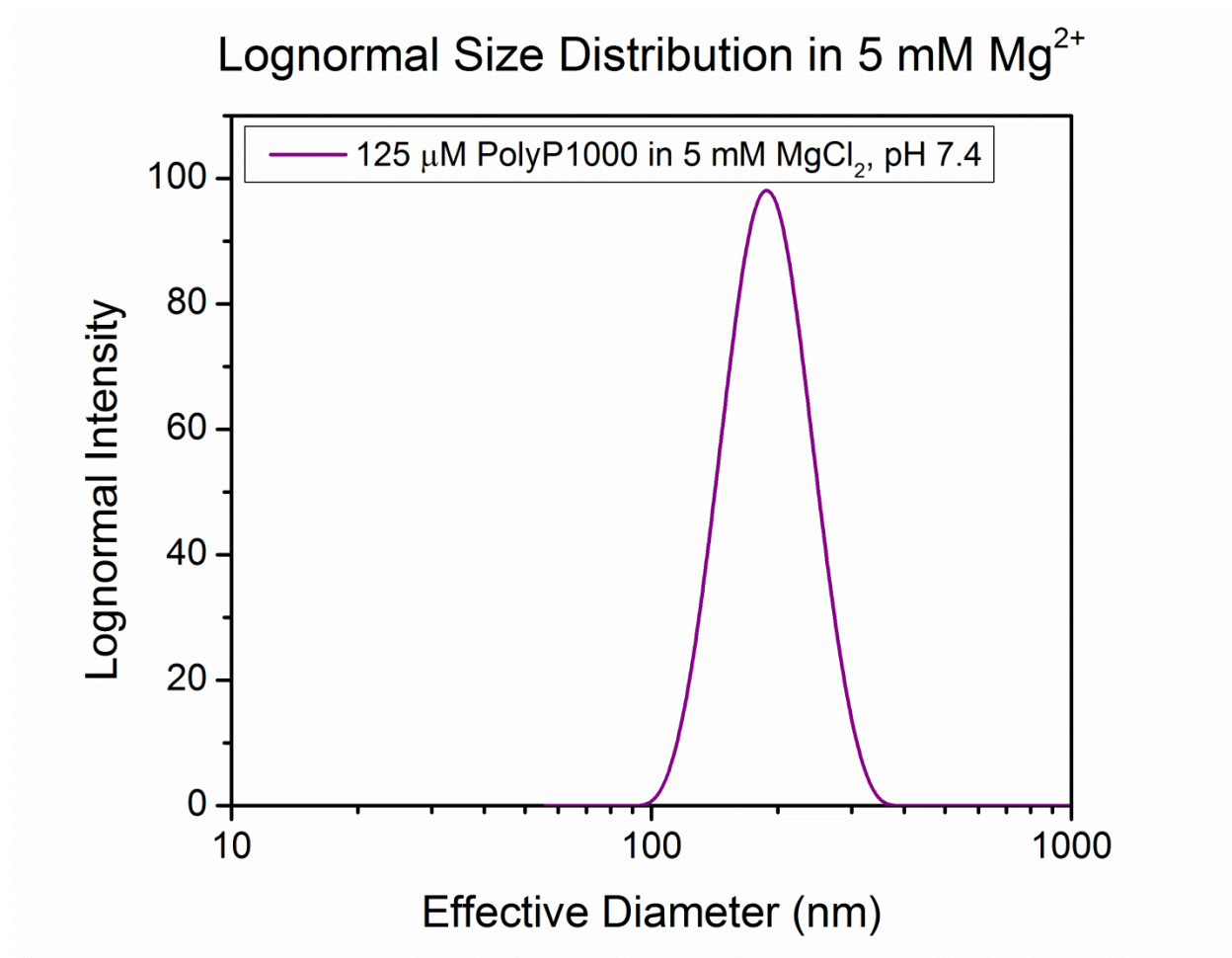


Figure 2.18. Lognormal particle size distribution of polyP1000+ in 5 mM Mg²⁺ only. 125 μM polyP1000+ was precipitated in 5 mM MgCl_2 , 8 mM Tris·HCl, pH 7.4 in the absence of ionic calcium, yielding monodisperse nanoparticles approximately 180 nm in diameter, comparable to polyP precipitates synthesized in 5 mM CaCl_2 alone. Interestingly, polyP305 and polyP80 could not be precipitated at equivalent monoP and Mg^{2+} concentrations, implying that

ionic magnesium's influence on polyP precipitation is an even more highly nonlinear function of polymer size in relation to calcium's exerted effects (data not shown). Moreover, polyP1000+ could not be precipitated at 0.4 mM MgCl_2 , pH 7.4 (ionic $[\text{Mg}^{2+}]$ in blood) (data also not shown).

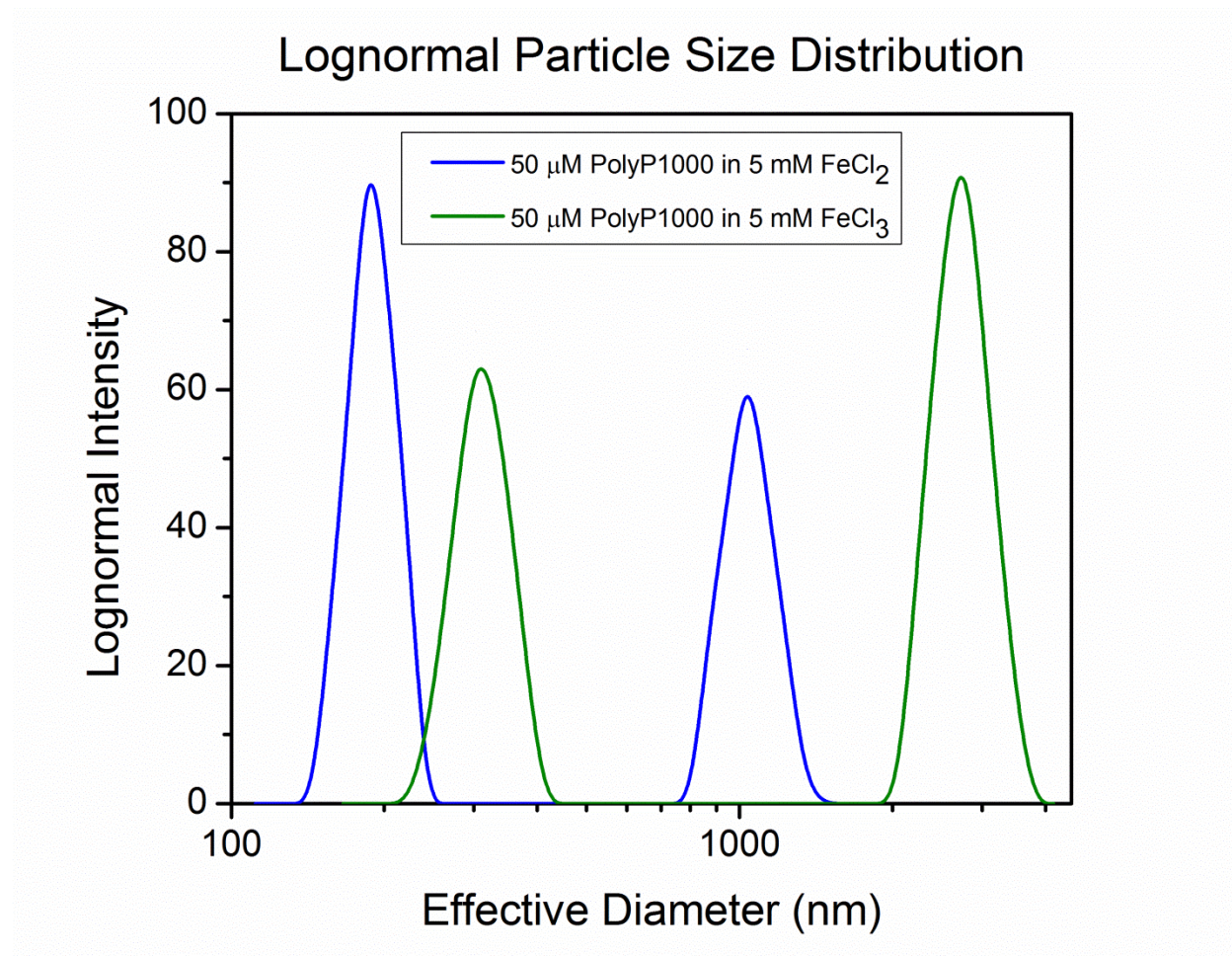


Figure 2.19. Particle size distribution of polyP1000+ precipitates in $\text{Fe}^{2+}/\text{Fe}^{3+}$. 50 μM polyP1000+ was precipitated in DI H_2O , pH 5.4 with either 5 mM FeCl_2 or 5 mM FeCl_3 . Both conditions lead to bimodal particle populations. In the case of Fe^{2+} , there are particles approximately 180 nm in diameter, with a smaller population approximately one micron in

diameter. Fe^{3+} produces particles that are several hundred to several thousand nanometers in size, suggesting that increasing cation valency leads to bigger precipitates.

These data suggest that platelet polyP only weakly promotes the activation of FXII, with the reduction in clotting time deriving mostly from effects on the final common pathway of clotting. On the other hand, the longer polymer sizes are large enough to serve as scaffolds for primary complex formation after treatment with calcium. One possibility is that there is a threshold polymer length (molecular weight) (as was previously reported for polystyrene and dextran sulfate) needed to exert the conformation change on the FXII zymogen (or to recruit a sufficiently high local surface density of FXII and its activators) as shown in **Figure 2.17A**.

Interestingly, polyP305's molecular weight is approximately 24 kDa, corroborating past results on threshold contact activation measured using polystyrene and dextran sulfate polymers. The fact that the concentration dependence is identical for polyP305 and polyP1000+ also suggests that the nanoparticle solubility is not the threshold condition for contact pathway activation for polymers over the threshold size, as polyP1000+'s solubility is approximately two-fold lower in 5 mM CaCl_2 . If the solubility were the limiting condition, then polyP1000+'s clotting time would drop at $\sim 4 \mu\text{M}$, whereas polyP305's would drop at $\sim 9 \mu\text{M}$. However, there are several important caveats that limit the completeness of this analysis: (1) polyP NPs have been shown to exhibit dilution-dependent hysteresis; (2) the solubility of polyP in plasma or serum with its diversity of proteins and peptides and additional polyvalent cations such as Mg^{2+} , Cu^{2+} , Zn^{2+} , Mn^{2+} , and $\text{Fe}^{2+}/\text{Fe}^{3+}$ (see **Figures 2.18 & 2.19**) could be vastly different than in aqueous buffer containing only calcium; and (3) the effect of citrate and other calcium chelators such as EDTA on polyP nanoparticle stability has yet to be investigated.

Polymer Length (range, phosphate units)	Mean Zeta Potential in mV \pm S.E.	Mean Particle Effective Diameter in nm \pm S.D.
BKGP70 (20-125)	-16.53 \pm 3.83	159.55 \pm 3.32
PolyP250 (100-390)	-17.89 \pm 3.69	169.40 \pm 6.97
PolyP1000+ (>1000)	-15.41 \pm 0.53	162.50 \pm 11.46

Table 2.4. Average zeta potential and effective diameter of polyP NPs precipitated at 125 μ M monoP in 5 mM CaCl₂, 8 mM Tris·HCl, pH 7.4. The zeta potential is approximately -15 to -20 mV irrespective of polymer length. The average initial effective diameter is approximately 160 nm regardless of the polymer molecular weight, being only a function of the calcium concentration.

Precipitating Condition	Mean Zeta Potential in mV \pm S.E.	Mean Particle Effective Diameter in nm \pm S.D.
5 mM CaCl ₂ , 10 mM NaCl, pH 5.4	-14.94 \pm 1.54	170.20 \pm 2.55
5 mM CaCl ₂ , 10 mM NaCl, 8 mM Tris·HCl, pH 7.4	-19.28 \pm 1.15	177.30 \pm 4.38
1.2 mM CaCl ₂ , 10 mM NaCl, 8 mM Tris·HCl, pH 7.4	-15.72 \pm 0.65	47.80 \pm 4.81

Table 2.5. Average zeta potential and effective diameter of 125 μ M polyP1000+ NPs synthesized at various precipitating conditions. The mean zeta potential is again in the range of -15 to -20 mV. The potential does not change substantially as a function of [Ca²⁺], with the surface charge at physiologic calcium being comparable to 5 mM CaCl₂.

The zeta potential of the polyP NPs was determined to be between -15 and -20 mV independent of particle diameter and polymer length (see **Tables 2.4 & 2.5**). The negative surface charge of PolyP precipitates could therefore conceivably support autoactivation of Factor

XII or recruitment of its activators, plasma prekallikrein and high molecular weight kininogen independent of polymer molecular weight, discounting other factors that would influence polyP NP stability in human plasma mentioned above.

Regardless of the physical interpretation, the fact remains that polyP precipitation under aqueous conditions at physiologic salt concentrations is a facile means to synthesize large amounts of condensed PolyP granules similar in structure to human platelet dense granules for potential downstream uses such as a biocompatible procoagulant agent.

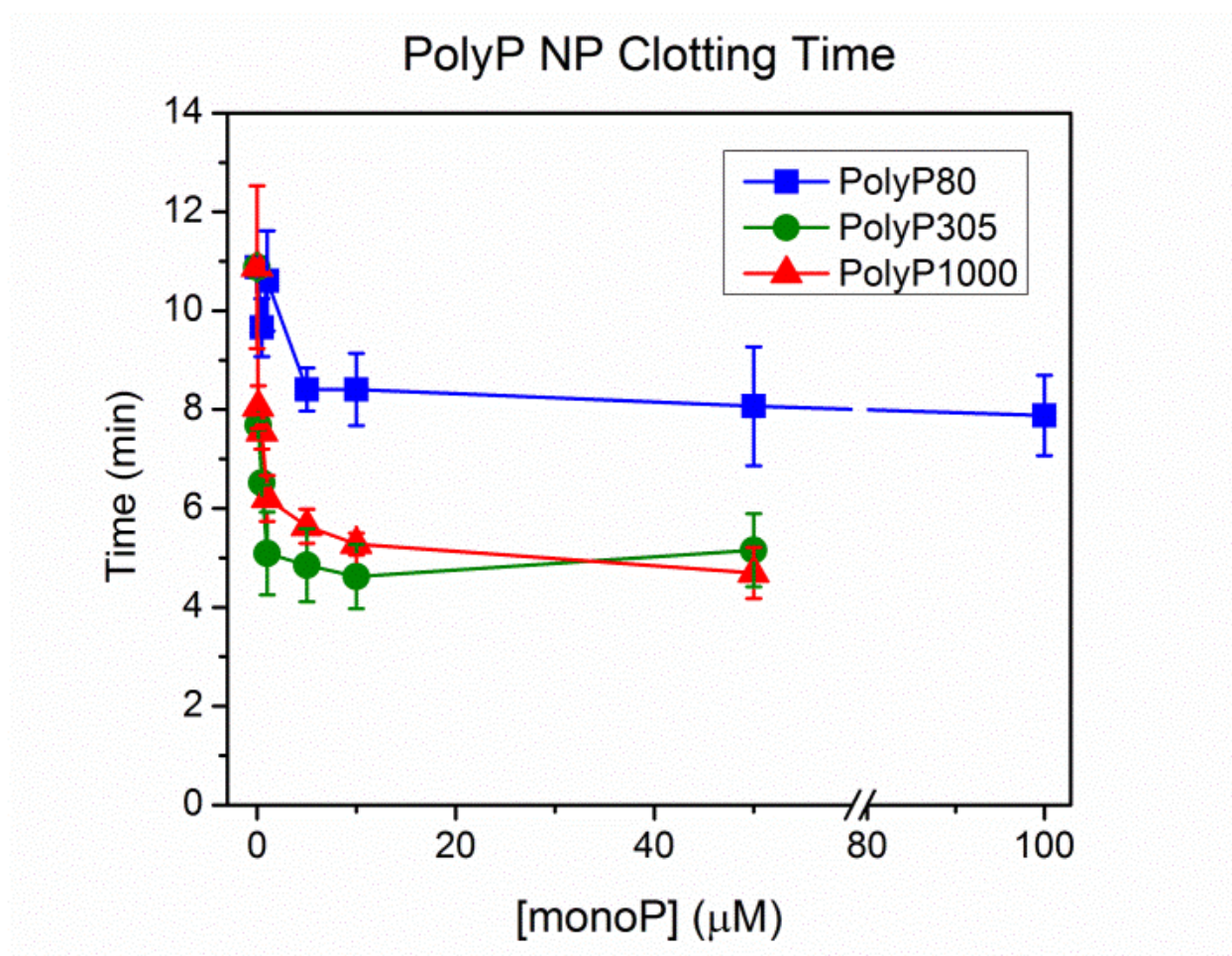


Figure 2.20. Initiation of the contact pathway by polyP based on polymer length and concentration. Clotting time of polyP is plotted as a function of monoP concentration from 0-100 μM. PolyP was added to 5 mM CaCl₂, 8 mM Tris·HCl, pH 7.4 at concentrations above and below its solubility. The presence of precipitated polyP was monitored by DLS before addition to plasma. Intermediate- and very long-chain length polyP (polyP305 and polyP1000+) are clearly more robust contact activators than platelet-sized polyP (polyP80). The concentration dependence on clotting time for polyP305 and polyP1000+ are identical, suggesting that a “saturating condition” has been established.

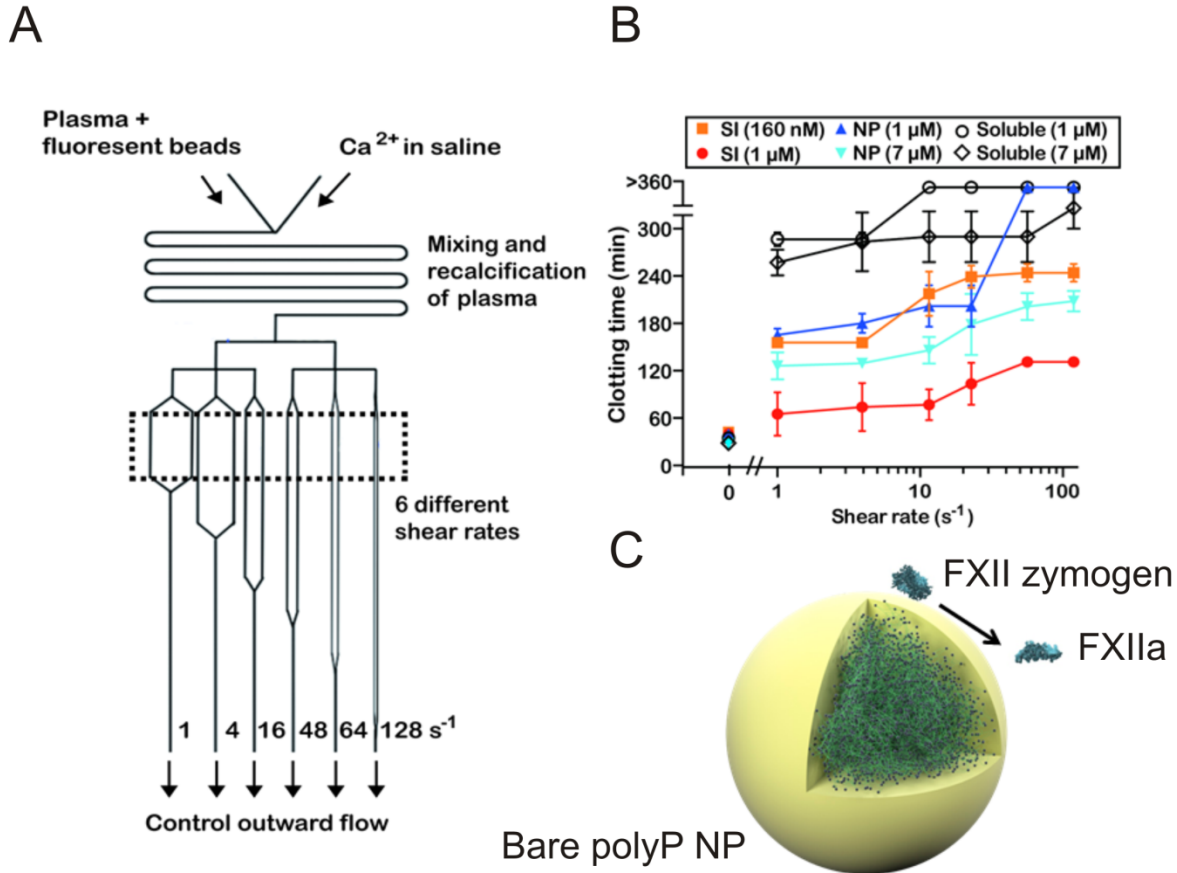


Figure 2.21. A: Microfluidic device for measuring procoagulant behavior of polyP NPs at physiologic and pathophysiologic shear rates ($1\text{--}128\text{ s}^{-1}$) simultaneously. Citrated PNP is mixed with CaCl_2 buffer and rapidly recalcified in a tortuous, serpentine channel before the channel branches into multiple outlets with various widths for determination of clotting time at shear rates varying across two orders of magnitude. **B: Bare polyP160 NPs (NP) exert threshold-switchable procoagulant activity as a function of shear rate.** When plasma is nearly static, an environment that approximates the flow conditions near a catastrophic hemorrhage site, polyP produces a significant decrease in the clotting time compared to control, whereas at higher shear rates typical of normal venous flow, polyP160 NPs are not nearly as

procoagulant compared to control with no activator present. **C: Cartoon of granular polyP NPs autoactivating FXII by serving as a negatively charged, templating surface.**

In addition to evaluating the procoagulant behavior of bare polyP NPs under static (no flow) conditions, the ability for the granular particles to induce coagulation as a function of shear rate was also investigated. Collaborating with Dr. Christian Kastrup's research group at University of British Columbia, we investigated the effects of polyP localization on the hemostatic agent's ability to form fibrin clots by examining two other forms employing polyP of equivalent polymer length: molecularly dissolved (in the absence of precipitative metal cations) and confined to the microfluidic channel walls (surface-immobilized).¹¹⁷ Two inlet channels containing citrated pooled normal plasma (PNP) and fluorescent beads (as a tracer) and 50 mM calcium chloride in 150 mM NaCl, respectively, were homogeneously mixed in a serpentine winding channel to rapidly recalcify the plasma and initiate clotting. The bare polyP160 NPs were added to the calcium chloride buffer. **Figure 2.21A** shows a schematic of the microfluidic device that is capable of measuring coagulation at shear rates of $1\text{--}128\text{ s}^{-1}$, flow conditions that span the nearly stagnant pooling of blood characteristic of catastrophic hemorrhaging ($\sim 1\text{ s}^{-1}$) and more typical venous flow rates ($\sim 100\text{ s}^{-1}$) absent any coagulopathy.¹¹⁸ The rectangle outlined by the dotted line encompasses the length of the channel where the shear rate was varied. **Figure 2.21B** contrasts the ability of molecularly dissolved, nanoparticulate, and surface-immobilized polyP160 to generate fibrin clots at the various flow conditions. The ability of polyP160 NPs to completely occlude the microfluidic channel is manifested by a sigmoidal curve, indicating that the granular particles are potent procoagulant agents at low shear rates, e.g. 1 s^{-1} , while they are weakly activating at typical venous flow rates.¹¹⁷ **Figure 2.21C** is a cartoon of granular polyP

NPs acting as a templating surface for the autoactivation of FXII zymogen, the preliminary step in the initiation of the contact pathway of clotting. These microfluidics experiments create the groundwork for evaluating the clotting ability at physiologic and pathophysiologic flow conditions for downstream hemostatic drug delivery platforms incorporating granular polyP NPs.

Conclusion

Herein, we demonstrate the size-controlled synthesis of monodisperse polyP NPs at physiological concentrations of calcium and magnesium. The solubility is related nonlinearly to the polymer length, with very long-chain polyP precipitating much more facilely than platelet polyP. Further, the NP size is only a function of the calcium concentration across a wide supersaturation range. The granules are stable for at least an hour in aqueous buffer solutions, displaying typical power-law growth kinetics, and are stable in BSA suspensions for three hours.

The polyP NPs possess promising procoagulant activity. Given that the polyP particles are stable on the same time scale as a catastrophic bleeding event raises the question that polyP's powerful procoagulant effects on the intrinsic pathway may be related to its precipitation into micron or sub-micron granular particles serving as negatively charged surfaces for FXII activation. The facile, size-controlled synthesis of these particles in the laboratory serves as a foundation for the future development of targeted procoagulant nanotechnologies exploiting polyP precipitation to mitigate the effects of a diversity of bleeding phenomena such as internal hemorrhage and hemophilia in a minimally invasive manner.

CHAPTER 3. BIONSPIRED ARTIFICIAL PLATELET NANOPARTICLES

The text in this chapter was originally published in part as Donovan, A.J. *et al.* “Artificial dense granules: a procoagulant liposomal formulation modeled after platelet polyphosphate storage pools.” *Biomacromolecules* **2016**, 17(8): 2572-2581.

3.1 Introduction

Hemorrhagic events arising from trauma in either the civilian or military setting contribute to a significant proportion of avoidable fatality.^{2, 119, 120} In countless combat scenarios proper management of hemorrhage is not immediately feasible without invasive surgical intervention. Topical hemostatic wound dressings and other pharmacological agents, which can be delivered on-demand on the battlefield, are therapeutically inferior in mitigating internal, incompressible bleeding sources.¹²¹

Clinical guidelines created to diminish poor outcomes in patients experiencing an uncontrolled post-traumatic bleeding event have focused on restoring normal circulatory perfusion to the wounds after swiftly determining and suppressing the source of bleeding by a trained clinician rather than via administration of a hemostat as a first-line therapy.^{122, 123} However, these guidelines have largely failed to eradicate trauma-related complications even in developed countries with relatively more medical resources.¹ Both private and public entities have invested heavily into developing a targeted, on-demand, broad-spectrum procoagulant agent.¹²¹ The FDA has approved a myriad of pharmacological therapies in recent years to address external compressible trauma, enhancing survival and reestablishing hemostasis without surgery.⁶⁴ Factor VIIa is one such example of a recombinant coagulation protein that has been used to treat internal bleeding.¹²⁴ However, the efficacy of factor VIIa therapy for treating traumatic injuries is controversial.⁵⁷ The recombinant clotting factor is expensive and requires special storage and handling conditions.

Nanoscale drug delivery has emerged as a novel therapeutic platform in recent decades with the potential to drastically transform medical treatment,¹⁴ promising reduced side effects, enhanced efficacy, and targeted delivery to only effected organs and tissues.¹²⁵ The conventional strategy to design this next generation of smart drugs entails the encapsulation of therapeutic and/or imaging agents into supramolecularly assembled depots¹²⁶ such as phospholipid vesicles,¹⁸ polymersomes,^{20, 127} viral capsids,¹²⁸ polymeric micelles,¹²⁹ and other self-assembled nanostructures.¹³⁰ Among these candidate drug architectures, vesicles have garnered the most tangible success, with several liposomal nanoformulations being approved by the FDA to treat a myriad of disorders, especially cancer.^{23, 131} The liposomal envelope of these smart drugs usually contains a small molar percentage of poly(ethylene glycol)-phosphatidylethanolamine (PEG-PE), which is used for steric stabilization and long blood circulation time.^{132, 133}

Given both the limitations of the available treatments to improve hemostasis and the promise of nanotherapeutics, numerous candidate nanoparticle hemostats have been developed in recent years. These nanotherapeutics attempt to imitate at least some aspects of platelet morphology and the procoagulant response adjacent to the bleeding site. Platelet-like nanoparticles (PLNs) were synthesized by alternative deposition of the polyelectrolytes bovine serum albumin (BSA) and poly(allylamine) hydrochloride on a polystyrene (PS) core.^{26, 134} Further functionalization of the PLN with targeting peptide ligands allow PLNs to accumulate at the bleeding site, bind and interact synergistically with the body's own activated platelets, and rapidly induce coagulation at the site of trauma.²⁶ However, the synthesis of the PLNs involves multiple steps and toxic organic solvents to dissolve the nonbiodegradable polymer.

Inorganic polyP, on the contrary, is virtually omnipresent in biology and degradable in human blood plasma on therapeutic time scales.³¹ The polymer is often stored intracellularly in a

precipitated form as ~250 nm granules^{40, 135, 136} in conjunction with calcium and other divalent and multivalent cations. These subcellular phosphate-containing bodies are called dense granules in human platelets⁴⁰ due to their uniformly high electron density. Their contents are secreted upon platelet activation, where they exert potent procoagulant and proinflammatory effects,¹³⁷ especially on Factor V³³ and thrombin-promoted Factor XI activation.³⁴ We have previously shown that polyP self-assembly into granular NPs in the presence of physiological amounts of metal cations is thermodynamically controlled, and that these particles retain their robust procoagulant effects.¹³⁵

Herein we envision a biomimetic procoagulant nanoparticle composed of a granular polyP NP core encapsulated in a sterically stabilized liposome, which we call an Artificial Dense Granule (ADG). The ADG assembly process is scalable and highly reproducible, and there are no toxic organic solvents or nonbiodegradable materials involved. The size distribution of the ADGs was characterized by DLS measurements. Electron microscopy techniques demonstrate that the ADGs are virtually indistinguishable from dense granules isolated from human platelets in terms of morphology and structure,⁴⁰ consisting of a 150 nm uniformly dense core surrounded by a 200 nm shell. Electron energy loss spectroscopy (EELS) confirms the co-localization of P, Ca, and O in the core and P, C and O in the phospholipid lamella. The ADGs are procoagulant as demonstrated by *in vitro* clotting factor assays. The ADGs can be triggered to initiate FXII autoactivation, the initial step in the contact pathway of blood clotting, via enzymatic hydrolysis by phospholipase C (PLC), which modulates platelet degranulation. Furthermore, ADGs manifest contact activity in human plasma, and are roughly equivalent to molecularly dissolved, long-chain polyP at physiologically relevant concentrations.

3.2 Experimental Section

3.2.1 Materials and reagents

CaCl₂·6H₂O, phospholipase C (PLC) from *Clostridium perfringens* (*C. welchii*), and secretory phospholipase A₂ from honey bee venom (bvsPLA₂) were purchased from Sigma-Aldrich (St. Louis, MO). Water was deionized using a Nanopure II filtration system (Barnstead, Dubuque, IA) to 18.2 MΩ-cm. 1,2-dipalmitoyl-sn-glycero-3-phosphoethanolamine-N-[methoxy(polyethylene glycol)-2000] (ammonium salt) (PEG_{2k}DPPE), L-α-phosphatidylcholine (L-α-PC), and Avanti® Mini Extruder Kit, together with a 200-nm pore-diameter polycarbonate membrane, were purchased from Avanti Polar Lipids (Alabaster, AL). Citrated human pooled normal plasma (PNP) from thirty healthy donors was purchased from George King Biomedical (Overland Park, KS). The polyP preparation used throughout for synthesis of ADGs was Natriumpolyphosphat P70 (BKGP70, approximate range 20-125 phosphate units, mode ~45) from BK Guilini GmbH (Ludwigshafen am Rhein, Germany). PolyP_{>600} ('long chain polyP') used in clotting assays, and polyP_{>1000}, used to synthesize "Artificial Acidocalcisomes," were size-fractionated as previously described by differential isopropanol precipitation.³³ All materials were purchased at standard grades and used as received.

3.2.2 Synthesis of Sterically Stabilized Liposomes

Sterically-stabilized liposomes (~200 nm) composed of 95 mol% L-α-PC/ 5 mol% PEG_{2k}DPPE were synthesized by standard protocol via extrusion⁹⁹ through a 200-nm pore-diameter polycarbonate membrane. Briefly, 14.3 µl of 25 mg/mL PEG_{2k}DPPE and 76.1 µl of 25 mg/mL L-α-PC (both dissolved in chloroform) were micropipetted into a 7 mL glass scintillation vial and dried under a gentle stream of Argon gas. The dried lipid film was then placed under vacuum for an additional 60 min to remove any residual traces of organic solvent. The desiccated lipid cake was subsequently rehydrated with 1 mL of filtered, deionized H₂O (DI H₂O) and

stored for up to two weeks at 4°C. Liposome effective diameter and polydispersity index (PDI) were characterized by DLS after rehydration.

3.2.3 *Synthesis of ADGs*

5 mM polyP NPs were synthesized as described above. Following precipitation the bare NP effective diameter, polydispersity, and scattering intensity were characterized by DLS before addition of 106.6 μ l of 2.6 mM 200-nm L- α -PC/PEG_{2k}DPPE liposomes in DI H₂O. The dispersion was bath sonicated for 10 min to encapsulate the granular polyP NPs at high efficiency.

3.2.4 *FXII Autoactivation Assay with Detergent*

FXII autoactivation was measured in 96-well microplates as described previously¹³⁸ with some small modifications. In short, ADGs were synthesized at 5 mM [monoP] in 5 mM CaCl₂, pH 5.4 as delineated in *Synthesis of ADGs* above. The ADGs were diluted with more 5 mM CaCl₂, pH 5.4 after solubilization with 0.5 % (v:v) Tween 20 or an equivalent volumetric amount of pure DI H₂O (as a control) to a final monoP concentration of 500 μ M. Final concentrations of FXII zymogen and S-2302 substrate were 50 nM and 0.5 mM, respectively. FXII autoactivation was measured at room temperature.

3.2.5 *FXII Autoactivation Assay with PLC from C. welchii*

In lieu of solubilization with Tween 20, the 5 mM ADGs were prepared, as above, and diluted into 5 mM CaCl₂, 10 μ M ZnCl₂, 0.1% bovine serum albumin (BSA), 5 mM Tris·HCl, pH 5.5, and preincubated with 30 μ g/ml PLC for 20 minutes at 37°C before addition of FXII zymogen and S-2032 chromogenic substrate. BSA was added as a carrier protein for maximal PLC activity. Final concentrations of ADG, FXII zymogen and S-2302 substrate were 500 μ M, 50 nM and 0.5 mM, respectively. FXII autoactivation was measured at room temperature.

3.2.6 Determination of PolyP NP Encapsulation Efficiency

A facile assay was devised employing DLS to measure the stability of ADGs after modulation of $[Ca^{2+}]$ with and without the presence of surface-active agents which would disrupt phospholipid vesicular integrity. Bare granular polyP NPs and ADGs at equivalent monoP concentration were monitored for stability by DLS at 5 mM $CaCl_2$ for 30 minutes. Immediately prior to the 30-minute measurement, the calcium concentration was adjusted to 7.5 mM with gentle mixing (to prevent local concentration inhomogeneities) with or without the addition of 0.5% (v:v) Tween 20.

3.2.7 Monitoring Digestion of ADGs by bvsPLA₂ and PLC via DLS

The scattering intensity of 5 mM ADGs in 5 mM $CaCl_2$, pH 5.4 at room temperature (RT) was observed in 10-min increments for 30 min to ensure colloidal stability. The ADGs were then diluted 10X in enzyme buffer pre-warmed to 37°C containing either 25 mM Tris·HCl, pH 7.4, 100 mM NaCl, 7.5 mM $CaCl_2$ and 10 µg/ml bvsPLA₂ or 50 mM Tris·HCl, pH 5.5, 10 µM $ZnCl_2$, 7.5 mM $CaCl_2$, 0.1% (w:v) BSA, and 1 µg/ml PLC. The scattering intensity continued to be monitored in 10-min intervals at 37°C as phospholipid hydrolysis occurred.

3.2.8 ADG Contact Activity in Human Plasma

Before addition to citrated PNP, 30 µM ADGs were digested with 100 ng/ml PLC from *C. perfringens* for 20 min in a buffer containing 5 mM $CaCl_2$, 10 µM $ZnCl_2$, 0.1% (w:v) BSA, and 50 mM Tris·HCl, pH 7.4 for 20 min at 37°C. After phospholipase digestion, 50 µl citrated PNP was recalcified with 50 µl of 25 mM $CaCl_2$, 5 mM imidazole, pH 7.4 and 50 µl sample was immediately added (after recalcification). Final concentrations of molecularly dissolved, long-chain polyP (polyP_{>600}) and ADGs were 10 µM. Turbidity was measured at 405 nm every minute for 60 min at room temperature using a Finstriments™ Microplate Reader (MTX Lab Systems,

Vienna, Virginia). The resulting sigmoidal absorbance traces were fitted to a Boltzmann sigmoidal function in OriginPro 8.6 (OriginLab Corporation, Northampton, MA). The time to clot was defined as the inflection point $x_0 \pm \text{S.E.}$ The percent reduction in the time to clot was normalized against the control (with no activator present).

3.2.9 Conventional Transmission Electron Microscopy

3.2.9.1 Sample Preparation

Briefly, 10 μl of the undiluted sample was pipetted onto a 300-mesh Holey, copper-on-carbon Formvar grid (Structure Probe Inc., West Chester, PA). After two minutes the liquid that did not evaporate was wicked away by placing the tip of a Kim wipe in close proximity to the liquid droplet. The grid was subsequently allowed to dry at ambient conditions for at least five minutes before examination in a JEM-1220 transmission electron microscope (JEOL Ltd., Tokyo, Japan).

3.2.9.2 High-Resolution Scanning Transmission Electron Microscopy (HR-STEM)

The biocompatible graphene sandwich containing the ADG was prepared by: (1) etching the copper layer away from a copper/graphene film to expose the graphene monolayer before transfer to the surface of DI H_2O ; (2) forming a thin liquid film containing the ADG sample on a standard TEM grid coated with monolayer graphene; and (3) exploiting the evanescent wave generated by total internal reflection to place the grid on top of the graphene monolayer to form the graphene sandwich.⁹¹ The EELS spectrum images of the ADGs and the bare particles are background subtracted. In **Figure 3.2B**, the P *L*-edge in the shell EELS spectrum (red) is taken from the shell of the EELS map of the ADG. The P *L*-edge in the core EELS spectrum (blue) is generated by first extracting the spectrum from the core region of the EELS map, which contains both the core and the shell signal, and then by subtracting the shell spectrum. In **Figure 3.2B**, the

O, P, and Ca line profiles are normalized to the maximum intensity, while the C line profile is normalized with P at the maximum intensity position.

10 mM bare granular polyP NPs and 5 mM ADGs were prepared in biocompatible graphene sandwiches using previously established methodology⁹¹ and transferred to JEOL JEM200CF STEM/TEM (JEOL Ltd., Tokyo, Japan) operated at 80 keV for imaging and EELS acquisition. HAADF and ABF images were taken simultaneously.

3.3 Results and Discussion

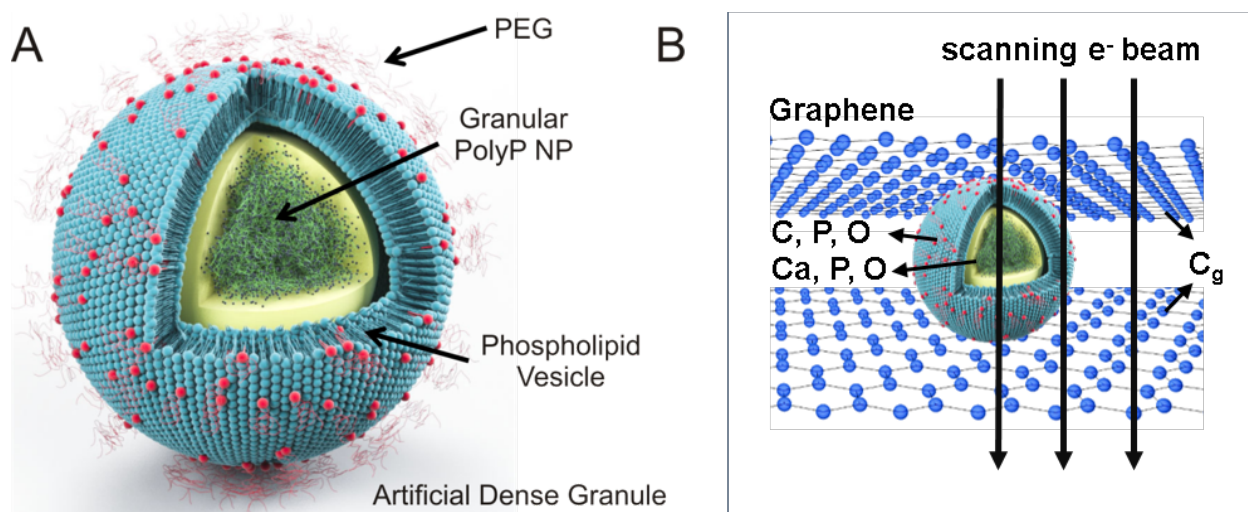


Figure 3.1. A: Schematic of ADG design and structure. ADGs are 150-nm granular polyP NPs encapsulated in 200-nm sterically stabilized, PEGylated liposomes. **B: Illustration of a biocompatible graphene sandwich trapping an ADG for high resolution imaging.** To prevent beam-induced morphology change and mass loss in the electron microscopy analysis, the ADG is directly sandwiched between two layers of free-standing graphene.

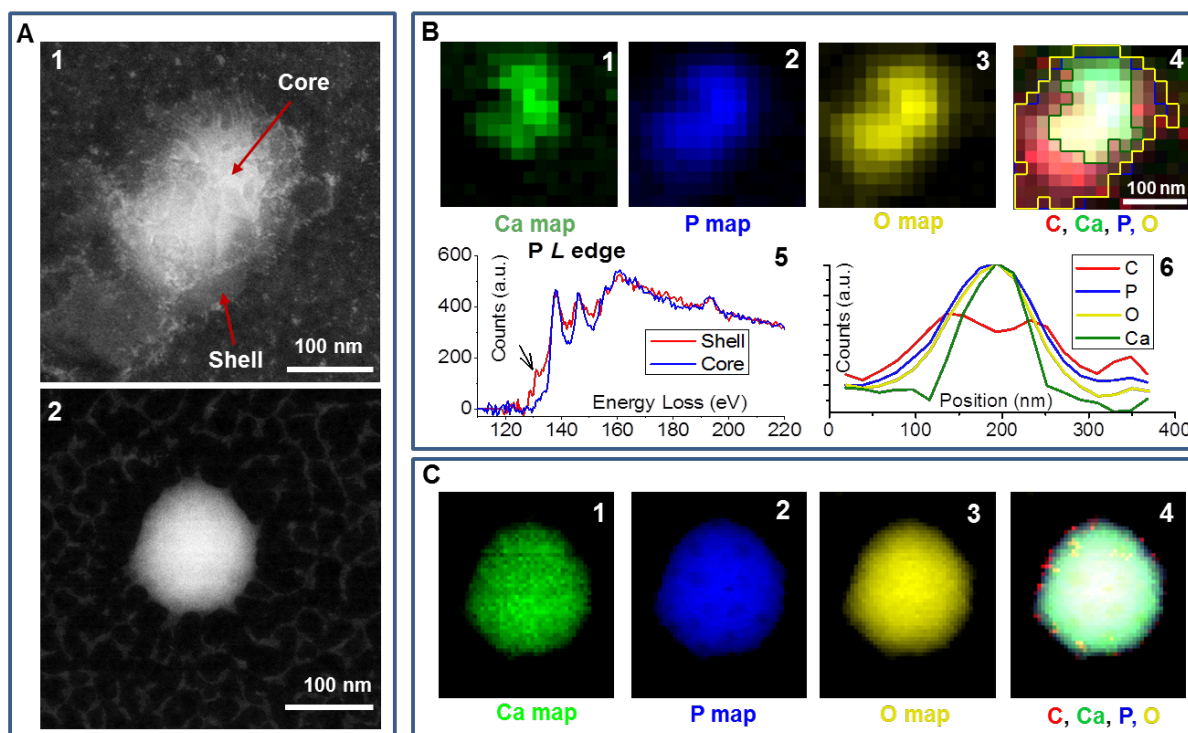


Figure 3.2. A: HAADF images of the ADG (1) and the bare polyP NP (2). B: Elemental and structural maps of the ADG. **B1-B4**: Individual Ca, P, O and composite (C, Ca, P, O) map extracted from EEL spectrum images with the graphene background subtracted. The color-coded outlines of the Ca, P and O distribution shown in **B1-B3** are superimposed in composite map **B4**. **B5**: Phosphorous *L*-edges extracted from the shell and core of the ADG shown in A. **B6**: Elemental line scan of the C, O, P and Ca map extracted from the graphene background-subtracted spectrum image of the ADG (**Figure B1-4**) from top left to lower right. C: Elemental maps of the bare particle. **C1-C4**: Individual Ca, P, and O maps as well as composite (C, Ca, P, O) map extracted from the background subtracted spectrum image.

A facile nanoprecipitation process was devised to encapsulate granular platelet-sized polyP into sterically stabilized liposomes rapidly on the benchtop, creating a nanoscale drug delivery platform modeled after the human body's intrinsic arsenal for controlling hemorrhage. The ADGs consist of a 150-nm granular polyP core surrounded by a 200-nm PEGylated liposome (**Figure 3.1A**), mimicking the size and structure of human platelet dense granules.⁴⁰

The nanostructure of the ADGs was subsequently examined by imaging and spectroscopic methods. Conventional transmission electron microscopy (TEM) and high-resolution scanning transmission electron microscopy (HR-STEM) were employed to show that the ADGs possess narrow size distribution and a defined core-shell architecture, with a homogeneously dense polyP granule serving as the core and a ring of lighter electron-density consisting of the phospholipid lamella (**Figure 3.2A & Figure 3.3**). Further, EELS was exploited to map the ADG's elemental components to prove unambiguously that the synthetic scheme yielded encapsulated polyP particles as intended.

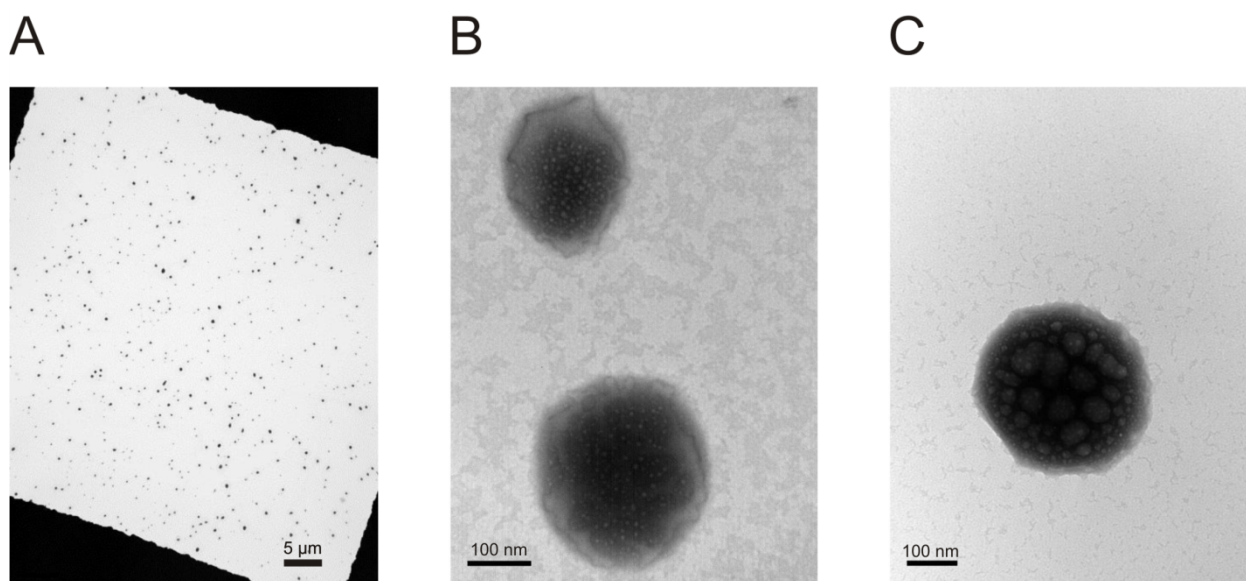


Figure 3.3. TEM of ADGs and Artificial Acidocalcisomes. A: Monodisperse ADG

population. Encapsulation of polyP NPs in sterically stabilized liposomes yields ADGs of low polydispersity without any aggregates visibly present. Scale bar: 5 μm . **B: Liposomally-encapsulated polyP NPs appear to have a core-shell architecture.** At higher magnification, one can notice a spherical spongelike core (the polyP precipitate) surrounded by a lighter shell, which presumably is the phospholipid envelope. The white spots are most likely hydrogen gas bubbles formed after prolonged electron beam exposure, ubiquitously observed among biological electron microscopy samples⁴ including isolated human platelet dense granules⁵. Scale bar: 100 nm. **C: Liposomally-encapsulated long-chain polyP forms Artificial Acidocalcisome.** Conventional TEM micrograph of polyP_{>1000} encapsulated in a sterically stabilized liposome following the same synthetic route as for platelet-sized polyP. Scale bar: 100 nm.

An inherent disadvantage of conventional TEM for structural characterization of biological or biomimetic nanomaterials is radiation damage from the electron beam,⁹⁰ limiting imaging resolution to length scales of nanometers and spectroscopy to angstroms.^{139, 140} Standard electron dose and dose rates directed at polyP bodies transform the granular structures into round sponges most likely due to electron beam-induced hydrogen gas bubbling and mass loss, and this therefore necessitates an alternative imaging and structural characterization tool for finer sample elucidation. To overcome these limitations, ADGs suspended in aqueous 5 mM CaCl₂ were directly sandwiched between two graphene layers, before transferal to the transmission electron microscope (JEOL JEM-ARM200CF) for high-resolution STEM and EELS analysis⁹¹ (**Figure 3.1B**). The presence of the graphene monolayers has been shown to substantially abrogate the deleterious electronic effects on the sample, minimizing covalent bond cleavage during electron

microscopy visualization of biological materials and biochemical reactions of experimental interest.¹⁴¹⁻¹⁴⁵ As a comparison, bare granular polyP NPs prepared in graphene sandwiches are spherical particles of uniform electron density, with the characteristic white spots, observed by Docampo and Ruiz⁴⁰ using conventional TEM, being absent (**Figure 3.2A**). The polyP granules are approximately 150-200 nm in diameter, in very good agreement with DLS measurements (cf. **Figure 3.4**). In contrast to the bare particles, the ADGs exhibit a clear core-shell nanoarchitecture characteristic of a polyP NP encapsulated in a liposome. A high angle annular dark-field (HAADF) image of an ADG reveals a dense, 150-nm core surrounded by an irregularly-shaped 25-nm thick shell of decreased electron density (**Figure 3.2A**). These length scales are in good agreement with light scattering data, as the granular polyP NP was measured to have an initial hydrodynamic diameter of ~160 nm and the liposomes were formed via extrusion through a polycarbonate membrane with 200-nm pores.

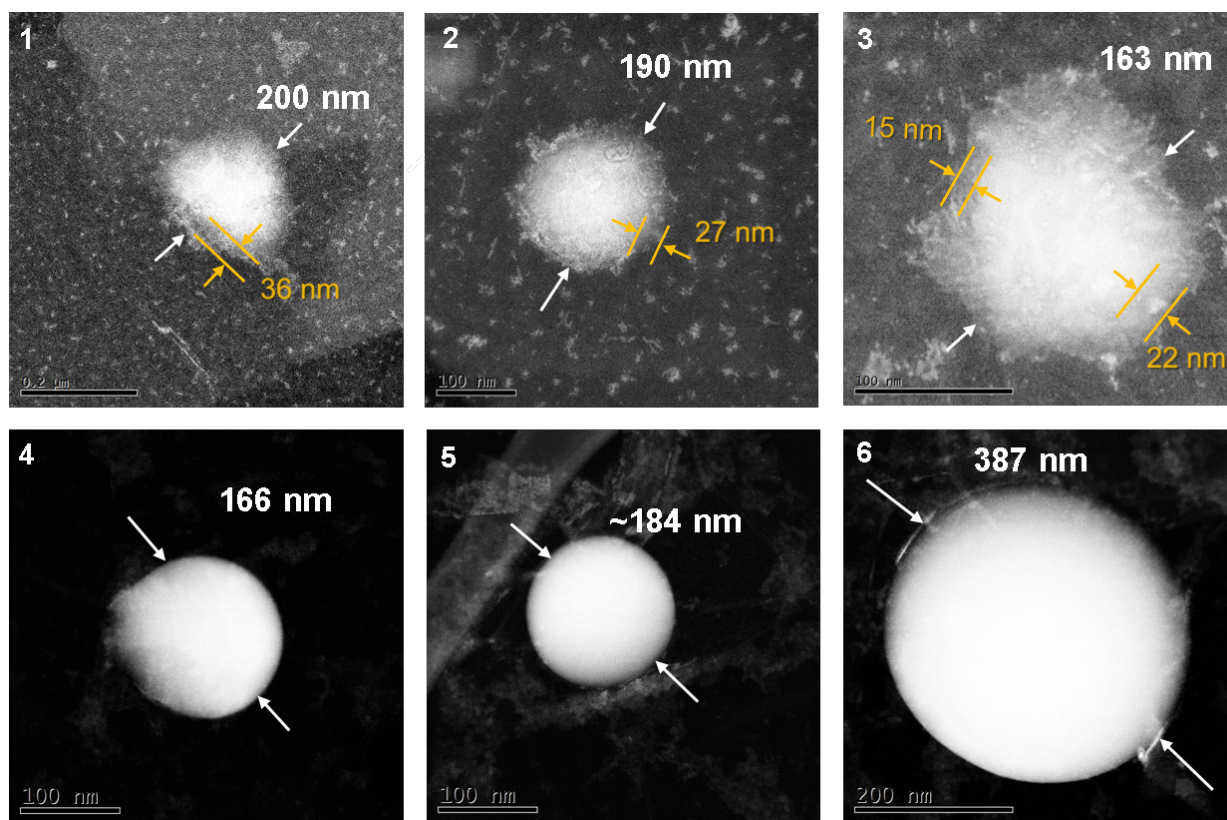


Figure 3.4. HAADF images of the ADGs (1-3), as well as the bare particles (4-6) protected by the graphene sandwich approach. Compared to the images of ADGs taken using conventional TEM (**Supporting Figure S1**), the morphology of the graphene-protected ADGs are better preserved, and thus reveal more structural details. Comparison of the ADGs (1-3) and the bare particle images (4-6) clearly show a morphology difference between the bare polyP granules and the liposomally encapsulated ADGs. While the bare polyP granule mostly manifests a uniform sphere structure, the ADGs clearly reveal a core-shell architecture.

To the best of our knowledge, this is the first time that EELS has been used to probe the elemental constituents of polyP NPs and their liposomally encapsulated counterparts, ADGs.

Figure 3.2B shows the elemental distribution of Ca, P and O within the ADG particle. The compositional map reveals that the shell consists of C, O, and P, but not Ca, suggesting the

presence of a phospholipid envelope. The carbon signal in the shell stems most likely from the PEG brushes and the hydrocarbon tails, glycerol backbone, and headgroup carbons of the phospholipid lamella (cf. **Figure 3.4**). The dense core exhibits a homogeneous distribution of Ca, P and O, demonstrating that the granular polyP NPs were successfully encapsulated by the phospholipid envelope. As a control group, **Figure 3.2C** shows the elemental distribution of Ca, P, and O of the bare particle. These elemental maps match well with the acquired HAADF image, and show a uniform distribution of Ca, P and O in the bare particle, consistent with the elemental composition of granular polyP NPs. The pixel-size in **Figure 3.2B** is larger than in **Figure 3.2C** to minimize the effects of electron-dose induced changes to the shell. In order to rule out the possibility that in the ADG, the O and P signals in the core region shown in **Figure 3.2B** are only coming from the phospholipid envelope, which also contains O and P, we perform elemental line scans of the C, O, P and Ca to show the distribution of these elements, shown in **Figure 3.2B**. Elemental line scans of C and Ca indicates the presence of a Ca core encapsulated by a ~25 nm thick C shell. The shape of the C and Ca signal is consistent with the typical core-shell structure. Unlike the “saddle” shape of C, which indicates the absence of C in the core, the Gaussian shape of the O and P signals indicates that these two elements are present in both the core and the shell. Furthermore, analysis of the P *L*-edges is used to compare the local P bonding between the core and the shell. Both spectra show a near-edge fine-structure typical for P_xO_y ,¹⁴⁶ while the P spectrum from the shell shows an additional pre-peak, indicating a loss in P-O bonding. These EELS data are consistent with our expectation of the P bonding structure in the granular polyP core as well as the liposome shell.

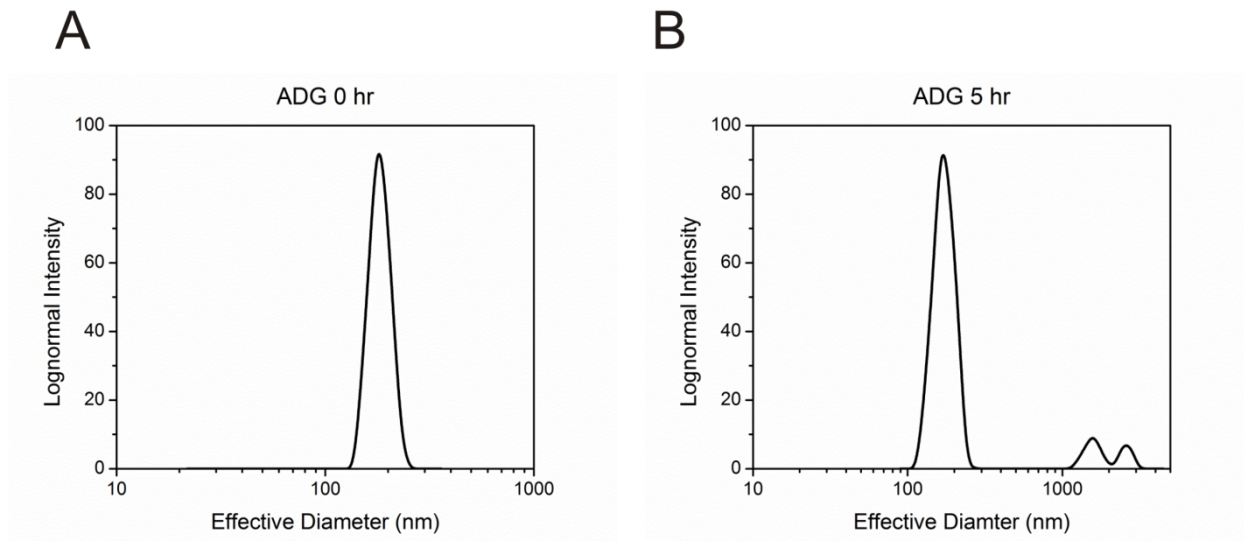


Figure 3.5. Intensity-weighted, lognormal particle size distribution of ADGs by DLS prepared for HR-STEM. A: ADG particle size distribution immediately after encapsulation. ADGs are monodisperse and approximately 180 nm in diameter. B: ADG particle size at 5 h after 30 s of gentle vortexing. The ADG intensity-weighted particle size distribution has a major peak at 180 nm and a minor peak above 1 micron. Very little irreversible aggregation has occurred.

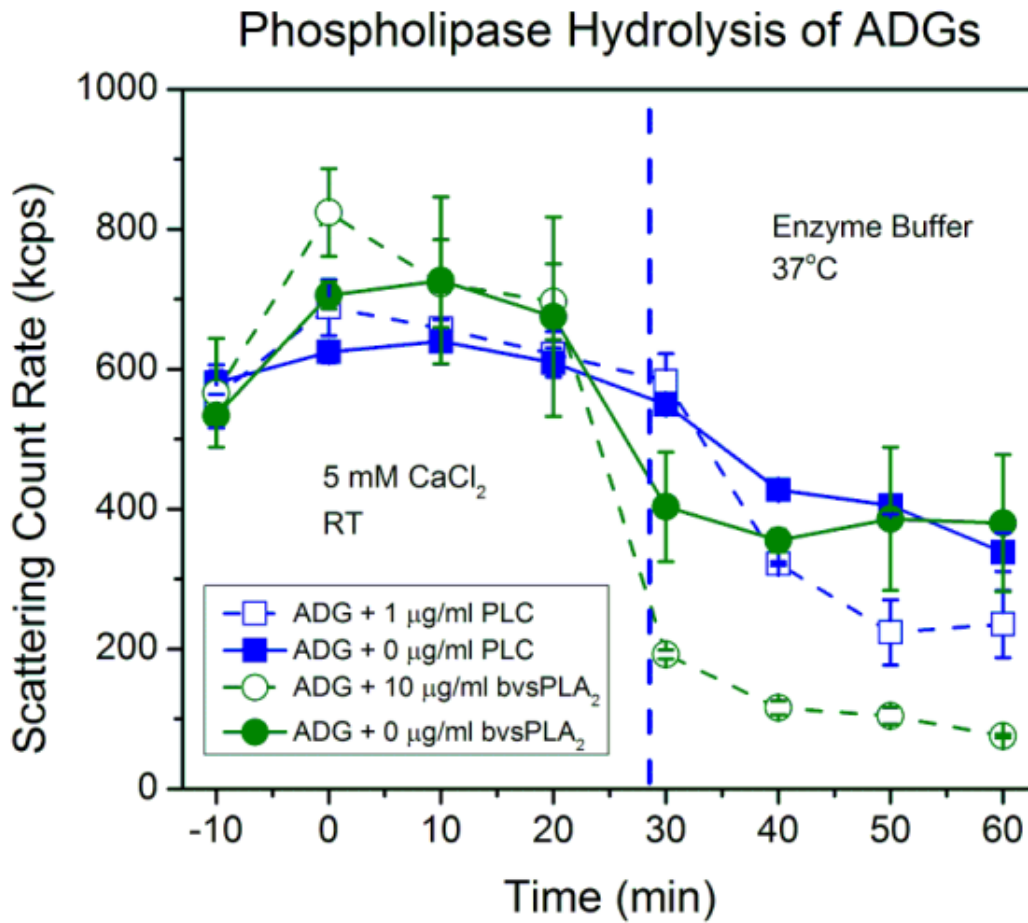


Figure 3.6. Scattering intensity of ADGs after phospholipase digestion. ADGs were prepared in 5 mM CaCl₂ at room temperature (RT) and monitored for stability for 30 min before transferal to an enzyme buffer at 37°C containing either 10 µg/mL sPLA₂ from bee venom (bvsPLA₂) or 1 µg/mL PLC from *C. perfringens*. The scattering count rate drops significantly for both 10 µg/mL bvsPLA₂ and 1 µg/mL PLC ADG digestions, implying that the phospholipases are inducing hydrolysis of the lipid envelope, leading to degradation and agglomeration of ADGs and precipitation of the polyP NP cargo.

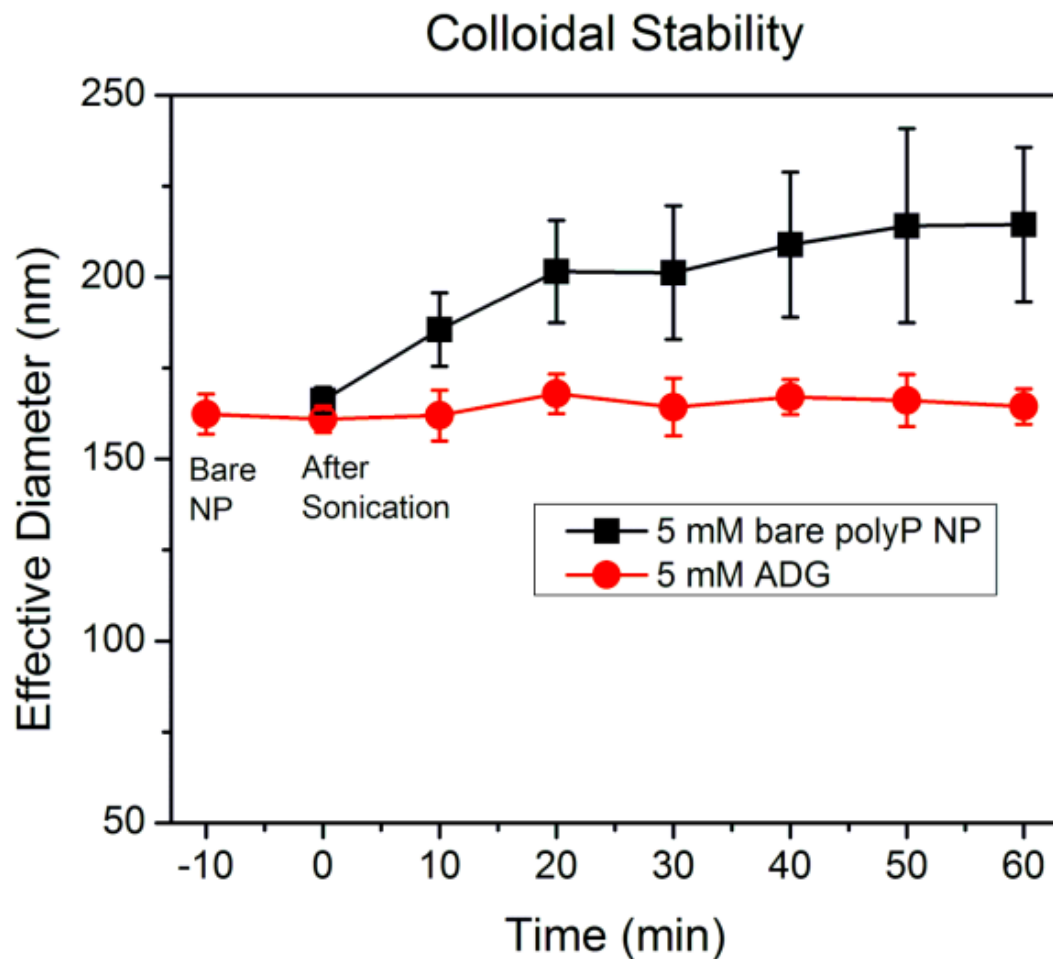


Figure 3.7 Stability of ADGs in suspension. The average effective diameter was determined for the bare polyP NP (immediately before adding liposome, $t = -10$ min), immediately after sonication ($t = 0$ min), and every ten minutes thereafter until 1 h had elapsed. The ADGs do not appreciably change in size over the duration of the experiment. The bare polyP NPs, on the other hand, prepared at the same supersaturation ratio, grow in a power-law manner to a mean effective diameter of approximately 220 nm in 1 h.

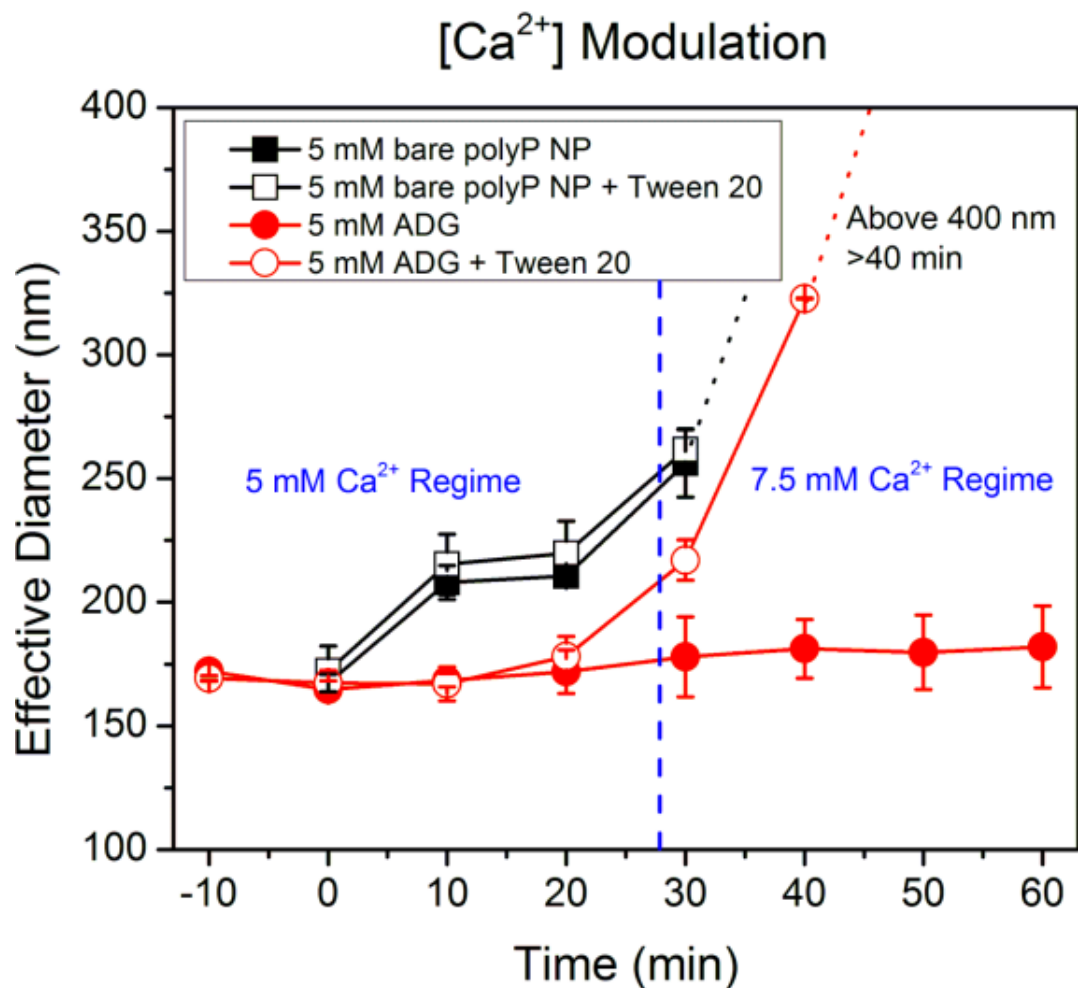


Figure 3.8 Verification of the ADG encapsulation efficiency by measuring ADG diameter shifts after exposure to detergent and changes in calcium concentration. Liposome solubilization by the non-ionic detergent Tween 20, in conjunction with an increase in the calcium concentration, was exploited to judge the ADG encapsulation efficiency semi-quantitatively. In the absence of Tween 20 and an increase in calcium concentration to 7.5 mM at $t=30\text{ min}$, there is no statistically significant perturbation in the ADG effective diameter (solid red dots). However, increasing the calcium concentration after dissolution of the lipid envelope

by detergent exposure allows for the polyP NPs to be exposed to the higher amount of calcium, resulting in an increased effective diameter (hollow red dots).

The stability of the ADGs was subsequently investigated for 1 h at room temperature in the same solution in which they were prepared (5 mM CaCl_2 , pH 5.4) utilizing DLS, measured in 10-min intervals (**Figure 3.7**). The initial effective diameter of the bare polyP granules is approximately 160 nm with a PDI ~ 0.1 ($t = -10 \text{ min}$ in **Figure 3.7**), in agreement with our previous report.¹³⁵ After addition of a stoichiometric excess of sterically stabilized liposomes and 10 min of bath sonication, encapsulated polyP granules are monodisperse with a PDI ~ 0.2 , (**Figure 3.5**), with an effective diameter only marginally bigger than their unencapsulated counterparts ($t = 0 \text{ min}$ in **Figure 3.7**). Further DLS measurements reveal that the diameter remains unchanged ca. 165 nm after 60 min has elapsed, whereas bare polyP NPs (black symbols and line in **Figure 3.7**) in the same solution environment manifest power-law type growth kinetics. At the time of nanoprecipitation the bare polyP granules are approximately 160 nm, ripening to $\sim 220 \text{ nm}$ in 1 h. The equivalent power-law growth phenomenon is clearly absent with the ADGs (red symbols and line in **Figure 3.7**). The particle diameter of the ADGs as determined by electron microscopy is comparable qualitatively to the hydrodynamic diameter measured by dynamic light scattering, which strongly suggests that the encapsulated particles observed in HR-STEM are stable in suspension for at least an hour, a time scale sufficient to potentially mitigate bleeding after a severe hemorrhagic event.

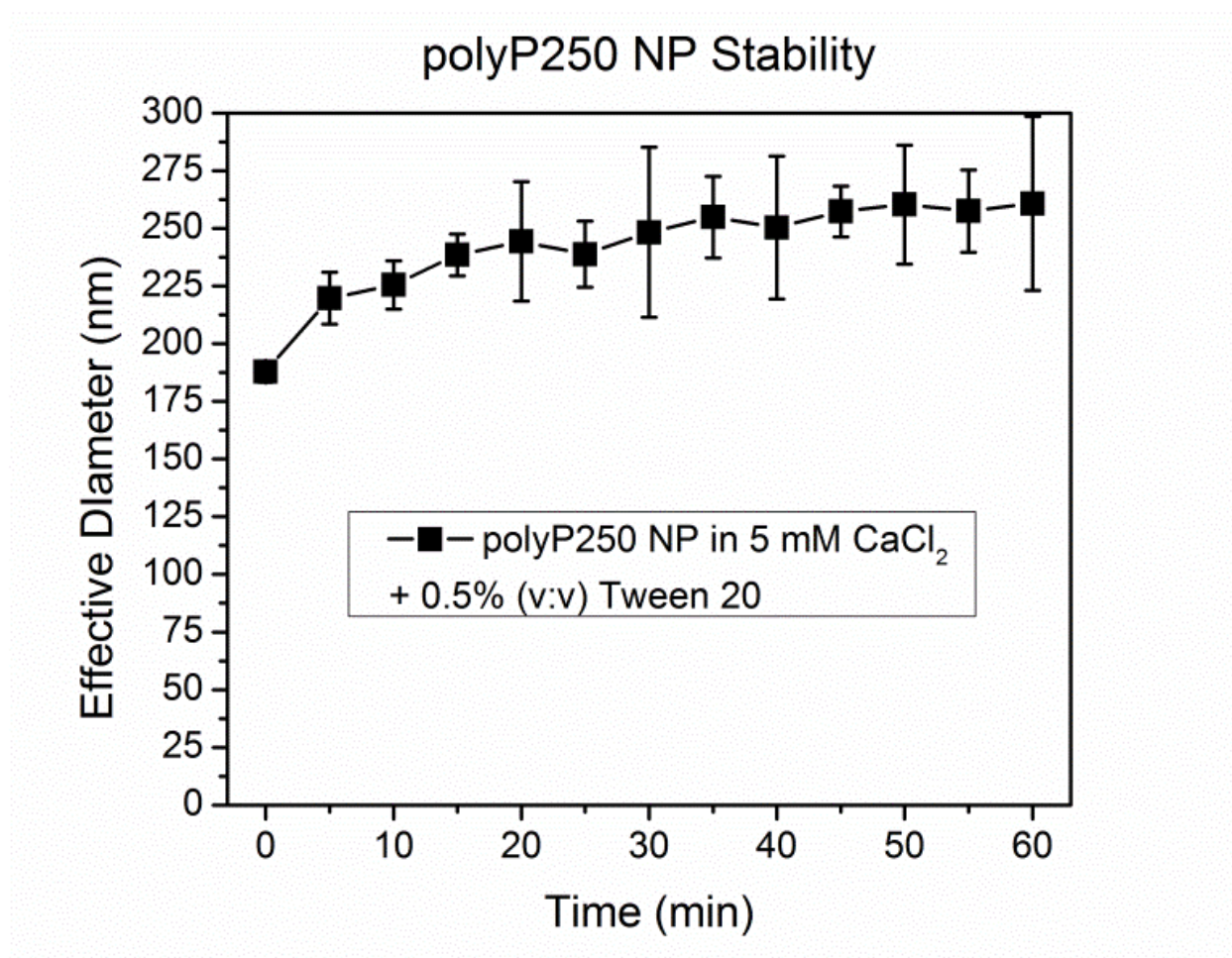


Figure 3.9. Colloidal stability of granular polyP NPs in the presence of non-ionic detergent. Intermediate chain length polyP250 was nanoprecipitated in 5 mM CaCl₂ + 0.5% (v:v) Tween 20 and the particle growth was monitored by DLS every 5 min until 1 h had elapsed. The presence of the surface-active agent appears to exert no influence on the ability of polyP to assemble into granular nanoparticles, nor diminish its colloidal stability, as polyP nanoprecipitated in 5 mM CaCl₂ alone also manifests equivalent power-law growth kinetics and comparable particle diameters.

ADG encapsulation efficiency was investigated by modulating the calcium concentration, since the presence of calcium controls the thermodynamic equilibrium of granular polyP NP self-assembly.¹³⁵ Changes in the calcium concentration would have nearly immediate effects on the polyP NP effective diameter, as the polyP NP size is solely determined by the calcium concentration over an extensive range of polyP supersaturation values.¹³⁵ 5 mM ADGs were synthesized in 5 mM CaCl₂, pH 5.4, and monitored by DLS every 10 min. Once 30 min had elapsed the calcium concentration was increased to 7.5 mM and an excess of a non-ionic detergent, Tween 20, (which would not affect polyP nanoprecipitation in a measurable way, cf. **Figure 3.9**) was added to solubilize the vesicular envelope and expose the polyP cargo to the higher calcium environment (**Figure 3.8**). Upon addition of 0.5% (v:v) Tween 20 and increasing the calcium concentration to 7.5 mM, the average particle size rapidly increases above 200 nm (red line with open circles in **Figure 3.8**). 10 min after detergent solubilization, the particle population is no longer unimodal (data not shown), with a Gaussian-averaged effective diameter greater than 300 nm. Visible sedimentation of agglomerated granular polyP occurs 20 min after adding detergent, with the effective diameter bigger than the micron length scale and the scattering count rate tending to 0. In the absence of detergent, an increase in calcium concentration, in contrast, causes only a negligible change in size, with the average effective diameter centered around 165-180 nm (red line with solid circles in **Figure 3.8**), comparable to the instance with no modulation in the calcium concentration (red line with solid circles in **Figure 3.8**). Bare polyP NPs subjected to the same experimental scheme show typical power-law growth before calcium concentration increase and subsequently rapidly precipitate into micron-sized particles after 10 min independent of the presence of detergent. These results suggest that the particle encapsulation efficiency is close to the theoretically maximum value.

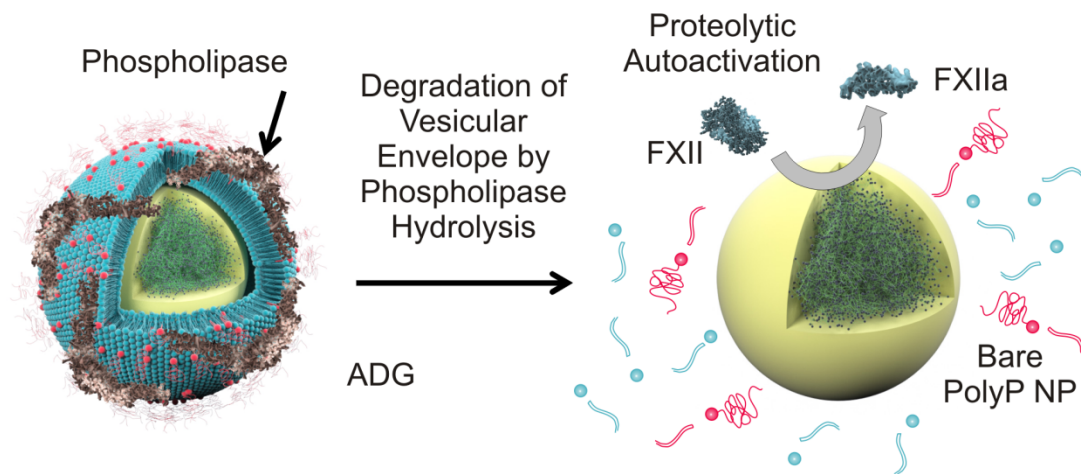


Figure 3.10. Illustration of phospholipase-induced degradation of the lipid envelope.

Secretory phospholipases such as human sPLA₂ encountered at locally high concentrations near sites of trauma and inflammation, as well as intracellular isoforms like PLC, involved in platelet degranulation, are envisioned to degrade the liposome vesicle, exposing the granular polyP NP to induce FXII autoactivation.

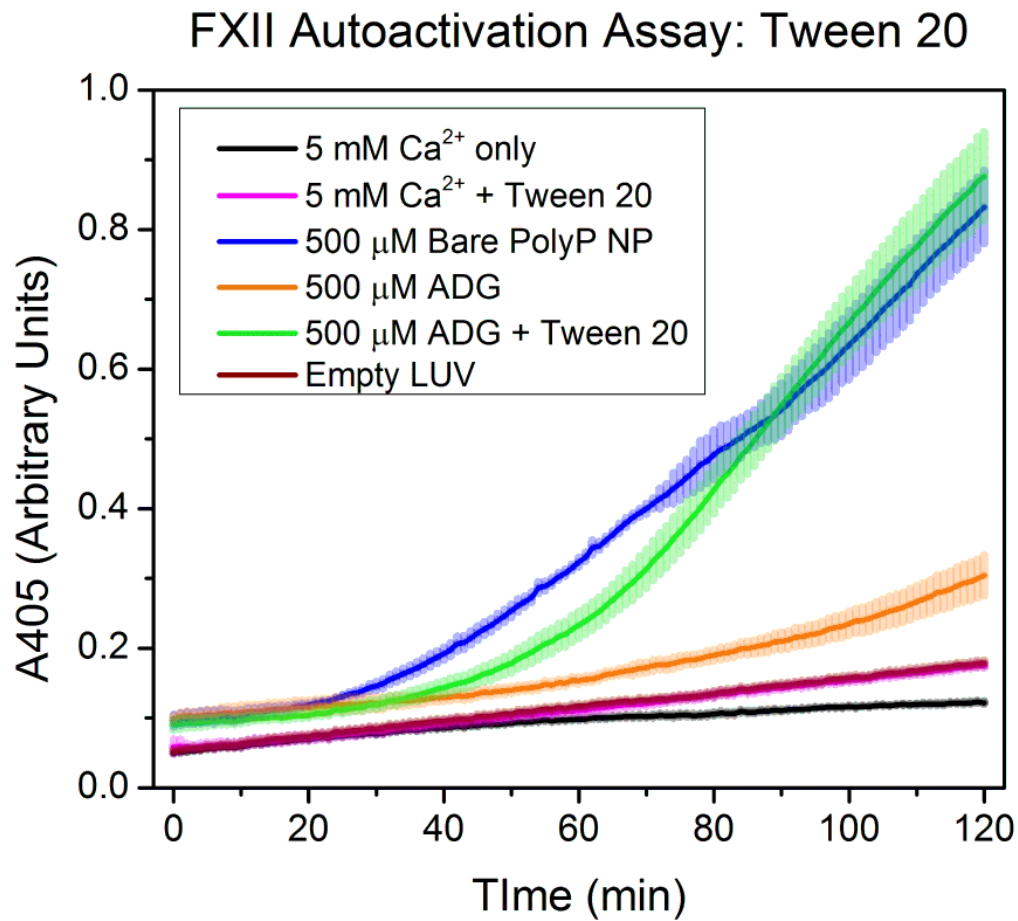


Figure 3.11. Autoactivation of FXII zymogen via detergent-triggered solubilization of ADG vesicular envelope. ADGs initiate autoactivation of FXII after addition of 0.5% (v:v) Tween 20, similar to the bare polyP NPs (as a positive control). In contrast, ADGs without detergent treatment yield no significant conversion of FXII to FXIIa. As a negative control empty liposomes at the same concentration elicit no FXII autoactivation.

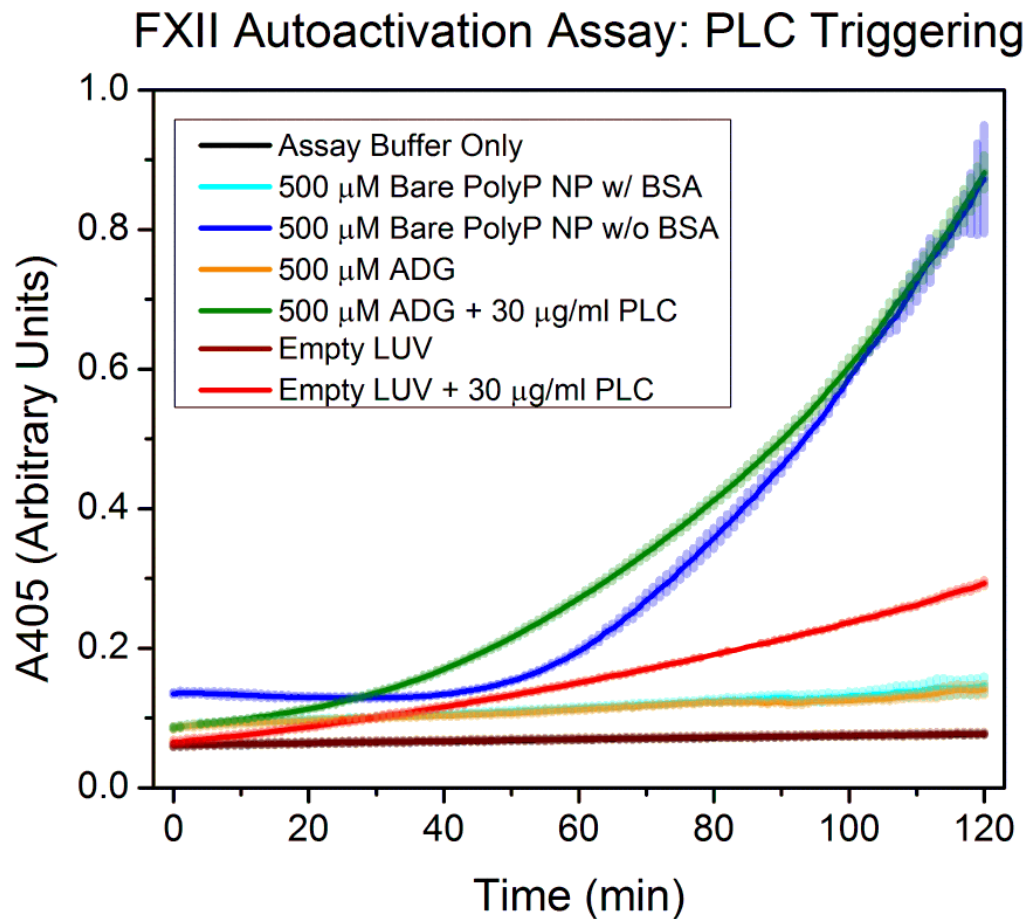


Figure 3.12. FXII autoactivation after ADG preincubation with PLC. ADGs were incubated with 30 μ g/ml PLC (from *C. perfringens*) at 37°C for 20 min before initiation of FXII autoactivation in a buffer containing BSA to ensure optimal phospholipase digestion. Bare polyP NPs without BSA were included as a positive control. ADGs preincubated with PLC manifest a similar rate of absorbance increase to both bare polyP NPs and ADGs digested with Tween 20. ADGs without PLC do not measurably promote FXII autoactivation at the concentration tested. Empty liposomes digested with PLC show some absorbance increase, which is likely a result of vesicle aggregation after phospholipid hydrolysis.

Not only do the ADGs structurally resemble human platelet dense granules, they also manifest potentially promising procoagulant effects *in vitro* like their biological counterparts when triggering agents are used to disassemble the phospholipid envelope and expose the procoagulant polyP cargo. Inspired by the platelet degranulation process that occurs *in vivo*, we present a paradigm through which hydrolytic enzymes present in human platelets or secreted into the circulation after hemorrhage can be exploited to induce clotting factor activity on a time scale sufficient to cease bleeding.

The targeted delivery of polyP relies on the presence of phospholipases (e.g. PLC and sPLA₂), which occur at much higher concentrations at local bleeding sites (at the scale of $\mu\text{g/ml}$) compared to global baseline physiological levels (at the scale of ng/ml) to quickly degrade phospholipid vesicles. Immediately after traumatic hemorrhage, a concatenation of carefully orchestrated biochemical events must occur near the wound site, with platelets serving as the principal actors in establishing primary hemostasis.¹⁴⁷ Platelets adjacent to the trauma site stick to the damaged endothelium creating a temporary “plug,” recruit other platelets via secreted small molecule messengers, and initiate the coagulation cascade by supporting activation of circulating clotting factors.¹⁴⁸⁻¹⁵⁰ PLC plays a major role in platelet activation, and is central to the platelet degranulation process^{151, 152}— the exocytosis of dense and α granules into the vasculature, ensuring that high local concentrations of polyP are established in platelet-rich thrombi. PLC is an intracellular lipase which hydrolyzes phospholipids at the 3 position,¹⁵¹ leading to mobilization of intracellular calcium stores and activation of G protein-coupled secondary messenger systems with diverse physiological consequences extending beyond hemostasis and inflammation.¹⁵³ Although PLC in human platelets exclusively hydrolyzes phosphoinositides,¹⁵⁴ numerous other PLC isoforms exist in nature that do not discriminate

between phospholipids. Many bacterial toxins referred to as “lecithinases” possess robust PLC activity for phosphatidylcholines and phosphatidylethanolamines.^{155, 156}

An additional strategy employs secreted phospholipases at sites of inflammation, e.g. around tumors and sites of vascular injury, to promote hydrolysis of the vesicular envelope. It has been clinically documented that in human patients with a constellation of inflammatory diseases, such as rheumatism and atherosclerosis, that the serum concentration of secretory phospholipase A₂ (sPLA₂) can reach 10-30 ng/mL.¹⁵⁷ Local plasma concentrations of sPLA₂ in the boundary layer directly adjacent to sites of trauma can be 100- to 1000-fold higher, approaching 10 µg/mL. Moreover, several studies have shown that degradation of phospholipid vesicles by phospholipase hydrolysis could be an order faster when conjugated to PEG chains.¹⁵⁸ The likely mechanism is that PEG chains cause extrusion of the phospholipid to the exterior of the bilayer, promoting more rapid and facile phospholipase adsorption at the interface.¹⁵⁹ Therefore, PEGylated phospholipid vesicles, as with our design of encapsulating polyP NPs, not only offer steric stabilization and immunoprotection, but also a means for controlling and targeting drug release upon phospholipid degradation at the sites where phospholipases are overexpressed.

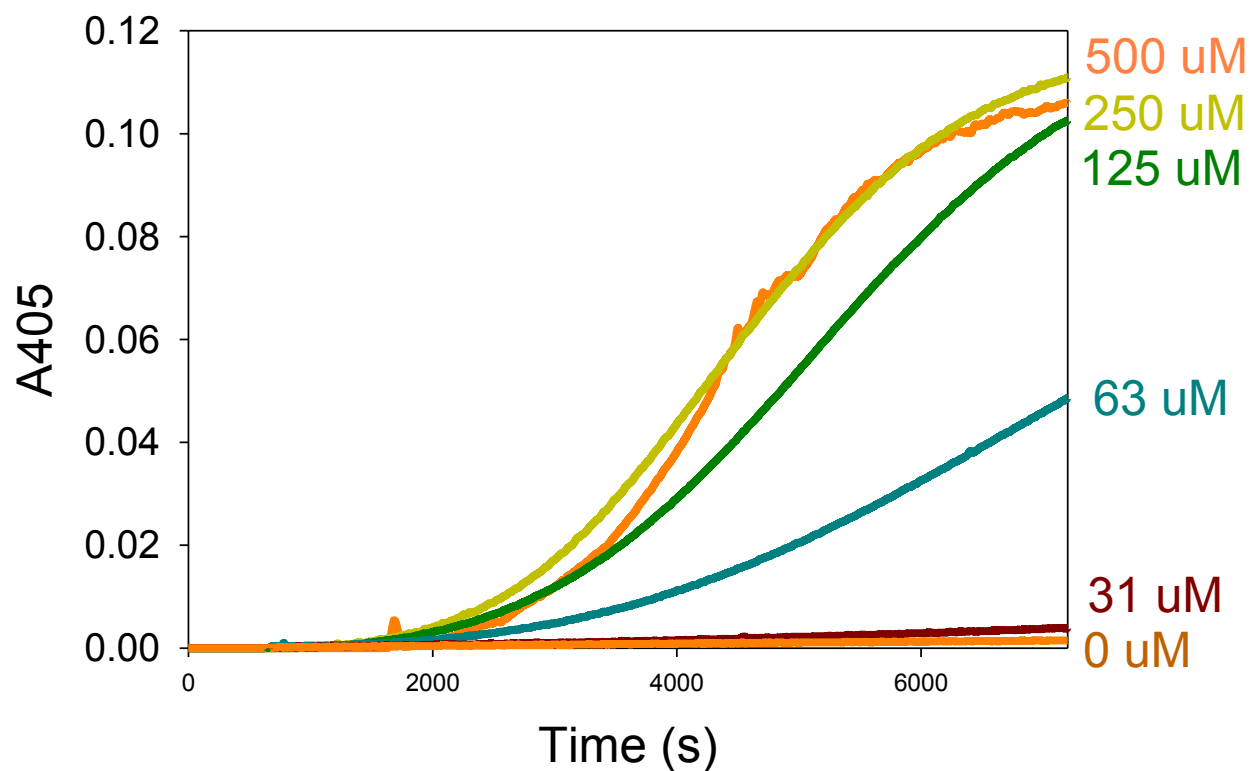


Figure 3.13. FXII autoactivity assay of bare polyP NPs. The initiation of FXII autoactivation elicited by bare granular polyP NPs manifests typical saturable, concentration-dependent kinetic behavior, with 250-500 μM being the most potent concentration range.

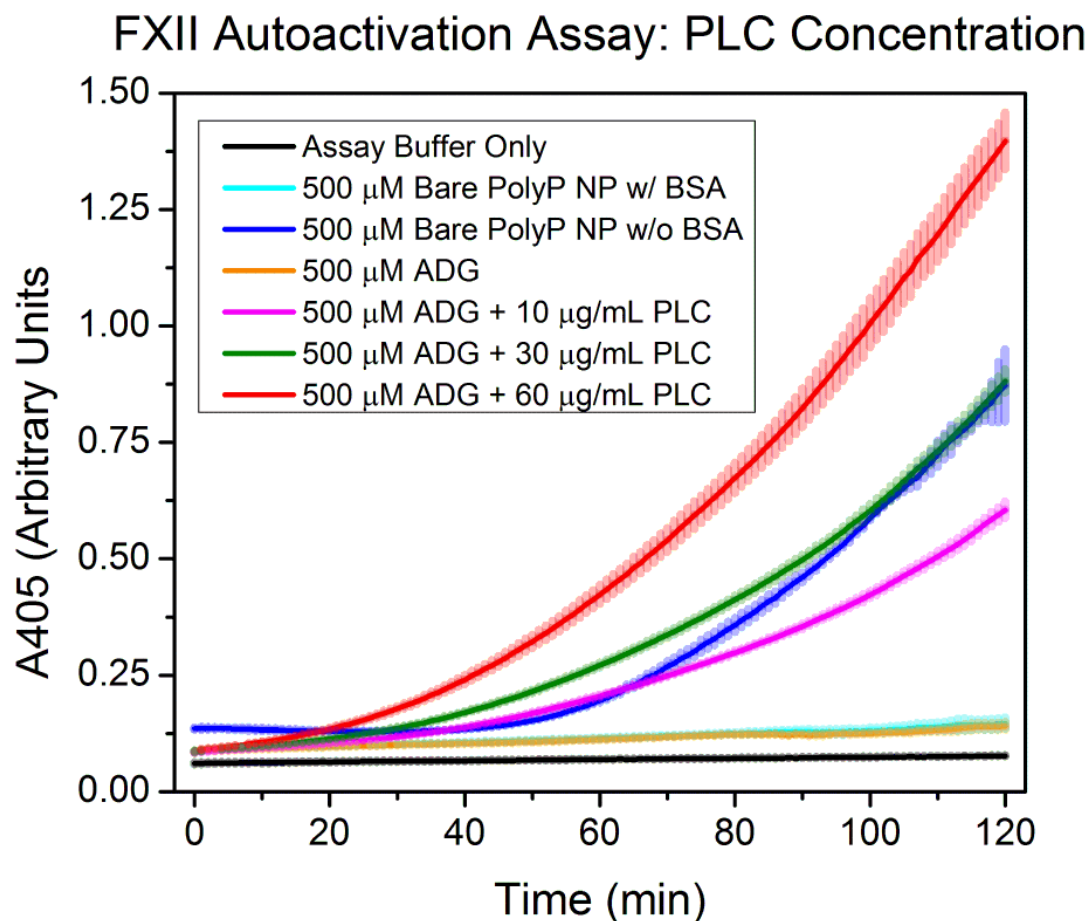


Figure 3.14: PLC concentration dependence of ADG-induced FXII autoactivity. A: ADGs pre-incubated with increasing amounts of PLC. 500 μ M ADGs were digested in the presence of 10, 30, or 60 μ g/mL PLC from *C. perfringens* at 37°C for 20 min prior to initiation of FXII zymogen autoactivation in the presence of chromogenic substrate. There is a clear correlation between increasing concentration of phospholipase and FXII autoactivity.

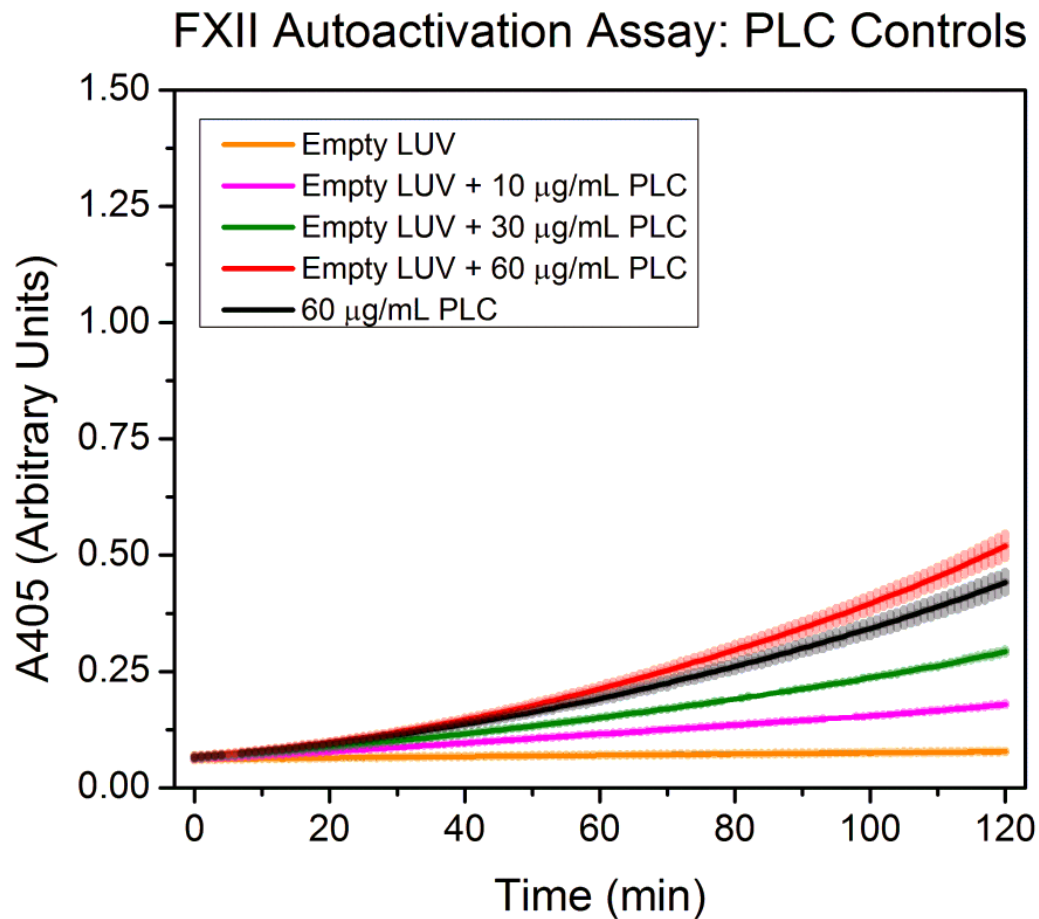


Figure 3.15 : Empty sterically stabilized liposomes in the presence of phospholipase. Empty vesicles with the equivalent concentrations of enzyme also display a notable absorbance increase. However, the mechanisms underlying this increase in absorbance likely stem from aggregation of vesicles or interaction of phospholipid degradation products with FXII zymogen or S-2032 substrate, as negatively charged phospholipids are known activators of the contact pathway of blood coagulation. 30 $\mu\text{g/mL}$ PLC appears to be the optimal triggering dose for comparable activity to the bare polyP NP and minimal activation from the vesicular hydrolytic products.

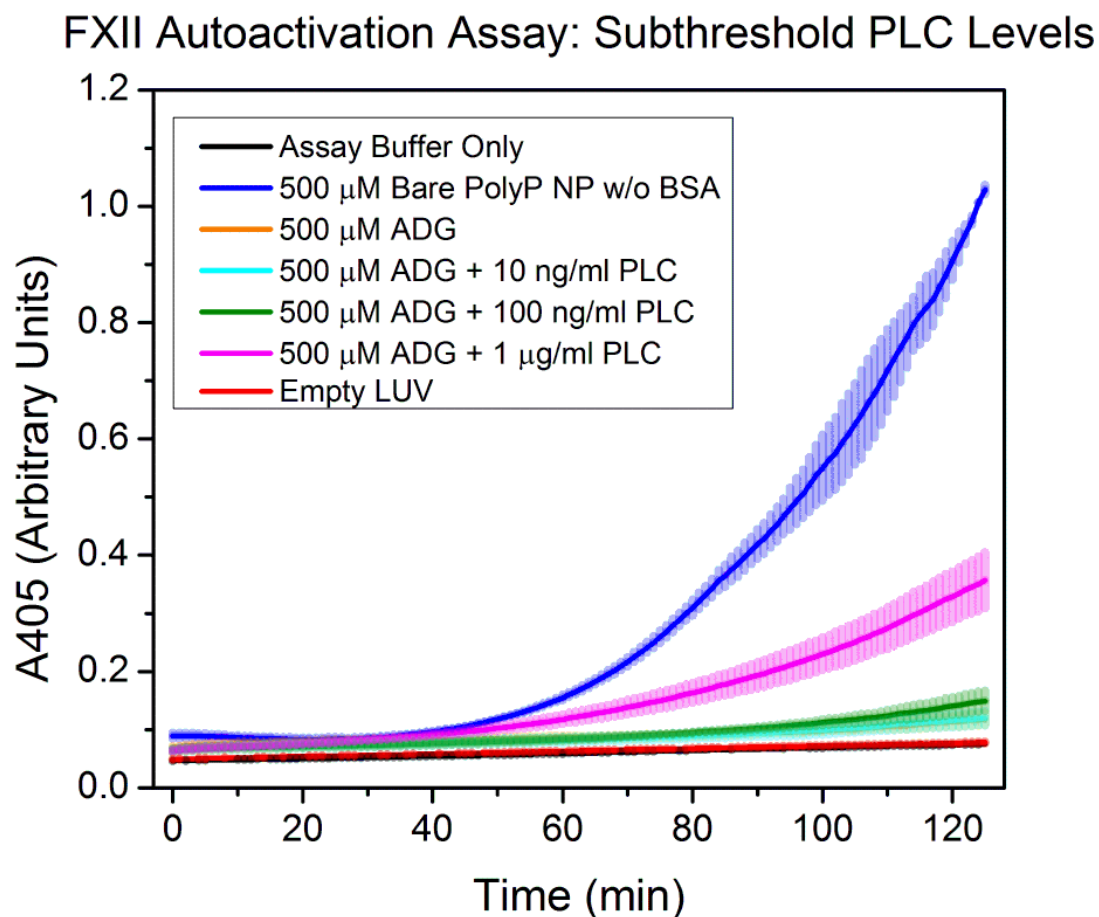


Figure 3.16. Subthreshold phospholipase concentrations do not trigger ADG-induced FXII zymogen conversion. Physiological PLC concentrations below 1 μ g/ml are below threshold to uncoat the ADG lipid envelope, implying that only pathologically extreme phospholipase concentrations encountered in the vicinity of hemorrhagic sites would induce ADG envelope hydrolysis and polyP NP unloading.

The phenomenon of ADG liposomal envelope digestion by model phospholipases was explored by DLS to estimate time scales of hydrolysis and protein concentrations necessary for polyP cargo release to suitably modulate clotting factor activity. The colloidal stability of ADGs

was surveyed in 5 mM CaCl₂, pH 5.4 at RT for 30 min before dilution into an enzymatic assay buffer at 37°C. Upon transfer to the enzymatic buffers tailored for optimal PLC and sPLA₂ activity, respectively, the scattering intensity marginally drops, likely due to changes in liposome phase behavior and fluidity due to the low melting temperature of L- α -phosphatidylcholine, the major constituent in the sterically stabilized liposomes (**Figure 3.6**). Moreover, the calcium concentration for both buffers is 7.5 mM in order to gauge polyP release after hydrolysis. In the absence of enzyme, the size of the ADGs does not change significantly, suggesting that the majority of the granular polyP NPs are completely encapsulated. After addition of 1 μ g/mL PLC or 10 μ g/mL sPLA₂ at 30 minutes, however, the scattering intensities drop significantly. This suggests that the phospholipases have begun to hydrolyze the liposomal barrier surrounding the polyP NP, leading to polyP NP precipitation in the more calcium-enriched environment, decreasing the total number of colloidal particles due to sedimentation. Further investigation reveals that 30 μ g/ml PLC is an ideal concentration for *in vitro* autoactivation of FXII (**Figure 3.14-3.16**).

The ability of ADGs to autoactivate isolated FXII zymogen after detergent-induced solubilization was first assessed as a proof-of-principle demonstrating that the polyP NP cargo retains its procoagulant functionality. Corroborating Engel *et al.*'s results that platelet-sized polyP robustly supports zymogen conversion,¹³⁸ we show under similar experimental conditions that 500 μ M ADGs are able to promote autoactivation of FXII after detergent solubilization by 0.5% (v:v) Tween 20, whereas ADGs not treated with detergent are largely inert, exhibiting minimal FXII autoactivity (**Figure 3.11**). Empty sterically stabilized liposomes are also unable to initiate conversion of FXII to FXIIa, suggesting that promotion of autoactivation stems from release of the granular polyP NPs. FXII autoactivity of the bare granular polyP NPs is

concentration-dependent, and manifests saturating kinetic behavior with maximal autoactivation occurring at 500 μ M monoP for BKGP70, the same polyP used in this study (see **Figure 3.13** for concentration dependence). **Figure 3.12** shows that ADGs preincubated in a 0.1% (w:v) BSA suspension with PLC for optimal phospholipase activity for 20 min before addition of zymogen initiate conversion of FXII in a manner consistent with ADGs subjected to detergent treatment with Tween 20. ADGs preincubated in the same buffer without PLC are largely “contact inactive”. Likewise, empty sterically stabilized liposomes are unable to support autoactivation of FXII zymogen. The absorbance intensity of empty sterically stabilized liposomes preincubated with the equivalent concentration of PLC does increase slightly during the duration of the experiment; however, this rise is likely due to vesicle aggregation or zymogen activation stemming from interaction with negatively charged degradation products.

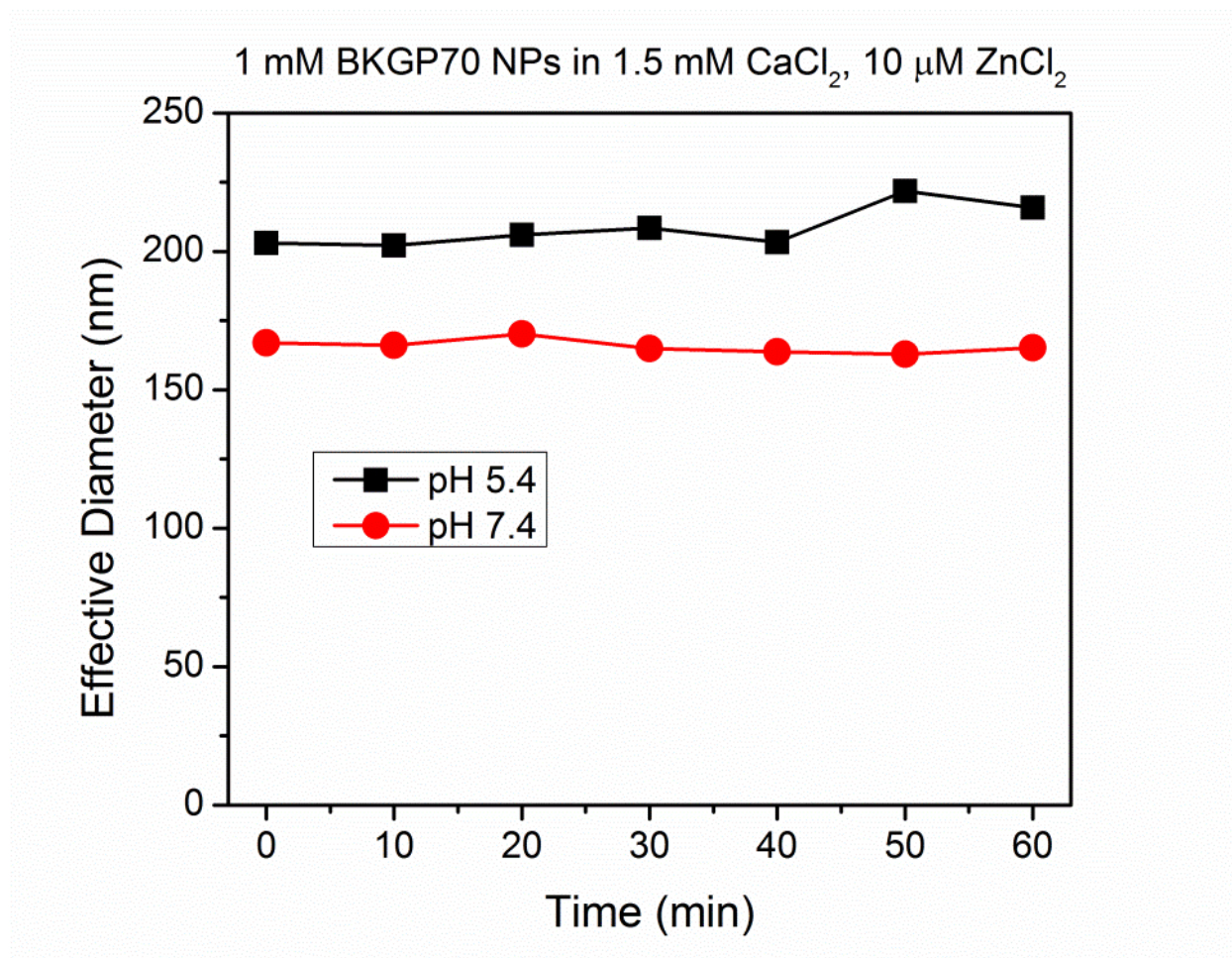


Figure 3.17. Mean particle diameter of platelet-sized polyP NPs precipitated in 1.5 mM CaCl_2 , 10 μM ZnCl_2 , conditions mimicking the ionic concentrations for the FXII autoactivation assay, at nearly neutral and slightly acidic pH. The granular polyP NPs are approximately 160-200 nm and do not exhibit the same power-law growth behavior characteristic of polyP NPs in aqueous media containing only CaCl_2 .

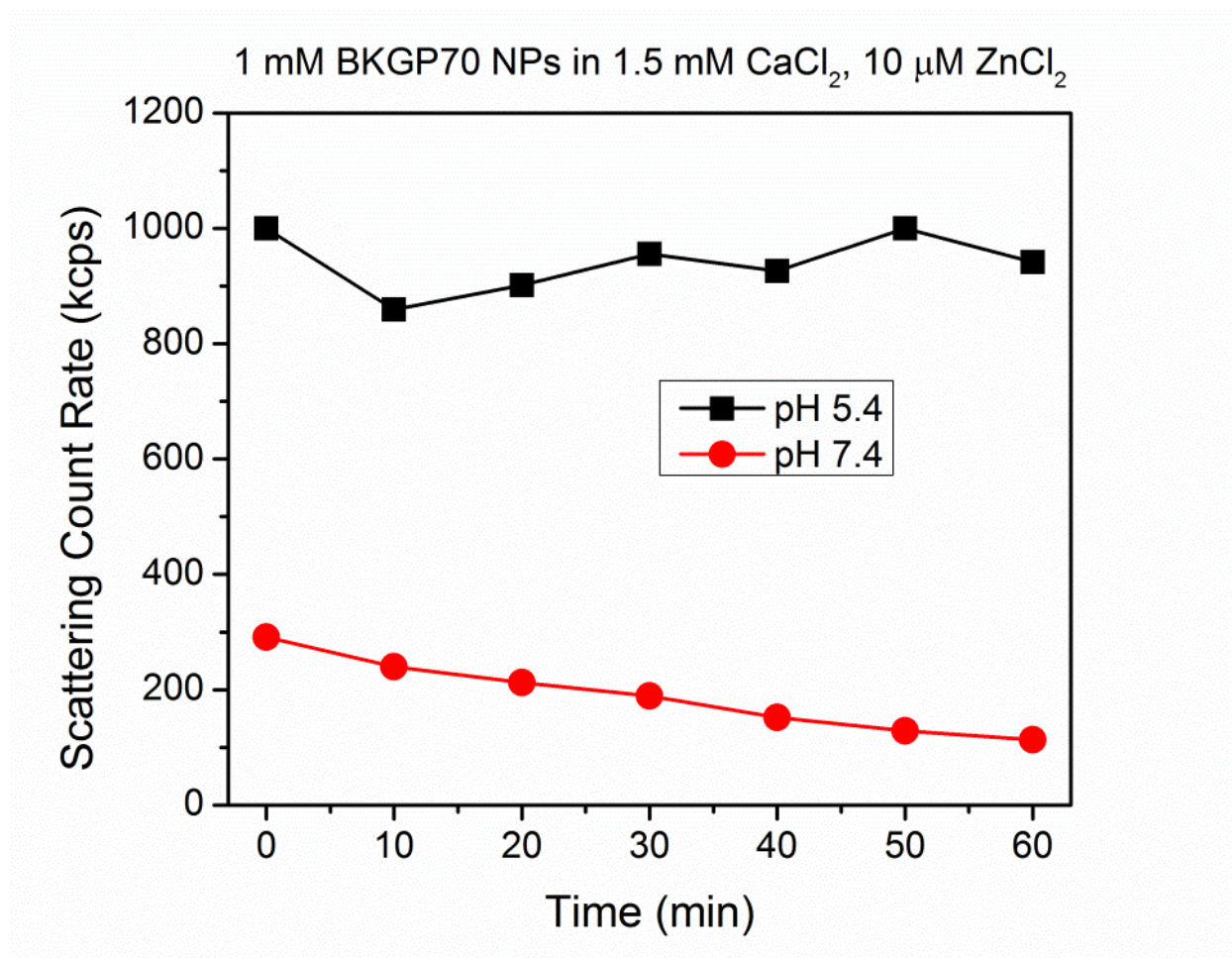


Figure 3.18. Scattering intensity of Ca²⁺/Zn²⁺-polyP NPs at physiologic and dense-granular pH environments. The scattering count rate decreases precipitously at pH 7.4, but is remarkably stable at pH 5.4, equivalent to the mildly acid lumen of human platelet dense granules.

Interestingly, 500 μM bare polyP NPs in the presence of 0.1% (w:v) BSA evince no contact activity over the 120 min assay, whereas bare polyP NPs without BSA elicit robust FXII autoactivation within 1 h (**Figure 3.12**). BSA is an established divalent metal chelator, with low dissociation constants for Ca²⁺, Zn²⁺ and Cu²⁺.^{107, 109} Moreover, zinc cations greatly accelerate FXII autoactivation, and hence significantly reduce the autoactivation doubling time.^{160, 161} The

presence of millimolar amounts of divalent metals like Ca^{2+} and Zn^{2+} ensures that the predominant polyP species is either an NP or polyP-metal complex (see **Figures 3.17-3.18** for zinc's *nanoprecipitative* effects). It is well established that foreign contact activators manifest as either negatively charged colloids or granules like kaolin⁵⁰ or as polymer-metal complexes, e.g. ellagic acid coordinated with copper.¹⁶² The fact that BSA effectively lowers the free ionic concentration of these precipitative divalent metal cations and completely abrogates polyP NP contact activity in this simplified *in vitro* model of the contact pathway of blood clotting suggests that divalent metal ion complexation to the polymer may be required for polyP to elicit FXII zymogen autoactivation. Additionally, recent work by Ursula Jakob and colleagues at the University of Michigan provides compelling evidence that polyP is a nonspecific protein binder, facilitating protein folding in a fashion comparable to conventional protein chaperones.³⁶ Surface plasmon resonance measurements have identified numerous blood proteins that bind to polyP, including thrombin.¹⁶³ We have also observed by DLS that bare polyP NPs may complex with BSA via a calcium-mediated process.¹³⁵ However, enzymatically triggered hydrolysis of ADGs by PLC even in the presence of BSA still yields significant proteolytic autoactivation (**Figure 3.12**). Although there is a high concentration of serum albumin in human plasma, polyP still manages to function as a very potent procoagulant agent, implying that the inhibitory effect of serum albumin cannot be too strong. Nonetheless, the precise mechanism by which BSA and polyP interact demands further investigation. Taken together, these data suggest that PLC hydrolysis of the lipid envelope is occurring, quickly exposing a negatively charged surface to autoactivate the FXII zymogen, and, further, that the sterically stabilized liposome shields the granular polyP NP from interacting with FXII and other proteins like BSA over a duration of at least two hours.

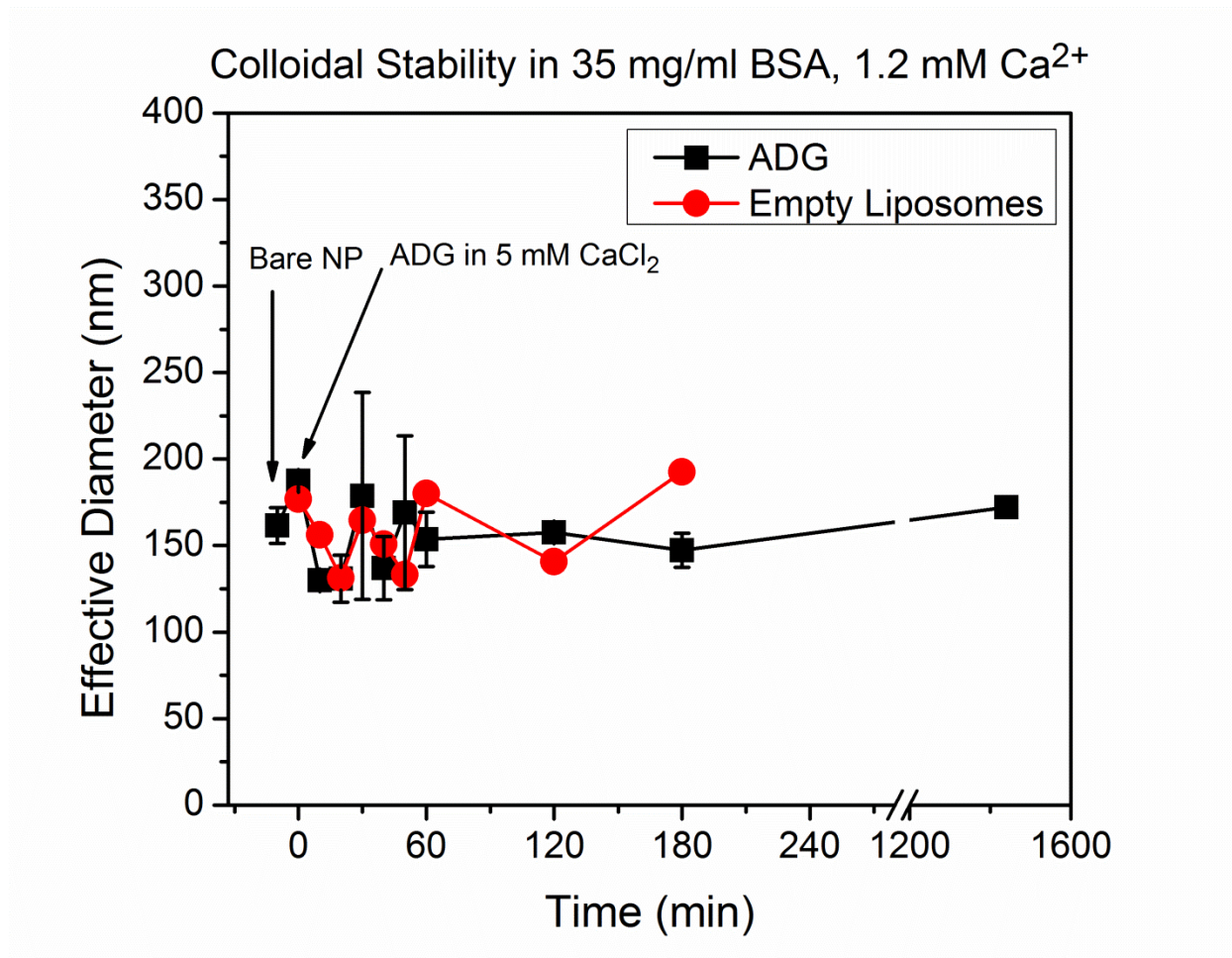


Figure 3.19. Colloidal stability of ADGs and empty liposomes in 35 mg/ml BSA, 1.2 mM Ca^{2+} , approximating the solvent environment of human blood plasma. A: Effective diameter of ADGs and empty PEGylated liposomes in BSA suspension over a 24-h period.

The hydrodynamic diameter of ADGs and empty liposomes were measured in 35 mg/ml BSA suspensions with 1.2 mM Ca^{2+} by DLS for 24 h. The particle diameter was determined by calculating the intensity-weighted average of the largest peak in the MSD summary (see below in **Figure 3.xx**). The particle diameter does not change significantly over the trial period.

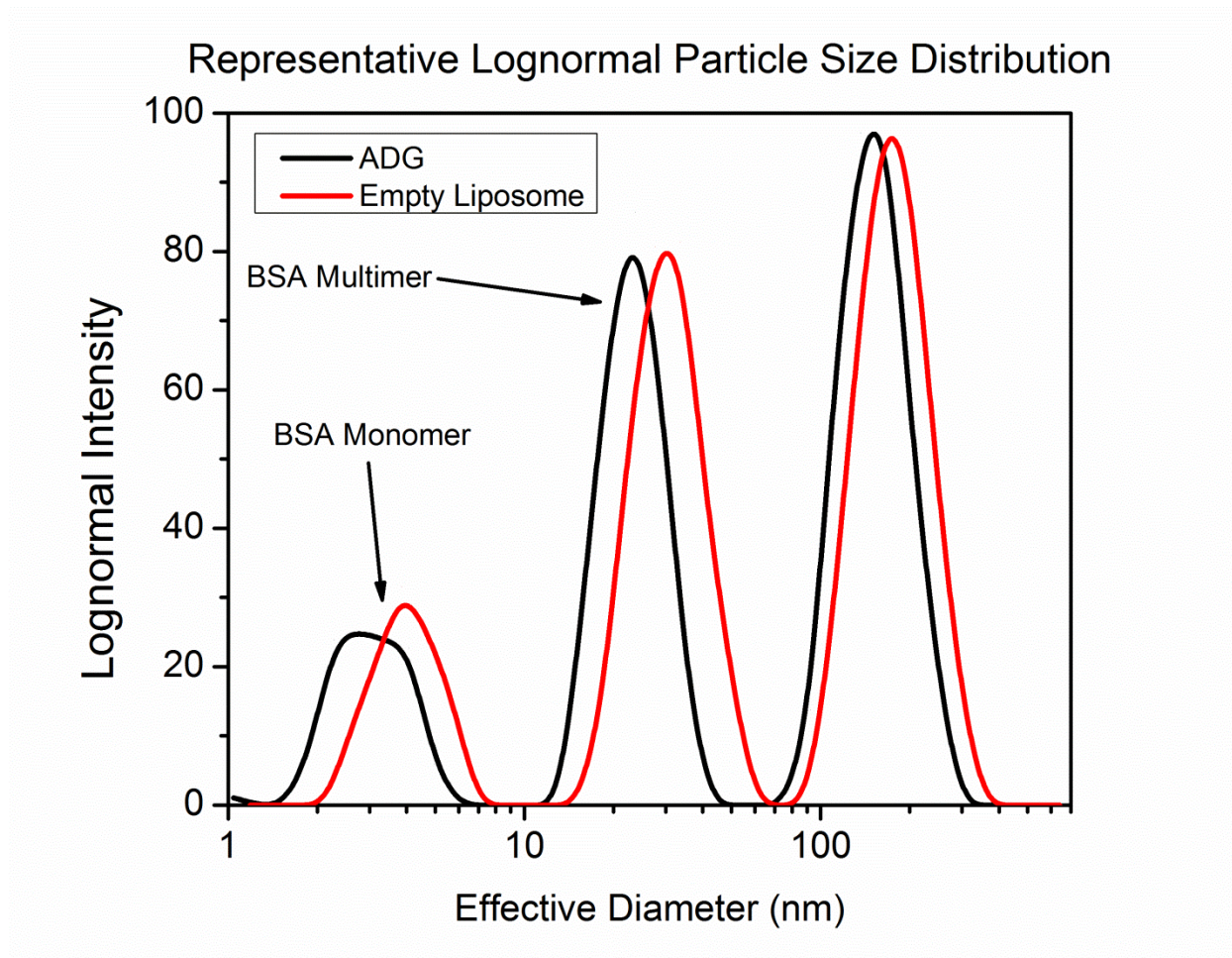


Figure 3.20 Trimodal particle size distributions of ADGs and empty liposomes 40 min after addition to the BSA suspension. The particle populations for both ADGs and empty liposomes in BSA manifest as three distinct peaks: the first, centered around 3 nm, is likely the protein monomer; the second, with a hydrodynamic diameter of approximately 21 nm, appears to be a BSA aggregate; and third, the largest peak is most likely the liposomal sample, i.e. the ADG or empty PEGylated vesicle. As the calcium cation concentration is 1.2 mM, any unencapsulated polyP is favored to form 50-nm diameter granular particles, which are clearly absent in the particle size distribution above. Taken together, these data suggest that ADGs are sufficiently

colloidally stable to properly interrogate their procoagulant effects in recalcified human plasma.

Similar studies with bare polyP NPs in BSA/Ca²⁺ have already been performed.¹³⁵

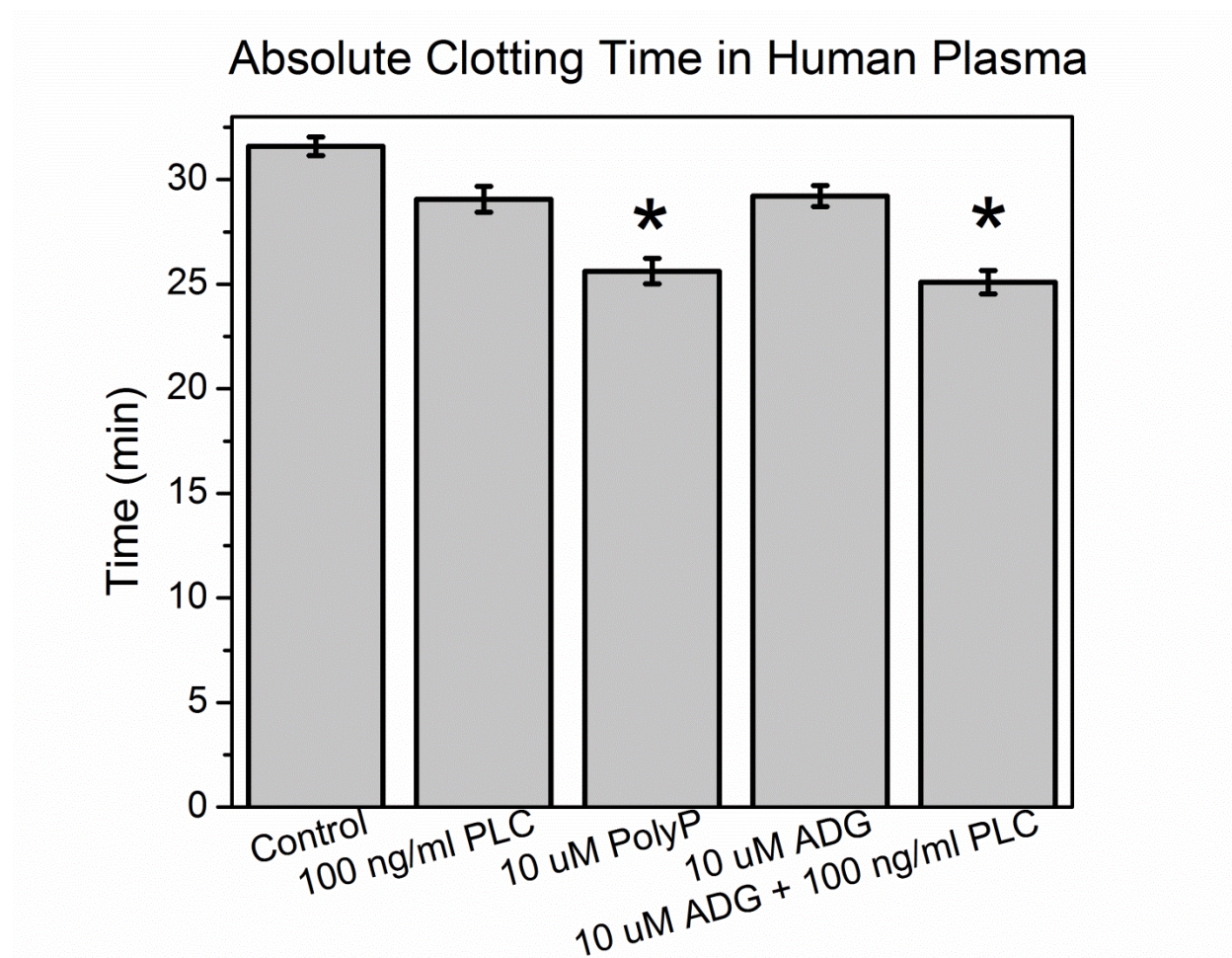


Figure 3.21. Contact activity of ADGs in human plasma. A: Absolute clotting time in human plasma. 10 μ M ADGs + 100 ng/ml PLC are comparably procoagulant to 10 μ M molecularly dissolved, long-chain polyP. 10 μ M ADGs without trigger and 100 ng/ml PLC alone marginally reduce the time to clot compared to the control (with no activator present). Absolute clotting time is given by the fitted inflection point of a Boltzmann sigmoidal growth function \pm

S.E. of the averaged absorbance traces of each sample group (n=11). * represents $p<0.05$ for a two-sided t test compared to control (without activator).

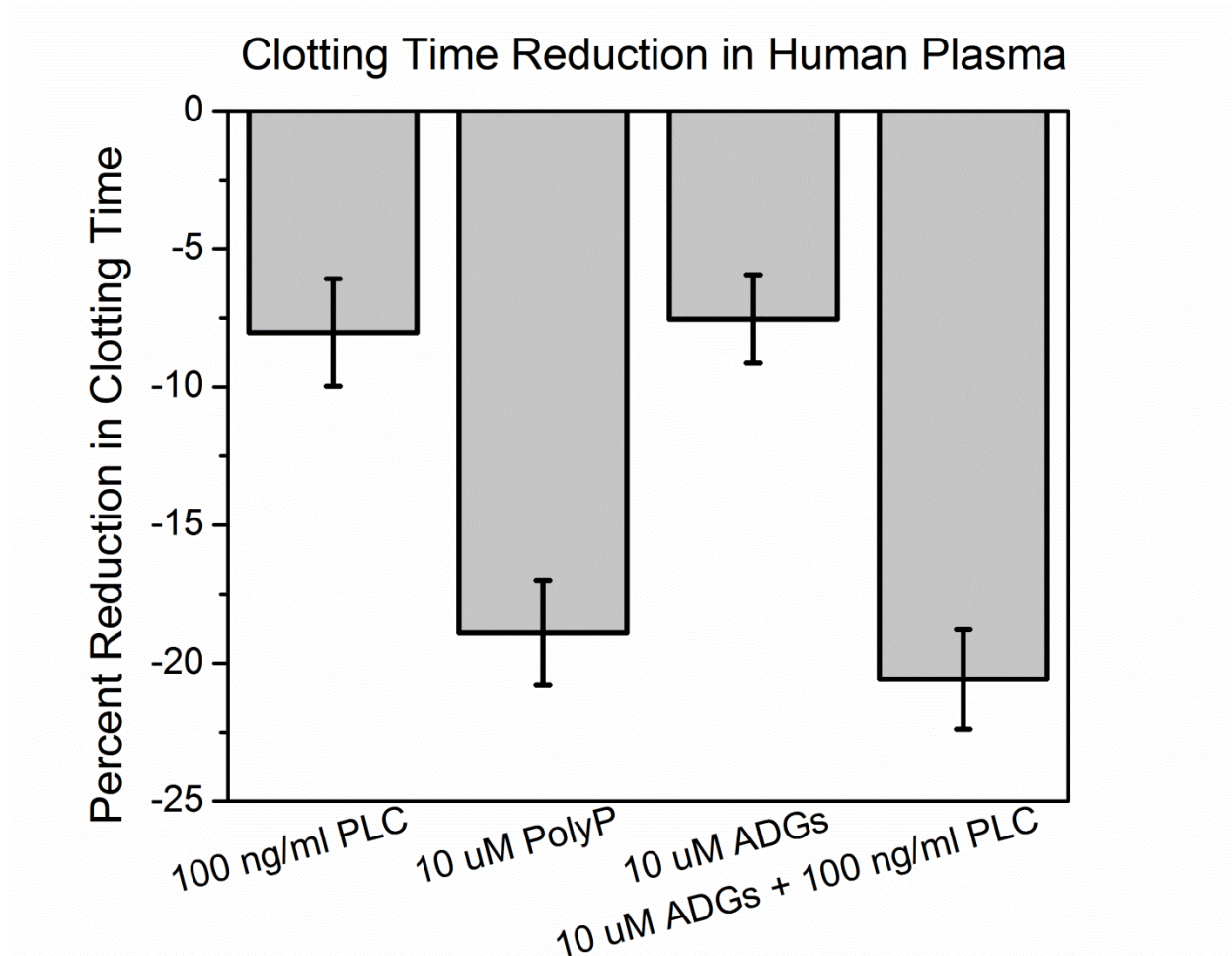


Figure 3.22. Clotting times given as percent reduction from the control.

In addition to assessing the ability of ADGs to catalyze the conversion of FXII zymogen to FXIIa in isolation, the particles' contact activity was determined in pooled normal plasma (PNP) by measuring changes in turbidity upon coagulation. ADGs were preincubated for 20 min with 100 ng/mL PLC from *C. perfringens* before initiation of clotting. **Figure 3.21-3.22** shows that 10 μ M ADGs + 100 ng/ml PLC reduce the time to clot equivalently compared to 10 μ M

molecularly dissolved, long-chain polyP, with 21% and 19% diminutions compared to control, respectively. 10 μ M ADGs and 100 ng/ml PLC alone both clot slightly more rapidly than control (with no activator present). The fact that ADGs minimally reduce the clotting time suggests that either a small fraction of the polyP remains unencapsulated, or that some polyP can be transported across the relatively fluid ADG bilayer, of which 95 mol% is the low T_m L- α -PC, when it is diluted into PNP. Given that PLC also reduces the time to coagulation compared to control implies that the phospholipase possesses marginal intrinsic contact activity at the concentration tested. It is also noteworthy that molecularly dissolved, long-chain polyP is not as robust a contact activator as previous reports in the literature demonstrate^{33, 135}; however, the assay protocol was suitably modified to gauge the ADG procoagulant activity, accounting for the divergent behavior. Altogether, PLC is able to digest the ADG lipid envelope, allowing the polyP granule inside to initiate the contact pathway of blood coagulation.

3.4 Conclusion

We present the facile, rapid, and inexpensive synthesis of a polyP NP encapsulated in a liposome as a potential procoagulant nanotherapy imitating human platelet dense granules. All the materials are biocompatible and biodegradable, and the process could conceivably be scaled in an economical manner. High-resolution TEM and EEL spectrum imaging of ADGs confirm the nanostructure of a 200-nm sterically stabilized liposome shell encapsulating a 150-nm diameter granular polyP NP core. A label-free direct graphene sandwich approach was used in electron microscopy experiments to prevent beam-induced mass loss and morphology change. Light scattering measurements of ADGs in suspension indicate that the procoagulant nanoparticle is colloidally stable. Triggered initiation of FXII autoactivation by ADGs via

detergent solubilization or phospholipase hydrolysis of the liposomal envelope in an *in vitro* model lends direction in the future for an *in vivo* investigation into ADGs' efficacy in activating the contact system of clotting with the objective to limit blood loss following a severe hemorrhagic event.

CHAPTER 4. INORGANIC POLYPHOSPHATE FOR GENERIC PROTEIN DELIVERY APPLICATIONS

4.1. Introduction

Perfected by natural selection over countless iterations, proteins are evolution's molecular machines tasked with implementing the majority of cellular processes.¹⁶⁴ At the nanoscale, a polypeptide's function is interwoven with its ability to form a specific complex configuration called the folded state.¹⁶⁵ This process is driven by a concatenation of interactions, including hydrogen bonding, disulfide bridging, electrostatic and van der Waals forces, information all encapsulated in the linear arrangement of the protein's amino acids.¹⁶⁶ Even subtle deviations in the physiological environment may disturb the thermodynamics of protein folding and lead to denaturation and loss of crucial biochemical functions.¹⁶⁷ However, countervailing measures, activated in response to environmental triggers such as elevated temperatures or changes in cytosolic pH, exist to limit negative ramifications to cellular metabolism.¹⁶⁸ Organisms employ biochemical "chaperones," which are normally other proteins that are more robust and resistant to environmental changes themselves.¹⁶⁹

Although several examples of generic protein chaperones exist, for instance those that aid in the folding of translated polypeptides,¹⁷⁰ there is little precedent, to the best of our knowledge, for a non-proteinaceous chaperone with similar depth and versatility of function documented in the literature. Some low molecular weight species like trehalose and betaine have some canonical "chaperone-like" effects, but fail to exert the full suite of protective functionality.¹⁷¹ Recently, however, Ursula Jakob and colleagues at the University of Michigan argue that polyP has fulfilled the gamut of molecular chaperone functionality since life's earliest stages, and continues to protect myriad polypeptides from chemical and environmental stressors.³⁶

FVIII zymogen is encountered in the blood stream bound to von Willebrand Factor (vWF).¹⁷² It plays an indispensable role in hemostasis, as it forms part of the intrinsic tenase complex together with FIXa after proteolytic activation by thrombin.⁴⁸ Congenital deficiencies in the coagulation factor present as uncontrolled bleeding episodes, a condition referred to as Hemophilia A.¹⁷³

The intrinsic tenase complex self-assembles on negatively charged phospholipid membranes together with calcium cations. Previous results in the literature suggest that templating surfaces with increasing mole fractions of phosphatidylserine (PS) more facilely promote protein co-localization,¹⁷⁴ suggesting that the presence of negatively charged phospholipids dictates protein binding. Indeed, FVIIIa possesses a short (~20 amino acid), highly conserved motif rich in arginines and other positively charged amino acid residues capable of forming electrostatic interactions with PS.¹⁷⁵

When two oppositely charged polyelectrolytes, such as positively charged poly(arginine) and negatively charged poly(glutamic acid), are mixed at neutral pH in an aqueous solvent environment, electrostatic forces drive association of the two polymers together to form a polyelectrolyte complex.¹⁷⁶ Complex coacervation is a phenomenon characterized by the creation of another liquid phase after addition of a third component to a two-polyelectrolyte suspension.¹⁷⁷ One liquid phase is depleted of the polyelectrolytes, while the coacervate phase has a high density of colloidal polyelectrolyte complexes.¹⁷⁸ The coacervate phase often manifests as suspended droplets in the suspension.¹⁷⁹

Leveraging the physiological phenomenon of intrinsic tenase self-assembly on negatively charged templating surfaces with calcium cations and the coacervative ability of polyP, it is proposed that polyP and FVIII can be co-nanoprecipitated in the presence of calcium cations to

form a polyP-FVIII complex and subsequently encapsulated in sterically stabilized liposomes for possible directed delivery of proteinaceous procoagulant agents to the bleeding site. DLS demonstrates that ADG-FVIII NPs are colloidally stable if stored at 4°C for 20 h, whereas bare polyP-FVIII NPs precipitate out of suspension in less than 1 h. The encapsulation efficiency is quantified to be about 50% by Bradford Assay following a conventional protocol before any additional separation steps. Therefore, unencapsulated FVIII is removed by ultracentrifugation before downstream clotting tests with modest success. Purified ADG-FVIII NPs are subsequently assayed for their ability to reduce their time to clot in FVIII-deficient human plasma, a simplified *in vitro* model of Hemophilia A. The data suggest that ADG-FVIII NPs in the presence of above-threshold concentrations of PLC begin to restore the normal clotting time phenotype when measured against FVIII-deficient plasma spiked with 0.7 nM FVIII concentrate and polyP. Taken together, these results support the hypothesis that ADGs may be loaded with therapeutic proteins by leveraging the ability of polyP to function as a molecular chaperone.

4.2. Experimental Section

4.2.1. Materials and Reagents

Human FVIII concentrate (FVIII), $\text{CaCl}_2 \cdot 6\text{H}_2\text{O}$, and PLC from *C. perfringens* were purchased from Sigma Aldrich (Saint Louis, MO, USA). Citrated pooled normal plasma (PNP) and FVIII-deficient plasma were purchased from George King Biomedical (Overland Park, KS, USA). 1,2-dilinoleoyl-*sn*-glycero-3-phosphocholine (DLPC, 16:2), 1,2-dipalmitoyl-*sn*-glycero-3-phosphocholine (DPPC, 16:0), 1,2-dipalmitoyl-*sn*-glycero-3-phosphoethanolamine-N-[methoxy(polyethylene glycol)-2000] (ammonium salt), (PEG_{2k}DPPE, 16:0), in addition to the Avanti® Mini Extruder and 200-nm polycarbonate membranes were obtained from Avanti Polar

Lipids (Alabaster, AL). PolyP₇₀, or Natriumpolyphosphat P70 (BKGP70) was purchased BK Guilini GmbH (Ludwigshafen am Rhein, Germany). Water was deionized using a Nanopure II filtration system (Barnstead, Dubuque, IA) to 18.2 MΩ-cm. All materials were purchased at standard grades and used as received.

4.2.2 Co-nanoprecipitation of PolyP and FVIII

Aqueous polyP₇₀ (BKGP70, 2 µl of 737 mM) was micropipetted into a mixture containing 50 µl of 0.139 mM FVIII. The polyP/FVIII mixture was subsequently added dropwise to 1500 µl of 5 mM CaCl₂ to give a final polyP polymer: FVIII protein stoichiometric ratio of approximately 1:1. The polyP/FVIII coprecipitate's hydrodynamic diameter, polydispersity, and scattering count rate were determined by DLS (Brookhaven NanoDLS™, Brookhaven, NY).

4.2.3 Synthesis of DLPC/DPPC/PEG_{2k}DPPE Liposomes

Large unilamellar vesicles (LUVs) (size about 200 nm, with 37.5mol% DLPC/57.5mol% DPPC/ 5mol% PEG_{2k}DPPE) were synthesized by membrane extrusion by a conventional protocol in the literature with minor modifications. In short, 81.38 µl 10 mM DLPC and 14.51 µl 10 mM DPPC, both in chloroform, were pipetted into a small scintillation vial, and 186.1 µl of the resulting 40 mol% DLPC/60 mol% DPPC mixture was added to 14.7 µl 10 mM PEG_{2k}DPPE in chloroform, yielding 37.5mol% DLPC/57.5mol% DPPC/ 5mol% PEG_{2k}DPPE after combination. The solution was subsequently bubbled with Ar gas to form a lipid cake, further dried under vacuum for 1 h, and finally rehydrated with 1 mL DI H₂O. To form 200-nm LUVs, the rehydrated phospholipids were passed through an Avanti® mini-extruder with a 200-nm pore-diameter polycarbonate membrane at least 11 times.

4.2.4 Encapsulation of polyP-FVIII NPs in Sterically Stabilized Liposomes

Bare polyP-FVIII NPs suspension (450 μ l) produced in 4.2.2. are added to 78.89 μ l of 2.6 mM 200-nm 37.5mol% DLPC/57.5mol% DPPC/ 5mol% PEG_{2k}DPPE LUVs and sonicated for 10 min.

4.2.5 Ultracentrifugation of ADG/FVIII NPs

ADG-FVIII NPs suspension (500 μ l of 5 mM monoP) were centrifuged 5X at 4500 rpm. After each centrifugation step the supernatant was removed and the pellet was gently resuspended in 500 μ l of 5 mM CaCl₂.

4.2.6 FVIII Encapsulation Efficiency

FVIII encapsulation efficiency was determined by measuring the difference in the total mass of free floating FVIII in ADG-FVIII NP suspension incubated with and without 0.5% (v:v) Tween 20 and 10 mM sodium citrate, dividing the result by the total mass of FVIII added and multiplying by 100%. The nonionic detergent Tween 20 solubilizes the phospholipid envelope, exposing the bare polyP-FVIII NPs. Excess citrate ions will then dissolve the polyP-FVIII complex by outcompeting polyP for calcium chelation. Therefore, addition of these two agents will result in FVIII and polyP returning to a molecularly dissolved state. In short, 5 mM ADG-FVIII NPs were ultracentrifuged at 4500 rpm for 10 minutes and the supernatant was collected. The protein concentration was measured by Bradford Assay following a standard protocol. A FVIII calibration curve from 0-2 mg/ml was used as an internal standard.

4.2.7 Microplate-Based Clotting Assay in FVIII-Deficient Human Plasma with PLC

ADG-FVIII (10 μ M monoP) suspensions were assayed for their ability to reduce the time to clot in FVIII-deficient plasma in the presence of above-threshold concentrations of PLC before (ADG-FVIII BC) and after (ADG-FVIII AC) centrifugation to remove any free-floating

FVIII. For the ADG-FVIII samples digested with phospholipase enzyme, the ADG-FVIII NPs were digested with either 0.3 or 3.3 μM PLC from *C. perfringens* for 20 min at 37°C in a buffer containing 5 mM CaCl_2 , 10 μM ZnCl_2 , 0.1 wt% BSA, and 50 mM Tris-HCl, pH 7.4. Coagulation was initiated by adding 50 μl of citrated FVIII-deficient plasma containing 75 μM PCPS vesicles to 50 μl of 25 mM CaCl_2 , 5 mM imidazole pH 7.4. 50 μl of the PLC-digested ADG-FVIII NPs were then immediately added to the recalcified plasma, and the optical turbidity at 405 nm (A_{405}) was measured every min for 90 min using a FinstrumentsTM Microplate Reader (MTX Lab Systems, Vienna VA). The curvilinear turbidity curve was fitted to a standard Boltzmann sigmoidal function in OriginPro 8.6 (OriginLab Corporation, Northhampton, MA). The coagulation time was defined as the averaged x-coordinate at which the inflection point (x_0) occurs of the respective fitted Boltzmann functions plus or minus the standard error of the mean.

4.3 Results and Discussion

FVIII was co-nanoprecipitated with polyP in aqueous calcium chloride and encapsulated in sterically stabilized, 200-nm liposomes by ultrasonication, forming ADG-FVIII NPs for delivery of clotting factors to the bleeding site. The lipid composition of the vesicle envelope was modified from the original composition to contain a controlled combination of 37.5 mol% DLPC, 57.5 mol% DPPC, and 5 mol% mPEG₂₀₀₀-DPPE for enhanced structural stability. **Figure 4.2** shows the colloidal stability of bare polyP-FVIII NPs and ADG-FVIII NPs over 20 hours. Upon addition of 5 mM polyP to a 5 mM CaCl_2 -FVIII suspension, the resulting particles have a hydrodynamic diameter of approximately 200 nm, marginally larger than bare polyP NPs prepared at equivalent supersaturation ratios (**Chapter 2**). The polyP-FVIII complex is incipiently unstable and rapidly precipitates out of suspension within 1 h. In contrast, after 10

min of ultrasonication with PEGylated vesicles, the ADG-FVIII NPs are approximately 160 nm, in close agreement with pure ADGs without complexed protein. Moreover, the size of ADG-FVIII NPs maintain approximately the same size 20 h after synthesis when refrigerated at 4°C.

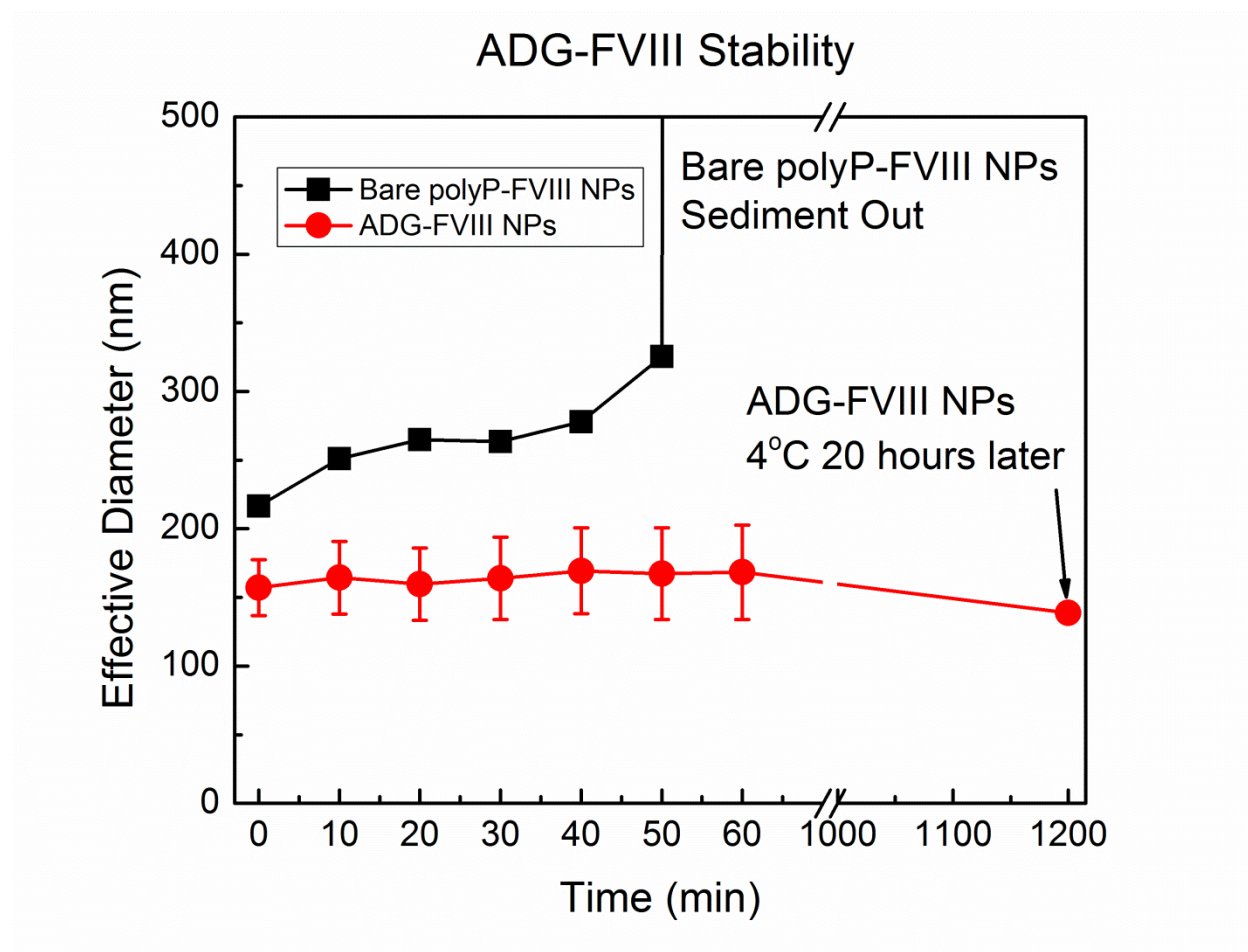


Figure 4.1. Colloidal stability of bare polyP-FVIII and ADG-FVIII NPs in 5 mM CaCl₂.

ADG-FVIII NPs are approximately 160 nm and are colloidally stable for nearly 20 h if they are refrigerated at 4°C. However, the effective diameter of bare polyP-FVIII NPs is initially 200 nm, and the particles substantially ripen within 1 hr, at which point they begin to sediment from the suspension.

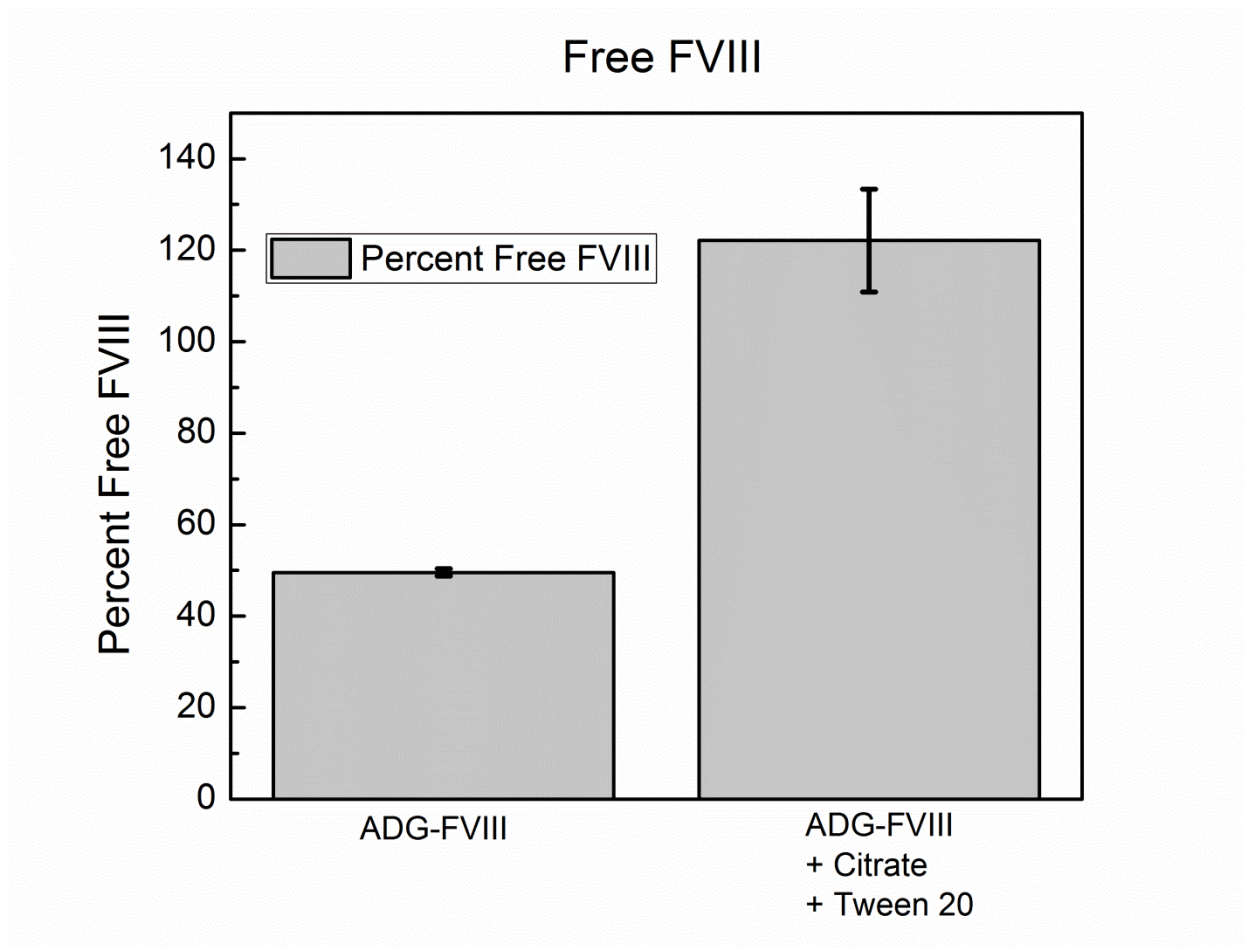


Figure 4.2 Free un-encapsulated FVIII in ADG-FVIII NPs Suspensions Determined by Bradford Assay. The fraction of free form FVIII measured in ADG-FVIII suspensions is approximately 50%, indicating that half of the protein is unencapsulated. ADG-FVIII incubated with the non-ionic detergent Tween 20 to dissolve the liposomal envelope and sodium citrate to dissolve the polyP particle shows nearly complete recovery of free form FVIII in suspension. Therefore, the encapsulation efficiency is approximately 50%.

After characterizing the particle's colloidal stability by light scattering, the FVIII encapsulation efficiency was determined by Bradford (Coomassie Blue) assay following conventional protocol in the literature. Briefly, the total mass of free unencapsulated FVIII in

suspension was measured in ADG-FVIII NP suspensions incubated with and without 0.5% (v:v) Tween 20 and 10 mM sodium citrate before any additional separation steps. The nonionic detergent solubilizes the lipid envelope, while the citrate ions present at stoichiometric excess will readily outcompete polyP for calcium cation chelation, leading to particle dissolution and disassembly of complexed FVIII. ADG-FVIII NPs treated with Tween 20 and excess sodium citrate then should theoretically give approximately 100% recovery of free FVIII by mass balance, and the encapsulation efficiency is given by subtracting this quantity from the percentage of free FVIII in the ADG-FVIII suspension not incubated with detergent or calcium chelator. The results indicate that close to 100% (reasonably close to the margin of experimental error) is recovered in the ADG-FVIII sample treated with 0.5% (v:v) Tween 20 and 10 mM sodium citrate, while 50% of FVIII remains in suspension in ADG-FVIII samples without incubation with detergent or calcium chelator. Thus, the FVIII encapsulation efficiency is measured to be approximately 50%.

Given the significant fraction of free FVIII remaining in suspension, it was attempted to separate the unencapsulated FVIII ADG-FVIII NPs by ultracentrifugation to mitigate downstream adverse ramifications on potential, targeted drug delivery applications. ADG-FVIII NPs were centrifuged 5X at 4500 rpm for 10 min, and the pellet consisting of the liposomal particles was gently resuspended in fresh calcium chloride solution before assaying for procoagulant activity in Hemophiliac plasma. The sedimentation conditions and pelleting time were determined by calculating the ADG-FVIII sedimentation coefficient in Svedberg units given the radius of the centrifuge.¹⁸⁰

Estimated density ρ	Ratio of radii k	ADG-FVIII Mass (S_v)	rpm	$t \text{ min}$
1.3	4730	32500	4500	>8.73

Table 4.1. Centrifugation parameters for removing free FVIII from ADG-FVIII NPs.

A Bradford Assay performed on ADG-FVIII NPs after 5X centrifugation indicates, however, that the free FVIII concentration in the ADG/FVIII eluate has not substantially decreased, and the total mass of FVIII recovered in ADG/FVIII samples incubated with 0.5% (v:v) Tween 20 and 10 mM sodium citrate remains equivalent to the total amount of FVIII added (in fact *much* greater than 100%). Clearly, the equivocal results indicate that the protocol for separating free FVIII from the ADG-FVIII suspension demands further optimization.

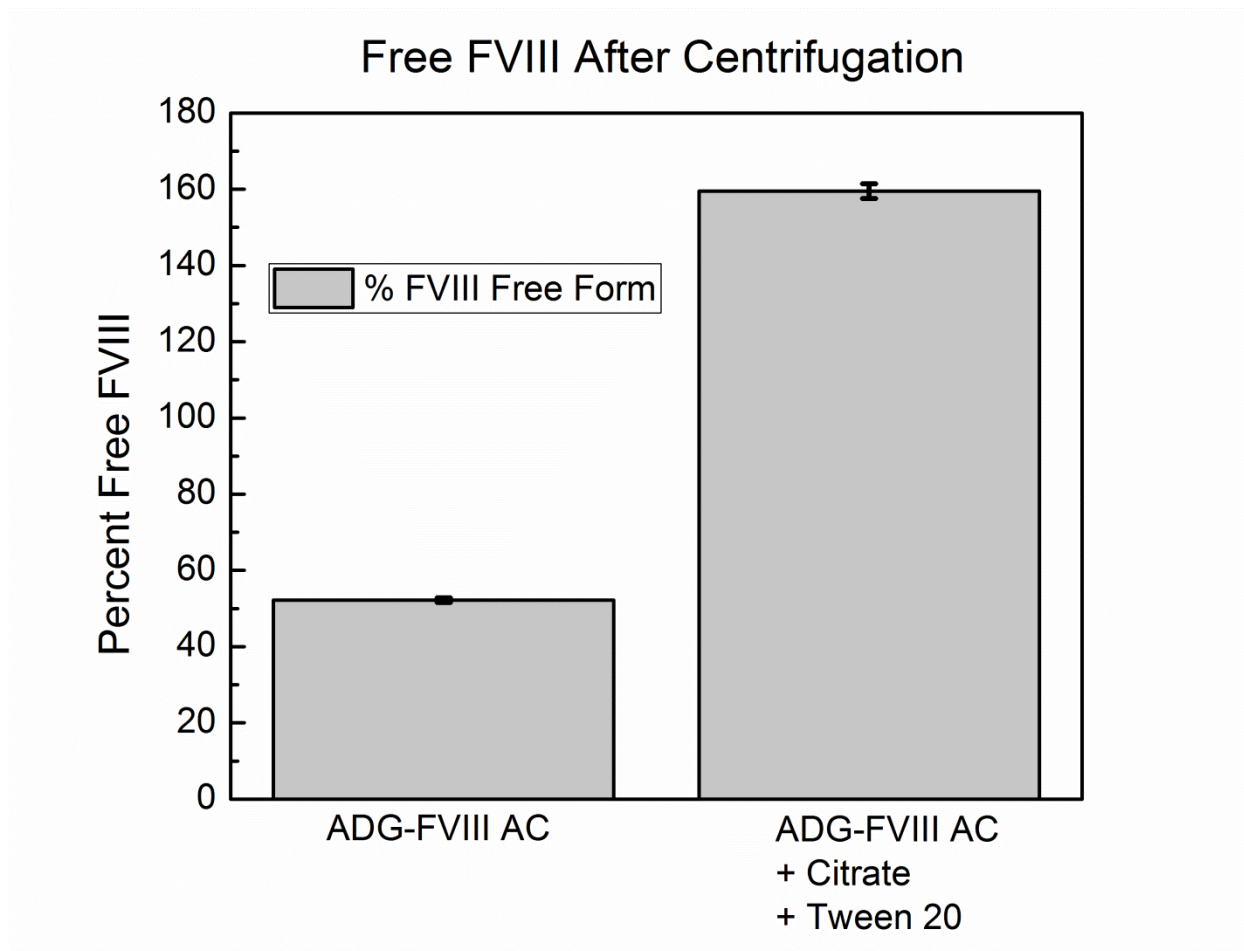


Figure 4.3 Free un-encapsulated FVIII in ADG-FVIII NPs Suspensions Determined by Bradford Assay.

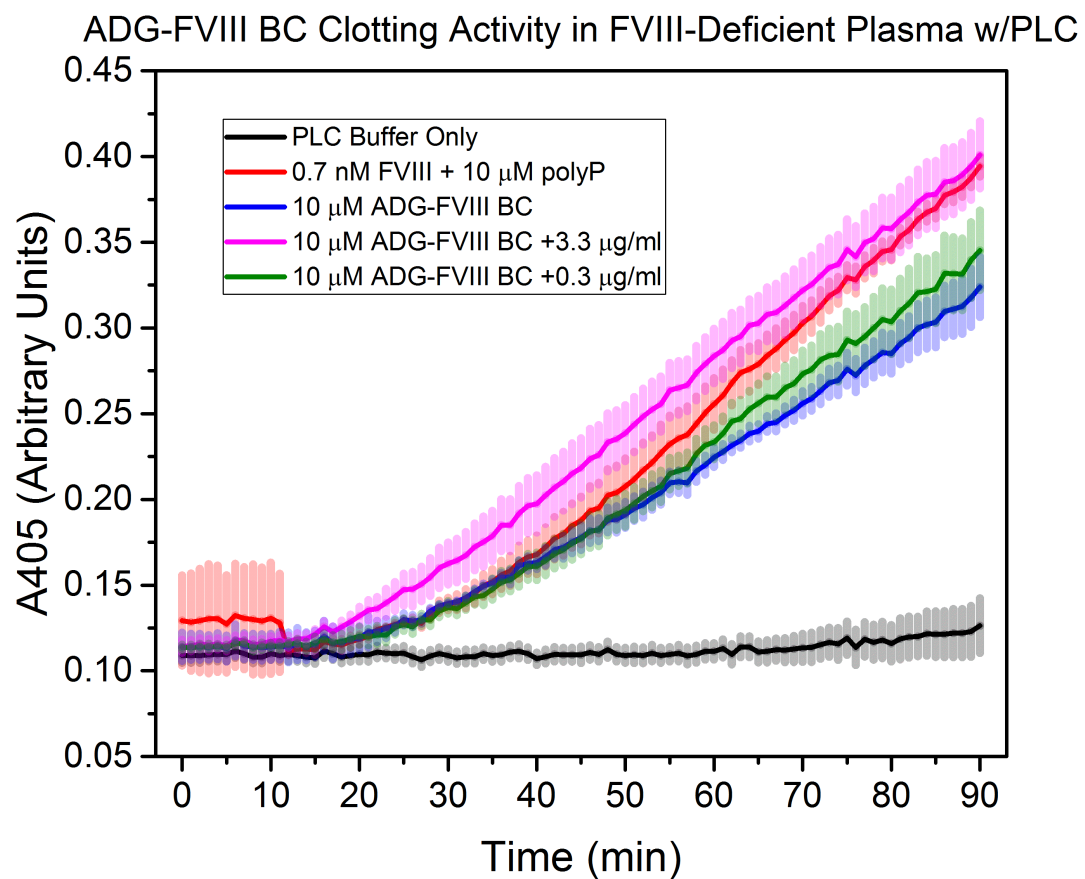


Figure 4.4. Clotting activity of ADG-FVIII NPs before centrifugation (ADG-FVIII BC) in FVIII-Deficient plasma after PLC digestion.

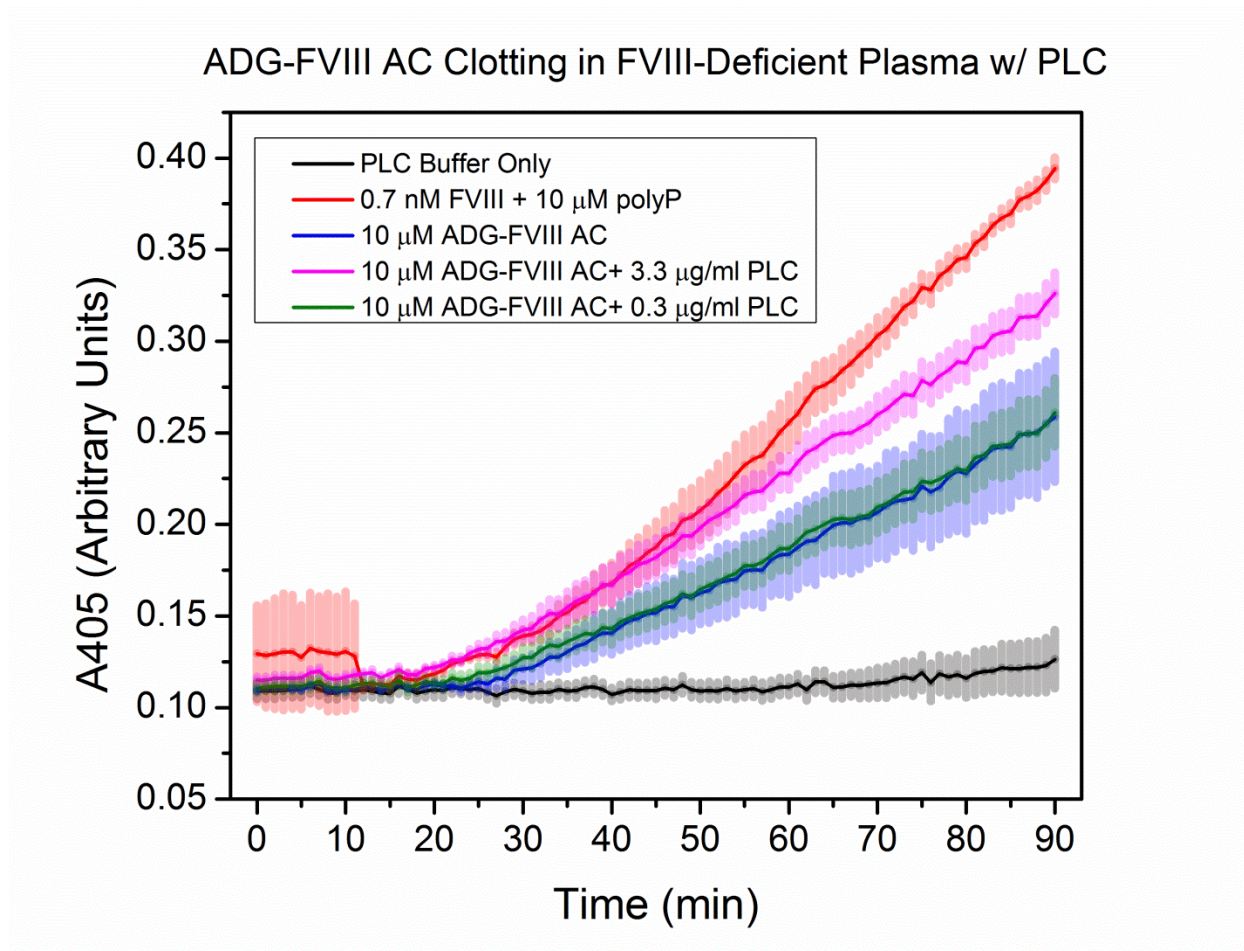


Figure 4.5. Clotting activity of ADG-FVIII NPs after centrifugation (ADG-FVIII AC) in FVIII-deficient plasma after PLC digestion.

The procoagulant behavior of ADG-FVIII NPs was assessed in FVIII-deficient human plasma, a simplified *in vitro* model of Hemophilia A. **Figure 4.4** shows the sigmoidal optical absorbance traces measured at 405 nm (A_{405}) in a microplate reader every min for 90 min against a control containing 0.7 nM FVIII (normal physiologic serum concentration in non-Hemophiliac human patients) and 10 μ M molecularly dissolved polyP that manifests typical reductions in clotting time similar to recalcified PNP with added polyP activator reported in the literature. 10 μ M ADG-FVIII NPs before and after centrifugation steps to eliminate unencapsulated, free

floating FVIII were digested with above-threshold PLC concentrations of 0.3 and 3.3 μM (cf. **Chapter 3**; PLC at these concentrations alone does not activate the contact pathway of clotting in citrated PNP.). **Figure 4.4A** shows that 10 μM ADG-FVIII NPs before centrifugation (noted as *ADG/FVIII BC* in **Figure 4.4A**) incubated with 3.3 μM PLC are equivalent to the control containing 0.7 nM FVIII + 10 μM molecularly dissolved polyP, whereas the reduction in the clotting time of 30 μM ADG-FVIII BC with 0.3 μM PLC is moderately less procoagulant than its counterpart with more phospholipase, presumably due to incomplete phospholipase digestion and release of clotting factor and available polyP surface. 10 μM ADG-FVIII BC without phospholipase trigger show a significant absorbance increase, suggesting that free form FVIII that was not encapsulated in the ADGs is able to reduce the time to clot compared to control without any activator present. **Figure 4.4B** indicates that 10 μM ADG-FVIII NPs after centrifugation (noted as *ADG-FVIII AC* in **Figure 4.4B**) are not nearly as robust as ADG-FVIII NPs BC digested with equivalent PLC concentrations. This phenomenon may be attributed to the fact that the separation protocol has not been fully developed. Furthermore, it may be that the ADG-FVIII NP yield is less than 100% after the separation and purification steps due to the presence of unpelleted ADG-FVIII NPs remaining in the supernatant. Thus, the stated monolipid concentration for the ADG-FVIII NPs AC may be less than that for the ADG-FVIII NPs BC. In order to quantify the recovered ADG-FVIII concentration after the separation steps, the total mass of phospholipids could be quantitated by a myriad of techniques known in the literature. Moreover, ADG-FVIII AC without phospholipase still is more active than control with no activator, suggesting that free form FVIII remains in suspension or that polyP and FVIII may be prematurely released in FVIII-deficient plasma. The sample containing no activator or 0.7 nM FVIII did not coagulate during the time measured in the assay as noted by the horizontal

absorbance trace. An additional control experiment not yet performed would be to rescue the normal phenotype by spiking human FVIII concentrate into FVIII-deficient plasma without activator present.

4.4 Conclusion & Future Directions

Employing polyP's ancient evolutionary functionality as a critical molecular chaperone in the design of a threshold-switchable procoagulant nanoparticle to transport therapeutic proteins, an initial platform is constructed for the complex coacervation of human FVIII and polyP with aqueous calcium cations serving as the coacervating agent. The protein and anionic polyelectrolyte are mixed and co-nanoprecipitated in 5 mM CaCl₂. The resulting polyP-FVIII complexes are encapsulated into PEGylated phospholipid vesicles by brief ultrasonication, following the synthetic protocol for the original ADG prototype. Investigation of the particles' colloidal stability by DLS indicates that bare polyP-FVIII complexes are incipiently unstable and sediment out of suspension within 1 h, while the encapsulated ADG-FVIII NPs are approximately 160 nm like ADG without encapsulated protein and are stable for at least 20 h if refrigerated at 4°C. FVIII encapsulation efficiency was measured to be approximately 50% by Bradford Assay, and free floating FVIII could be partially removed by successive centrifugation steps. Further optimization is required to further reduce free FVIII and premature release of FVIII. The procoagulant behavior of the ADG-FVIII NPs was evaluated in a simplified *in vitro* model of FVIII deficiency by a turbidity-based microplate assay using FVIII-deficient plasma obtained from human patients. ADG-FVIII NPs incubated with above-threshold concentrations of PLC begin to restore normal clotting behavior, although more study is necessary to elucidate its procoagulant behavior: the true monoP concentration of ADG/FVIII NPs AC was not

quantified. Further, another control containing only FVIII that resembles recalcified, citrated PNP without activator present in clotting time would be of interest to compare against results with ADG/FVIII NPs samples in FVIII-deficient plasma.

CHAPTER 5. FUTURE DIRECTIONS TOWARD A BIOINSPIRED NANOPARTICLE HEMOSTAT

5.1 Introduction

The foundation has been constructed in earlier chapters for an artificial platelet nanotherapy employing condensed granules of inorganic polyP and a stealth liposome technology. In addition, it has been shown that these particles serve as vectors for therapeutic protein delivery. These ADGs have a demonstrated ability to initiate conversion of FXII zymogen to its activated form FXIIa in isolated clotting factor assays and reduce the time to clot in *in vitro* models of the contact pathway of blood coagulation in recalcified human blood plasma. *In vitro* release of polyP from the PEGylated lipid envelope is triggered by the enzyme activity of phospholipases at concentrations above a threshold value. In the human body certain isoforms of the enzyme are present at sites of inflammation including hemorrhage at concentrations orders of magnitude higher than normal physiological serum levels. After dosing ADGs to treat a bleeding event, it is imagined that these threshold-switchable characteristics would translate *in vivo* to exploit the human body's intrinsic inflammatory and hemostatic mechanisms to accelerate blood clotting.

Notwithstanding, the ADGs described here only represent the first iteration of a prototype in the synthesis of a veritable nanoparticle hemostat with threshold-switchable characteristics. Presently evidence solely demonstrates that ADGs are threshold-switchable particles with procoagulant (not *hemostatic*) effects in simplified *in vitro* models. To progress past the proof-of-principle stage and to later, more robust iterations of an ADG hemostat, a systematic experimental agenda is therefore necessary. The objective toward a veritable threshold-switchable nanoparticle hemostat is to be realized by improving ADG structural integrity,

enhancing homing to the injury site, improving its ability to act synergistically with the human body's own blood platelets, and enhance its procoagulant effects via incorporation of small molecules, peptides, or proteins. Further, these new ADG iterations must necessarily be assayed in more complex and realistic models of traumatic hemorrhage, including assays entailing the use of fresh whole blood without anticoagulant, endogenous phospholipases, platelet releasates, microfluidic devices with physiologic flow conditions, and live animal experiments. The components of this two-sided experimental agenda are presented in detail below.

5.2 Synthesis of Novel ADG Iterations

The synthetic approach toward an efficacious, threshold-switchable nanoparticle hemostat is further divided into three strategies, which entails modification of the liposomal envelope composition, surface decoration by covalent conjugation or physical adsorption of ligands, and encapsulation of other adjuvant small molecules, peptides and proteins with procoagulant and antifibrinolytic properties.

5.2.1 Improve ADG Structural Integrity

The original ADG prototype consists of a liposomal envelope of 95 mol% L- α -PC derived from a natural source (soy) and 5 mol% PEG_{2k}DPPE. While deriving materials from natural sources (as in the case of L- α -PC) may be generally advantageous in the construction of a nanoscale drug delivery platform as a first principle, the structural stability of nanotherapeutic liposomes demands further development beyond these natural phospholipid sources, so as to ensure longer circulation half-life and optimize drug release kinetics.¹⁸¹ Further, the liposome hydrolysis kinetics, itself dependent on the liposome composition, has not been tailored for acceleration of coagulation subsequent to hemorrhagic events.

As such, a systematic investigation of liposomal colloidal stability, polyP release rate, and phospholipase hydrolysis kinetics will be performed to identify optimal combinations of saturated and unsaturated phospholipids, sterols (e.g. cholesterol), sphingolipids (e.g. sphingomyelin), and polymer-conjugated phospholipids (e.g. PEG_{2k}DPPE). It would be logical to construct the next ADG iteration by beginning with a liposomal shell composed of a controlled combination of the two most abundant components in L- α -PC, dipalmitoylphosphatidylcholine (DPPC, 16:0), and dilinoleoylphosphatidylcholine (DLPC, 18:2 cis), and a small molar percentage of PEGylated PE for steric stabilization and enhanced enzyme degradation. By varying the ratio of DPPC:DLPC away from the 14.9:63.0 mol/mol ratio in L- α -PC, one could investigate ADG structural integrity as a function of membrane fluidity.

Further modifications could be attempted to supplement membrane strength and rigidity if a DPPC: DLPC: PEG-PE combination is not sufficient by incorporating sterols or sphingolipids such as cholesterol, sphingomyelin, or cardiolipin. These lipids function as spacers between phospholipids, simultaneously creating stiffer and more impermeable vesicles.¹⁸² Several liposomal nanotherapeutics on the market typically contain high-melting temperature, long-chain saturated phospholipids (e.g. HSPC) and up to 40mol% cholesterol to ensure vesicle structural integrity and prevent premature drug release.¹⁸³

The effect of PEGylation on hydrolysis kinetics has not been substantially corroborated in the literature. Scattering techniques such as DLS, SAXS, and SANS could also be exploited to interrogate the relationship between vesicle composition and its degradation rate in the presence of phospholipases. DLS in flow mode is a robust method to determine kinetic parameters with a temporal resolution of approximately 1 s. ADGs will be incubated with various phospholipase isoforms at 37°C, and continuously flowed through the DLS, where the hydrodynamic diameter

will be measured versus time after addition of the enzyme. As the vesicles are degraded, the effective diameter will increase and follow a conventional sigmoidal growth curve, characterized by a lag phase (no hydrolysis occurring), an exponential growth phase (hydrolysis rapidly occurs), and a plateau phase (the rate of hydrolysis has slowed substantially). The sigmoidal growth curve will be fitted to a Boltzmann sigmoidal growth function to extract the enzyme lag time, initiation of hydrolysis, and other kinetic parameters pertaining to hydrolysis.

5.2.2 Enhance Homing to the Injury Site & Promoting Synergistic Activity with Human Platelets

While optimization of lipid composition will ensure superior structural integrity, prevent premature polyP leakage, and promote faster ADG hydrolysis at the inflammation site, additional synthetic strategies should be pursued to develop multiple targeting pathways. This approach may entail covalently modifying or physically decorating the liposomal envelope with proteins, peptides, and/or small molecules that are directed to hemorrhagic injuries and, furthermore, additional moieties that interact with other prohemostatic actors such as human platelets, coagulation factors, and fibrin.

Possible candidates include the proteins p-selectin, fibrinogen, and integrin $\alpha 2\beta 1$. P-selectin is stored on the inner membrane of human platelet α granules. Upon platelet stimulation, the protein is flipped to the outer leaflet after the granule is secreted into the circulation, where it functions to mobilize and marginate activated platelets.¹⁸⁴ Fibrinogen is the precursor to monomeric fibrin and would accelerate fibrin clot formation in the presence of thrombin.¹⁸⁵ Integrin $\alpha 2\beta 1$ is a collagen adhesion protein expressed on the outer leaflet of activated platelets, allowing ADGs to co-accumulate with platelets at the injury site, where collagen is exposed to the vasculature.¹⁸⁶

Several benign coupling chemistries are compatible with phospholipids for covalently attaching generic polypeptides to the surface of liposomes, two of which will be discussed here for their biocompatibility and robustness. Maleimide chemistry involves the covalent coupling of a maleimide-functionalized substrate with a polypeptide containing a cysteine residue under aqueous conditions at near neutral pH.⁸¹ The primary sulfhydryl group on the protein's cysteine residue serves as the nucleophile, attacking the double bond and forming a strong thioether linkage. Maleimide groups can easily be conjugated to PEGylated phosphoethanolamines and are readily commercially available.¹⁸⁷ Polypeptides of tens to hundreds of residues generally have one or more available cysteines, and, as such, maleimide coupling serves as a robust conjugation platform regardless of protein substrate.

Another alternative is carbodiimide coupling chemistry involving the formation of an amide bond between a carboxylic acid and the amino terminus of a protein substrate. The carboxylate of a PEG_{2k}DPPE-COOH could be activated by addition of a commercially available carbodiimide such as 1-ethyl-3-(3-dimethylaminopropyl)carbodiimide (EDC) to form a high energy isourea intermediate in an aqueous solvent at slightly acidic. The amino terminus of a protein substrate functions as the nucleophile to form an amide bond to yield Protein-NH-OOC-PEG_{2k}DPPE, for example.¹⁸⁸ Protein conjugation could be accomplished by adding the protein substrate directly into a suspension of preformed ADGs with functionalized PEGPE, in conjunction with activators such as EDC. In order to separate unconjugated protein substrate after reaction, dialysis or centrifugation could be performed.

5.2.3 Encapsulation of Small Molecules, Peptides, and Proteins to Enhance Procoagulant Effect

After the liposomal envelope composition has been optimized for structural stability and phospholipase hydrolysis rate and functionalized with proteins to improve its homing to the bleeding site and its synergistic activity with human platelets, the third ADG iteration would leverage polyP's molecular chaperone characteristics in order to enhance ADG procoagulant efficacy. Surface plasmon resonance (SPR) and DLS experiments can be employed to screen polyP binding with a multitude of proteins or peptides with prohemostatic effects, as in the previous chapter. Possible targets for encapsulation already known to bind with polyP with K_d 's below 100 nM include von Willebrand Factor (vWF), FXIa, thrombin, and kallekrein. VWF is a large glycosylated polypeptide that binds to collagen exposed at the bleeding site and stimulates platelet margination via interaction with another glycosylated protein expressed on platelets' cell membranes.¹⁸⁹ FXIa and kallekrein are consequential in propagation of the procoagulant stimulus in the contact pathway of blood clotting. Fibrinogen-functionalized ADGs encapsulating thrombin would thus greatly accelerate fibrin clot formation.¹⁹⁰

In order to synthesize the third generation platelet-mimetic ADG, a generic scheme would be as follows: (1) polyP would be co-nanoprecipitated with vWF, FXI, thrombin, and/or kallekrein in 5 mM CaCl_2 , (2) mixed with terminus-modified PEGylated liposomes, (3) sonicated for 10 min, (4) allowed to react with multiple protein substrates such as p-selectin, fibrinogen, and/or integrin $\alpha_2\beta_1$ for surface decoration, and (5) separated from unconjugated protein substrate by dialysis or ultracentrifugation.

5.3 Assaying Hemostatic Efficacy in More Complex Models of Traumatic Hemorrhage

The tripartite synthetic approach could be validated by experiments more representative of hemorrhagic bleeding scenarios in order to justify ADG's use as a potential hemostatic agent. The prohemostatic effects of the platelet-mimetic ADGs developed in **Section 5.1** could be assessed by increasingly elaborate *in vitro* clotting assays and in *in vivo* traumatic injury models, as described below.

5.3.1 *In Vitro* Clotting Assays

PolyP exerts multivariate procoagulant effects by interacting with several coagulation factors and inhibitors including FV, FXI, FXII, FXIII, TFPI, and thrombin according to its size.³¹⁻³⁴ ADGs have only been assayed for their contact activity via their ability to autoactivate FXII zymogen in isolation and their ability to reduce clotting time in recalcified PNP, with both assays conducted in microwell plates. In order to more fully explore a wider range of the platelet mimetic ADG's procoagulant effects, other models that study the mechanical, viscous, and optical changes upon coagulation of blood and blood products could be undertaken. Furthermore, these models could help elucidate ADG's role in modulating both the tissue factor pathway and the final common pathway of blood clotting, which are more relevant to hemostasis following traumatic injury. Indeed, polyP's most powerful hemostatic effects are derived from its capacity to attenuate TFPI (tissue factor pathway mechanism) and accelerate prothrombinase formation (final common pathway mechanism) by promoting more rapid FV conversion.³¹ In addition to isolated clotting factor or protein assays and employing citrated PNP, serum, fresh whole blood without anticoagulant, and extracts of endogenous phospholipases derived from human blood platelet releasates could be used extensively when it is practicable. Below, an array of *in vitro*

experiments is proposed to more clearly determine the procoagulant ability of platelet-mimetic ADGs.

The procoagulant ability of platelet-mimetic ADGs would also be evaluated in a coagulometer, a device that employs the oscillatory motion of a metallic ball in a cuvette filled with blood or plasma to determine mechanical and viscous changes upon gelation. As clotting is initiated blood becomes increasingly viscoelastic and impedes the ball's motion until it completely ceases upon crosslinking of the fibrin mesh.¹⁹¹ To complement the microwell-based clotting assays, the ability for platelet-mimetic ADGs to act as a contact pathway activator could be assessed in a coagulometer by addition of ADGs preincubated with Tween 20, PLC, or a platelet releasate containing endogenous secreted phospholipases, to recalcified, citrated PNP or fresh whole blood without anticoagulant following previous reports.¹⁸⁰ Likewise, to interrogate other locations in the coagulation cascade in which polyP intercedes, one could add 83 pM FXa or 33 ng/ml TFPI+167 pM FXa to quantitate ADG's ability to accelerate FVa formation and hinder TFPI function, respectively. A summary of the proposed experimental protocols are given in **Table 5.1**:

Coagulation Pathway	Coagulometric Experiment
Contact Pathway	10-50 μ M ADGs 8.33 mM CaCl_2 1.67 mM Imidazole pH 7.0 25 μ M PCPS 33% PNP or Fresh Whole Blood
Final Common Pathway	83 pM FXa 10-50 μ M ADGs 8.33 mM CaCl_2 1.67 mM Imidazole pH 7.0 25 μ M PCPS 33% PNP or Fresh Whole Blood
Tissue Factor Pathway	33 ng/ml TFPI 167 pM FXa 10-50 μ M ADGs 8.33 mM CaCl_2 1.67 mM Imidazole pH 7.0 25 μ M PCPS 33% PNP or Fresh Whole Blood

Table 5.1. Coagulometric Experiments to Assay ADGs' Ability to Initiate the Contact, Final Common, and Tissue Factor Pathways of Blood Clotting.

5.3.2 Animal Models of Internal Hemorrhage

Once the platelet-mimetic ADGs have realized positive results in further *in vitro* coagulation models in *in vitro* models, successful candidate ADG iterations should be evaluated for their ability to act as a prohemostatic therapy *in vivo*. Although murine and lapine preclinical models of traumatic hemorrhage have been used extensively and successfully in the past,¹⁹² pigs are ideal test subjects due to their similarity in physiology to humans with respect to hemostasis and thrombosis.¹⁹³ Before qualifying the prohemostatic effect, ADG toxicology should be qualified by incrementally titrating upward intravenously administered dosages of ADGs and evaluating thrombogenic, inflammatory, and complement parameters.

Upon completion of a systematic toxicological investigation, *in vivo* trials of ADG prohemostatic efficacy could begin. A robust, preclinical model of traumatic hemorrhage

involves conjoining an artery and an adjacent vein together by a diverting conduit called a shunt. Procoagulant agents may then be administered to marginate in the shunt and trigger fibrin clot formation.¹⁹⁴ This arteriovenous shunt model, as it has become known, will be utilized with platelet-mimetic ADGs in a porcine model with a few modifications. A polymeric shunt composed of a contact-inert material will be layered with streptavidin and blocked with BSA according to standard protocol and conjoined between the femoral artery and vein. Platelet-mimetic ADGs, which have been surface-decorated with biotinylated PEG-PE could be administered intravenously to anaesthetized pigs and elicited to marginate in the femoral shunt via streptavidin binding. Upon sufficient margination of ADGs and platelets, a fibrin clot should form and occlude blood flow. The reduction in the time to clot, and parameters relating to fibrin clot morphology and volume could serve as qualifiers to determine if platelet-mimetic ADGs function as veritable nanoparticle hemostats.

5.4 Conclusion

Transitioning from a successful proof-of-concept toward an efficacious nanoparticle hemostat with threshold-switchable functionality should entail an iterative synthetic strategy, followed by a multivariate experimental evaluation. To begin, the liposomal envelope's composition should be modified to enhance structural integrity and modulate degradation kinetics for optimal procoagulant cargo deployment at the bleeding site. Further modifications to the liposomal surface should promote hemostatic synergism between human platelets at the injury site and encapsulation of polypeptides with adjuvant procoagulant and antifibrinolytic properties can be incorporated to exert further effects on the coagulation cascade. As soon as a platelet-mimetic ADG is perfected from an engineering perspective, it could be evaluated with

more complex models of traumatic hemorrhage. First, the ability of the new ADG iterations to exert procoagulant effects via the final common pathway and TFPI abrogation should be examined by observing optical, mechanical, and viscous changes upon coagulation. As soon as conclusive *in vitro* data supporting the procoagulant behavior of platelet-mimetic ADGs is gathered, the nanoparticles can undergo toxicological studies and evaluations of hemostatic efficacy in a porcine model of hemorrhagic bleeding. Determinants from these *in vivo* experiments should serve as a means to conclude if platelet-mimetic ADGs satisfy the requirements of a hemostatic, threshold-switchable, nanoscale drug delivery platform as originally intended.

CHAPTER 6. CONCLUSIONS

The development of a versatile, on-demand hemostatic agent to mitigate traumatic hemorrhage is arguably consistent with engaging biology's procoagulant actors and mechanisms, leveraging the implicit positive and negative feedback loops in its threshold-switchable networks, and implementing novel combinations thereof to achieve hemostasis more effectively. Compatible with this overarching theme of bioinspiration in medicine, the principal elements of a nanoparticle hemostatic agent are constructed, which rely on the behavior of polyP to self-organize into condensed structures on the nanoscale and, moreover, its complex procoagulant effects through mediation via multiple actors in the clotting cascade. The thermodynamic self-assembly of polyP in metal cation solutions is utilized to store high concentrations of the polyelectrolyte in phospholipid vesicles, nanoscale lipid vectors that resemble cell membranes. In order to exert procoagulant effects in a triggered, nonlinear fashion, an enzyme found in the blood stream which also triggers secretion of human platelet granules, is recruited to hydrolyze the liposome shell.

A complete analysis of the precipitative ability of electrolytes on polyP is given first, with emphasis on biologically encountered concentrations of metal cations such as calcium, magnesium, zinc, sodium, and potassium. Light scattering techniques are utilized to quantify the solubility of polyP under these solvent conditions, and the colloidal stability of the resulting nanoprecipitated polymer. PolyP's tendency to precipitate in metal cation solutions is determined to be correlated with the polyelectrolyte's molecular weight. Larger polymer sizes more easily condense into granules, whereas polymers with less repeating units have higher solubilities. Moreover, the particle's effective diameter is solely controlled by the metal ion concentration, and virtually unaffected by the polyelectrolyte's supersaturation ratio. Finally, the ability of

condensed polyP to reduce coagulation time in a model of the contact pathway of blood clotting is shown in citrated human plasma by a microwell plate assay. This raises the question that polyP granules may play a direct role in the blood clotting cascade.

With knowledge regarding the physicochemical behavior of polyP nanoprecipitation in hand, a benchtop process is sought to construct a procoagulant nanoparticle drug delivery system with injury-homing attributes. Towards this objective, polyP is condensed into nanoparticles under optimized conditions and loaded into stealth phospholipid vesicles. The liposome is composed of 95mol% L- α -PC from soy, a mixture of saturated and doubly unsaturated phosphocholines resembling natural cell membranes, and 5mol% PEG₂₀₀₀-DSPE. A high resolution imaging method suited for biologically inspired materials is used to discern the complex core-shell architecture. Further, the hybrid particle is mapped by EELS to determine its composition. The threshold-switchable procoagulant behavior is qualified by assays involving activation of isolated proteins and models in human plasma for the intrinsic pathway of blood coagulation. These results suggest that the Artificial Dense Granules (ADG) duplicates to the first degree the form and function of its electron dense counterparts in human platelets.

Finally, the framework is created for employing polyP as a protein delivery vector and leveraging this ability to construct targeted procoagulant drug delivery platform potentially capable of transporting clotting factors to the bleeding site. FVIII and polyP are co-nanoprecipitated in the presence of aqueous calcium chloride, and the resulting polyelectrolyte complex is loaded into sterically stabilized liposomes after brief ultrasonication. The ADG/FVIII NPs partially restore clotting in a simplified *in vitro* model of Hemophilia A employing recalcified citrated plasma deficient in FVIII. This raises the possibility for additional procoagulant and antifibrinolytic proteins to be co-delivered in a future ADG prototype for

treating multiple bleeding presentations and coagulopathy beyond traumatic hemorrhage. More broadly speaking More broadly speaking, polyP may serve as a generic platform for nanoscale delivery of myriad classes of therapeutics polypeptides and as a vehicle aiding in the characterization efforts of structural biology, such as in X-Ray crystallography applications.

VITA

Publications

8. M. Szymusiak, J. Kalkowski, **A. J. Donovan**, H. Luo, W. Shang, T. Irving, M. Herrera-Alonso and Y. Liu. “Core-shell Structure and Aggregation Number of Micelles Composed of Amphiphilic Block Copolymers and Polymer Brushes Determined by Small-Angle X-ray Scattering.” *In preparation for submission to Macro Lett.*
7. **A.J. Donovan** and Y. Liu. “Oral Nanotherapeutics with innovations in lipid and polymeric micelle technologies,” *Nanotheranostics for Cancer Applications*. Eds. Stephanie Morris & Prakash Rai. New York City: Springer Publishing Group, *In preparation*.
6. **A.J. Donovan** and Y. Liu. “Chemistode for High Temporal- and Spatial-Resolution Chemical Analysis,” *Open Space Microfluidics*. Ed. Govind V. Kaigala. Weinheim, Germany: Wiley VCH, *In press*.
5. J.H. Yeon, N. Mazinani, T.S. Schlappi, K.Y.T. Chan, J.R. Baylis, S.A. Smith, **A.J. Donovan**, D. Kudela, G.D. Stucky, Y. Liu, J. H. Morrissey, R.F. Ismagilov, and C.J. Kastrup. “Localization of short-chain polyphosphate enhances its ability to clot flowing blood plasma.” *Sci. Rep.* **2017**, 7, 42119.
4. **A.J. Donovan**, J. Kalkowski, M. Szymusiak, C. Wang, S.A. Smith, R.F. Klie, J.H. Morrissey, and Y. Liu. “Artificial dense granules: a procoagulant liposomal formulation modeled after platelet polyphosphate storage pools.” *Biomacromolecules* **2016**, 17(8): 2572-2581.
3. M. Szymusiak*, **A.J. Donovan***, S.A. Smith, R. Ransom, H. Shen, J. Kalkowski, J.H. Morrissey, and Y. Liu. “Colloidal confinement of polyphosphate on gold nanoparticles robustly activates the contact pathway of blood coagulation.” *Bioconjugate Chem.* **2016**, 27 (1), 102–109. (*: These authors contributed equally to this work).
2. **A.J. Donovan**, J. Kalkowski, S.A. Smith, J.H. Morrissey, and Y. Liu. “Size-controlled synthesis of granular polyphosphate nanoparticles at physiologic salt concentrations for blood clotting.” *Biomacromolecules*, **2014**, 15 (11): 3976-3984.
1. **A.J. Donovan**, K. Lansu, J.G. Williams, M.F. Denning, and S. Gentile. “Long QT2 mutation on the Kv11.1 ion channel inhibits current activity by ablating a protein kinase C α consensus site,” *Mol. Pharmacol.* **2012**, 82(3): 428-437.

Patents & Patent Applications

1. Y. Liu and **A.J. Donovan**. “Artificial Platelets for Treating Catastrophic Bleeding.” 24 September 2015. U.S. Patent Application No.: PCT/US2015/051814.

COPYRIGHT PERMISSIONS

CHAPTER 2

THERMODYNAMIC SELF-ASSEMBLY OF INORGANIC POLYPHOSPHATE GRANULES IN AQUEOUS ELECTROLYTE SOLUTIONS

7/4/2017

Rightslink® by Copyright Clearance Center



RightsLink®

Home

Create
Account

Help



ACS Publications
Most Trusted. Most Cited. Most Read.

Title:

Size-Controlled Synthesis of
Granular Polyphosphate
Nanoparticles at Physiologic Salt
Concentrations for Blood
Clotting

Author:

Alexander J. Donovan, Joseph
Kalkowski, Stephanie A. Smith,
et al

Publication: Biomacromolecules

Publisher: American Chemical Society

Date: Nov 1, 2014

Copyright © 2014, American Chemical Society

LOGIN

If you're a [copyright.com](#)
user, you can login to
RightsLink using your
copyright.com credentials.
Already a RightsLink user or
want to [learn more?](#)

PERMISSION/LICENSE IS GRANTED FOR YOUR ORDER AT NO CHARGE

This type of permission/license, instead of the standard Terms & Conditions, is sent to you because no fee is being charged for your order. Please note the following:

- Permission is granted for your request in both print and electronic formats, and translations.
- If figures and/or tables were requested, they may be adapted or used in part.
- Please print this page for your records and send a copy of it to your publisher/graduate school.
- Appropriate credit for the requested material should be given as follows: "Reprinted (adapted) with permission from (COMPLETE REFERENCE CITATION). Copyright (YEAR) American Chemical Society." Insert appropriate information in place of the capitalized words.
- One-time permission is granted only for the use specified in your request. No additional uses are granted (such as derivative works or other editions). For any other uses, please submit a new request.

BACK

CLOSE WINDOW

Copyright © 2017 Copyright Clearance Center, Inc. All Rights Reserved. [Privacy statement](#). [Terms and Conditions](#).
Comments? We would like to hear from you. E-mail us at customer@copyright.com

COPYRIGHT PERMISSIONS

CHAPTER 3

BIOINSPIRED ARTIFICIAL PLATELET NANOPARTICLES

7/4/2017

Rightslink® by Copyright Clearance Center



RightsLink®

Home

Create Account

Help



ACS Publications
Most Trusted. Most Cited. Most Read.

Title:

Artificial Dense Granules: A Procoagulant Liposomal Formulation Modeled after Platelet Polyphosphate Storage Pools

Author:

Alexander J. Donovan, Joseph Kalkowski, Magdalena Szymusiak, et al

Publication: Biomacromolecules

Publisher: American Chemical Society

Date: Aug 1, 2016

Copyright © 2016, American Chemical Society

LOGIN

If you're a copyright.com user, you can login to RightsLink using your copyright.com credentials. Already a RightsLink user or want to [learn more?](#)

PERMISSION/LICENSE IS GRANTED FOR YOUR ORDER AT NO CHARGE

This type of permission/license, instead of the standard Terms & Conditions, is sent to you because no fee is being charged for your order. Please note the following:

- Permission is granted for your request in both print and electronic formats, and translations.
- If figures and/or tables were requested, they may be adapted or used in part.
- Please print this page for your records and send a copy of it to your publisher/graduate school.
- Appropriate credit for the requested material should be given as follows: "Reprinted (adapted) with permission from (COMPLETE REFERENCE CITATION). Copyright (YEAR) American Chemical Society." Insert appropriate information in place of the capitalized words.
- One-time permission is granted only for the use specified in your request. No additional uses are granted (such as derivative works or other editions). For any other uses, please submit a new request.

BACK

CLOSE WINDOW

Copyright © 2017 Copyright Clearance Center, Inc. All Rights Reserved. [Privacy statement](#). [Terms and Conditions](#). Comments? We would like to hear from you. E-mail us at customercare@copyright.com

REFERENCES

1. Kauvar, D. S.; Lefering, R.; Wade, C. E. Impact of hemorrhage on trauma outcome: an overview of epidemiology, clinical presentations, and therapeutic considerations. *J Trauma Acute Care Surg* 2006, 60, S3-S11.
2. Kauvar, D. S.; Wade, C. E. The epidemiology and modern management of traumatic hemorrhage: US and international perspectives. *Crit Care* 2005, 9, S1.
3. EASTRIDGE, B. J.; MABRY, R. L.; SEGUIN, P.; CANTRELL, J.; TOPS, T.; URIBE, P.; MALLET, O.; ZUBKO, T.; OETJEN-GERDES, L.; RASMUSSEN, T. E. Death on the battlefield (2001–2011): implications for the future of combat casualty care. *J Trauma Acute Care Surg* 2012, 73, S431-S437.
4. Champion, H. R.; Bellamy, R. F.; Roberts, C. P.; Leppaniemi, A. A profile of combat injury. *J Trauma* 2003, 54, S13-S19.
5. Wedmore, I.; McManus, J. G.; Pusateri, A. E.; Holcomb, J. B. A special report on the chitosan-based hemostatic dressing: Experience in current combat operations. *J Trauma* 2006, 60, 655-658.
6. Alam, H. B.; Uy, G. B.; Miller, D.; Koustova, E.; Hancock, T.; Inocencio, R.; Anderson, D.; Llorente, O.; Rhee, P. Comparative analysis of hemostatic agents in a swine model of lethal groin injury. *J Trauma Acute Care Surg* 2003, 54, 1077-1082.
7. Rhee, P.; Brown, C.; Martin, M.; Salim, A.; Plurad, D.; Green, D.; Chambers, L.; Demetriades, D.; Velmahos, G.; Alam, H. QuikClot use in trauma for hemorrhage control: case series of 103 documented uses. *J Trauma Acute Care Surg* 2008, 64, 1093-1099.
8. Lawson, J. H.; Lynn, K. A.; Vanmatre, R. M.; Domzalski, T.; Klemp, K. F.; Ortel, T. L.; Niklason, L. E.; Parker, W. Antihuman factor V antibodies after use of relatively pure bovine thrombin. *Ann Thorac Surg* 2005, 79, 1037-1038.
9. Chapman, W. C.; Singla, N.; Genyk, Y.; McNeil, J. W.; Renkens, K. L.; Reynolds, T. C.; Murphy, A.; Weaver, F. A. A phase 3, randomized, double-blind comparative study of the efficacy and safety of topical recombinant human thrombin and bovine thrombin in surgical hemostasis. *J Am Coll of Surg* 2007, 205, 252-265.
10. Palm, M. D.; Altman, J. S. Topical hemostatic agents: A review. *Dermatol Surg* 2008, 34, 431-445.
11. Dunn, C. J.; Goa, K. L. Tranexamic acid. *Drugs* 1999, 57, 1005-1032.
12. O'Connell, K. A.; Wood, J. J.; Wise, R. P.; Lozier, J. N.; Braun, M. M. Thromboembolic adverse events after use of recombinant human coagulation factor VIIa. *Jama* 2006, 295, 293-298.
13. Morrison, J. J.; Stannard, A.; Rasmussen, T. E.; Jansen, J. O.; Tai, N. R. M.; Midwinter, M. J. Injury pattern and mortality of noncompressible torso hemorrhage in UK combat casualties. *J Trauma Acute Care Surg* 2013, 75, S263-S268.
14. Farokhzad, O. C.; Langer, R. Impact of nanotechnology on drug delivery. *ACS Nano* 2009, 3, 16-20.
15. Petros, R. A.; DeSimone, J. M. Strategies in the design of nanoparticles for therapeutic applications. *Nat Rev Drug Discov* 2010, 9, 615-627.
16. Rabinow, B. E. Nanosuspensions in drug delivery. *Nat Rev Drug Discov* 2004, 3, 785-796.
17. Constantinides, P. P.; Chaubal, M. V.; Shorr, R. Advances in lipid nanodispersions for parenteral drug delivery and targeting. *Adv Drug Deliv Rev* 2008, 60, 757-767.

18. Torchilin, V. P. Recent advances with liposomes as pharmaceutical carriers. *Nat Rev Drug Discov* 2005, 4, 145-60.
19. Rosler, A.; Vandermeulen, G. W. M.; Klok, H. A. Advanced drug delivery devices via self-assembly of amphiphilic block copolymers. *Adv Drug Deliv Rev* 2012, 64, 270-279.
20. Discher, D. E.; Ahmed, F. Polymersomes. *Annu Rev Biomed Eng* 2006, 8, 323-41.
21. Harris, J. M.; Chess, R. B. Effect of pegylation on pharmaceuticals. *Nat Rev Drug Discov* 2003, 2, 214-221.
22. Anselmo, A. C.; Mitragotri, S. Nanoparticles in the clinic. *Bioengineering & Transla Med* 2016, 1, 10-29.
23. Barenholz, Y. Doxil (R) - The first FDA-approved nano-drug: Lessons learned. *J Control Release* 2012, 160, 117-134.
24. Ferrari, M. Cancer nanotechnology: Opportunities and challenges. *Nat Rev Cancer* 2005, 5, 161-171.
25. Dashkevich, N. M.; Ovanesov, M. V.; Balandina, A. N.; Karamzin, S. S.; Shestakov, P. I.; Soshitova, N. P.; Tokarev, A. A.; Panteleev, M. A.; Ataulakhanov, F. I. Thrombin Activity Propagates in Space During Blood Coagulation as an Excitation Wave. *Biophys J* 2012, 103, 2233-2240.
26. Anselmo, A. C.; Modery-Pawłowski, C. L.; Menegatti, S.; Kumar, S.; Vogus, D. R.; Tian, L. L.; Chen, M.; Squires, T. M.; Sen Gupta, A.; Mitragotri, S. Platelet-like nanoparticles: mimicking shape, flexibility, and surface biology of platelets to target vascular injuries. *ACS Nano* 2014, 8, 11243-53.
27. Brown, M. R. W.; Kornberg, A. Inorganic polyphosphate in the origin and survival of species. *Proc Natl Acad Sci U.S.A.* 2004, 101, 16085-16087.
28. Kornberg, A. Inorganic Polyphosphate - toward Making a Forgotten Polymer Unforgettable. *J Bacteriol* 1995, 177, 491-496.
29. Kornberg, A.; Rao, N. N.; Ault-Riche, D. Inorganic polyphosphate: A molecule of many functions. *Ann Rev Biochem* 1999, 68, 89-125.
30. Morrissey, J. H.; Choi, S. H.; Smith, S. A. Polyphosphate: an ancient molecule that links platelets, coagulation, and inflammation. *Blood* 2012, 119, 5972-9.
31. Smith, S. A.; Mutch, N. J.; Baskar, D.; Rohloff, P.; Docampo, R.; Morrissey, J. H. Polyphosphate modulates blood coagulation and fibrinolysis. *Proc Natl Acad Sci U S A* 2006, 103, 903-8.
32. Smith, S. A.; Morrissey, J. H. Polyphosphate enhances fibrin clot structure. *Blood* 2008, 112, 2810-6.
33. Smith, S. A.; Choi, S. H.; Davis-Harrison, R.; Huyck, J.; Boettcher, J.; Rienstra, C. M.; Morrissey, J. H. Polyphosphate exerts differential effects on blood clotting, depending on polymer size. *Blood* 2010, 116, 4353-9.
34. Choi, S. H.; Smith, S. A.; Morrissey, J. H. Polyphosphate is a cofactor for the activation of factor XI by thrombin. *Blood* 2011, 118, 6963-70.
35. Pavlov, E.; Aschar-Sobbi, R.; Campanella, M.; Turner, R. J.; Gomez-Garcia, M. R.; Abramov, A. Y. Inorganic Polyphosphate and Energy Metabolism in Mammalian Cells. *J Biol Chem* 2010, 285, 9420-9428.
36. Gray, M. J.; Wholey, W. Y.; Wagner, N. O.; Cremers, C. M.; Mueller-Schickert, A.; Hock, N. T.; Krieger, A. G.; Smith, E. M.; Bender, R. A.; Bardwell, J. C. A.; Jakob, U. Polyphosphate Is a Primordial Chaperone. *Mol Cell* 2014, 53, 689-699.

37. Keasling, J. D. Regulation of intracellular toxic metals and other cations by hydrolysis of polyphosphate. *Bioremediation of Surface and Subsurface Contamination* 1997, 829, 242-249.
38. Docampo, R.; Moreno, S. N. J. Acidocalcisome: A novel Ca^{2+} storage compartment in trypanosomatids and apicomplexan parasites. *Parasitol Today* 1999, 15, 443-448.
39. Docampo, R.; de Souza, W.; Miranda, K.; Rohloff, P.; Moreno, S. N. Acidocalcisomes - conserved from bacteria to man. *Nat Rev Microbiol* 2005, 3, 251-61.
40. Ruiz, F. A.; Lea, C. R.; Oldfield, E.; Docampo, R. Human platelet dense granules contain polyphosphate and are similar to acidocalcisomes of bacteria and unicellular eukaryotes. *J Biol Chem* 2004, 279, 44250-7.
41. Mackman, N.; Tilley, R. E.; Key, N. S. Role of the extrinsic pathway of blood coagulation in hemostasis and thrombosis. *Arterioscler Thromb Vasc Biol* 2007, 27, 1687-1693.
42. Panteleev, M. A.; Balandina, A. N.; Lipets, E. N.; Ovanesov, M. V.; Ataulakhanov, F. I. Task-Oriented Modular Decomposition of Biological Networks: Trigger Mechanism in Blood Coagulation. *Biophys J* 2010, 98, 1751-1761.
43. Seligsohn, U.; Lubetsky, A. Medical progress: Genetic susceptibility to venous thrombosis. *New Engl J Med* 2001, 344, 1222-1231.
44. Franchini, M.; Mannucci, P. M. The hemostatic balance revisited through the lessons of mankind evolution. *Intern Emerg Med* 2008, 3, 3-8.
45. Collet, J. P.; Shuman, H.; Ledger, R. E.; Lee, S. T.; Weisel, J. W. The elasticity of an individual fibrin fiber in a clot. *Proc Natl Acad Sci U.S.A.* 2005, 102, 9133-9137.
46. Davie, E. W.; Ratnoff, O. D. Waterfall sequence for intrinsic blood clotting. *Science* 1964, 145, 1310-1312.
47. Furie, B.; Furie, B. C. The molecular basis of blood coagulation. *Cell* 1988, 53, 505-518.
48. Dahlbäck, B. Blood coagulation. *Lancet* 2000, 355, 1627-1632.
49. Rao, L.; Rapaport, S. I. Activation of factor VII bound to tissue factor: a key early step in the tissue factor pathway of blood coagulation. *Proc Natl Acad Sci U.S.A.* 1988, 85, 6687-6691.
50. Renne, T.; Schmaier, A. H.; Nickel, K. F.; Blomback, M.; Maas, C. In vivo roles of factor XII. *Blood* 2012, 120, 4296-4303.
51. Maas, C.; Oschatz, C.; Renné, T. In *The plasma contact system 2.0*, Seminars in thrombosis and hemostasis, © Thieme Medical Publishers: 2011; pp 375-381.
52. Brummel, K. E.; Paradis, S. G.; Butenas, S.; Mann, K. G. Thrombin functions during tissue factor-induced blood coagulation. *Blood* 2002, 100, 148-152.
53. Krishnaswamy, S.; Jones, K. C.; Mann, K. G. Prothrombinase complex assembly. Kinetic mechanism of enzyme assembly on phospholipid vesicles. *J Biol Chem* 1988, 263, 3823-3834.
54. Pisano, J.; Finlayson, J.; Peyton, M. P. Cross-link in fibrin polymerized by factor XIII: ϵ -(γ -glutamyl) lysine. *Science* 1968, 160, 892-893.
55. Hoffman, M.; Monroe III, D.; Roberts, H. Activated factor VII activates factors IX and X on the surface of activated platelets: thoughts. *Blood Coagulation and Fibrinolysis* 1998, 9, S61-S65.
56. Hedner, U. Recombinant activated factor VII: 30 years of research and innovation. *Blood Reviews* 2015, 29, S4-S8.
57. Nishijima, D. K.; Zehtabchi, S. The efficacy of recombinant activated factor VII in severe trauma. *Ann Emerg Med* 2009, 54, 737-744. e1.
58. Emilia, M.; Luca, S.; Francesca, B.; Luca, B.; Paolo, S.; Giuseppe, F.; Gianbattista, B.; Carmela, M.; Luigi, M.; Mauro, L. Topical hemostatic agents in surgical practice. *Transfus Apher Sci* 2011, 45, 305-311.

59. Brown, J. R.; Birkmeyer, N. J. O.; O'Connor, G. T. Meta-analysis comparing the effectiveness and adverse outcomes of antifibrinolytic agents in cardiac surgery. *Circulation* 2007, 115, 2801-2813.
60. Wiman, B.; Collen, D. Molecular Mechanism of Physiological Fibrinolysis. *Nature* 1978, 272, 549-550.
61. Morrison, J. J.; Dubose, J. J.; Rasmussen, T. E.; Midwinter, M. J. Military application of tranexamic acid in trauma emergency resuscitation (MATTERs) study. *Arch Surg* 2012, 147, 113-119.
62. Horrow, J. C.; Vanriper, D. F.; Strong, M. D.; Brodsky, I.; Parmet, J. L. Hemostatic Effects of Tranexamic Acid and Desmopressin during Cardiac-Surgery. *Circulation* 1991, 84, 2063-2070.
63. Gegel, B.; MSNA, J. B. The effects of QuikClot Combat Gauze and movement on hemorrhage control in a porcine model. *Mil Med* 2012, 177, 1543.
64. Cox, E. D.; Schreiber, M. A.; McManus, J.; Wade, C. E.; Holcomb, J. B. New hemostatic agents in the combat setting. *Transfusion* 2009, 49 Suppl 5, 248S-55S.
65. Rashid, M. H.; Rao, N. N.; Kornberg, A. Inorganic polyphosphate is required for motility of bacterial pathogens. *J Bacteriol* 2000, 182, 225-227.
66. Kim, K. S.; Rao, N. N.; Fraley, C. D.; Kornberg, A. Inorganic polyphosphate is essential for long-term survival and virulence factors in Shigella and Salmonella spp. *Proc Natl Acad Sci U.S.A.* 2002, 99, 7675-7680.
67. Shi, X. B.; Rao, N. N.; Kornberg, A. Inorganic polyphosphate in Bacillus cereus: Motility, biofilm formation, and sporulation. *Proc Natl Acad Sci U.S.A.* 2004, 101, 17061-17065.
68. Docampo, R.; de Souza, W.; Miranda, K.; Rohloff, P.; Moreno, S. N. J. Acidocalcisomes - Conserved from bacteria to man. *Nat Rev Microbiol* 2005, 3, 251-261.
69. Verhoef, J. J.; Barendrecht, A. D.; Nickel, K. F.; Dijkxhoorn, K.; Kenne, E.; Labberton, L.; McCarty, O. J.; Schiffelers, R.; Heijnen, H. F.; Hendrickx, A. P. Polyphosphate nanoparticles on the platelet surface trigger contact system activation. *Blood* 2017, blood-2016-08-734988.
70. Locatelli, E.; Broggi, F.; Ponti, J.; Marmorato, P.; Franchini, F.; Lena, S.; Franchini, M. C. Lipophilic Silver Nanoparticles and Their Polymeric Entrapment into Targeted-PEG-Based Micelles for the Treatment of Glioblastoma. *Adv Healthc Mater* 2012, 1, 342-347.
71. Bangham, A.; Standish, M. M.; Watkins, J. Diffusion of univalent ions across the lamellae of swollen phospholipids. *J Mol Biol* 1965, 13, 238-IN27.
72. Bangham, A. D.; Horne, R. Negative staining of phospholipids and their structural modification by surface-active agents as observed in the electron microscope. *J Mol Biol* 1964, 8, 660IN2-668IN10.
73. Israelachvili, J. N.; Mitchell, D. J.; Ninham, B. W. Theory of self-assembly of lipid bilayers and vesicles. *Biochim Biophys Acta* 1977, 470, 185-201.
74. Allen, T. M. Liposomal drug formulations. *Drugs* 1998, 56, 747-756.
75. Boswell, G.; Buell, D.; Bekersky, I. AmBisome (liposomal amphotericin B): a comparative review. *J Clin Pharmacol* 1998, 38, 583-592.
76. Allen, T. M.; Cullis, P. R. Liposomal drug delivery systems: From concept to clinical applications. *Adv Drug Deliv Rev* 2013, 65, 36-48.
77. Allen, T.; Hansen, C.; Martin, F.; Redemann, C.; Yau-Young, A. Liposomes containing synthetic lipid derivatives of poly (ethylene glycol) show prolonged circulation half-lives in vivo. *Biochim Biophys Acta* 1991, 1066, 29-36.
78. Gordon, S. The macrophage. *Bioessays* 1995, 17, 977-986.

79. Ahsan, F. L.; Rivas, I. P.; Khan, M. A.; Suarez, A. I. T. Targeting to macrophages: role of physicochemical properties of particulate carriers-liposomes and microspheres-on the phagocytosis by macrophages. *J Control Release* 2002, 79, 29-40.
80. Dobrovolskaia, M. A.; McNeil, S. E. Immunological properties of engineered nanomaterials. *Nature Nanotechnol* 2007, 2, 469-478.
81. Martin, F. J.; Papahadjopoulos, D. Irreversible Coupling of Immunoglobulin Fragments to Preformed Vesicles - an Improved Method for Liposome Targeting. *J Biol Chem* 1982, 257, 286-288.
82. Kirpotin, D.; Park, J. W.; Hong, K.; Zalipsky, S.; Li, W. L.; Carter, P.; Benz, C. C.; Papahadjopoulos, D. Sterically stabilized Anti-HER2 immunoliposomes: Design and targeting to human breast cancer cells in vitro. *Biochemistry* 1997, 36, 66-75.
83. Papahadjopoulos, D.; Kirpotin, D. B.; Park, J. W.; Hong, K. L.; Shao, Y.; Shalaby, R.; Colbern, G.; Benz, C. C. Targeting of drugs to solid tumors using anti-HER2 immunoliposomes. *J Liposome Res* 1998, 8, 425-442.
84. Park, J. W.; Kirpotin, D. B.; Hong, K.; Shalaby, R.; Shao, Y.; Nielsen, U. B.; Marks, J. D.; Papahadjopoulos, D.; Benz, C. C. Tumor targeting using anti-her2 immunoliposomes. *J Control Release* 2001, 74, 95-113.
85. Discher, B. M.; Won, Y. Y.; Ege, D. S.; Lee, J. C. M.; Bates, F. S.; Discher, D. E.; Hammer, D. A. Polymersomes: Tough vesicles made from diblock copolymers. *Science* 1999, 284, 1143-1146.
86. Johnson, B. K.; Prud'homme, R. K. Mechanism for rapid self-assembly of block copolymer nanoparticles. *Phys Rev Lett* 2003, 91.
87. Kumari, A.; Yadav, S. K.; Yadav, S. C. Biodegradable polymeric nanoparticles based drug delivery systems. *Colloids Surf B* 2010, 75, 1-18.
88. Nicolas, J.; Mura, S.; Brambilla, D.; Mackiewicz, N.; Couvreur, P. Design, functionalization strategies and biomedical applications of targeted biodegradable/biocompatible polymer-based nanocarriers for drug delivery. *Chem Soc Rev* 2013, 42, 1147-1235.
89. Shen, H.; Hong, S. Y.; Prud'homme, R. K.; Liu, Y. Self-assembling process of flash nanoprecipitation in a multi-inlet vortex mixer to produce drug-loaded polymeric nanoparticles. *J Nanopart Res* 2011, 13, 4109-4120.
90. Egerton, R. F.; Li, P.; Malac, M. Radiation damage in the TEM and SEM. *Micron* 2004, 35, 399-409.
91. Wang, C. H.; Qiao, Q.; Shokuhfar, T.; Klie, R. F. High-Resolution Electron Microscopy and Spectroscopy of Ferritin in Biocompatible Graphene Liquid Cells and Graphene Sandwiches. *Adv Mater* 2014, 26, 3410-3414.
92. Jensen, T. E.; Baxter, M.; Rachlin, J. W.; Jani, V. Uptake of Heavy-Metals by Plectonema-Boryanum (Cyanophyceae) into Cellular-Components, Especially Polyphosphate Bodies - an X-Ray-Energy Dispersive Study. *Environ Pollut A* 1982, 27, 119-127.
93. Holmsen, H.; Weiss, H. J. Secretable Storage Pools in Platelets. *Annu Rev Med* 1979, 30, 119-34.
94. Bonting, C. F. C.; Kortstee, G. J. J.; Boekestein, A.; Zehnder, A. J. B. The Elemental Composition Dynamics of Large Polyphosphate Granules in Acinetobacter Strain 210a. *Arch Microbiol* 1993, 159, 428-434.
95. Monteiro, V. A. D.; de Souza, E. F.; de Azevedo, M. M. M.; Galembeck, F. Aluminum polyphosphate nanoparticles: Preparation, particle size determination, and microchemistry. *J Colloid Interface Sci* 1999, 217, 237-248.

96. Momeni, A.; Filiaggi, M. J. Synthesis and characterization of different chain length sodium polyphosphates. *J Non-Cryst Solids* 2013, 382, 11-17.
97. Momeni, A.; Filiaggi, M. J. Comprehensive Study of the Chelation and Coacervation of Alkaline Earth Metals in the Presence of Sodium Polyphosphate Solution. *Langmuir* 2014, 30, 5256-5266.
98. Einstein, A. A new determination of molecular dimensions. *Ann. Phys* 1906, 19, 289-306.
99. Mui, B.; Chow, L.; Hope, M. J. Extrusion technique to generate liposomes of defined size. *Methods Enzymol* 2002, 367, 3-14.
100. Smith, S. A.; Mutch, N. J.; Baskar, D.; Rohloff, P.; Docampo, R.; Morrissey, J. H. Polyphosphate modulates blood coagulation and fibrinolysis. *P Natl Acad Sci USA* 2006, 103, 903-908.
101. Noda, I.; Takahashi, Y. Viscoelastic Properties of Polyelectrolyte Solutions. *Abstr Pap Am Chem S* 1994, 207, 235-Poly.
102. Sjöholm, I.; Ekman, B.; Kober, A.; Ljungstedt, Pahlman, I.; Seiving, B.; Sjödin, T. Binding of Drugs to Human-Serum Albumin .11. Specificity of 3 Binding-Sites as Studied with Albumin Immobilized in Microparticles. *Mol Pharmacol* 1979, 16, 767-777.
103. Van Slyke, D. D.; Hastings, A. B.; Hiller, A.; Sendroy, J. Studies of Gas and Electrolyte Equilibria in Blood: XIV. The Amounts of Alkali Bound by Serum Albumin and Globulin. *J Biol Chem* 1928, 79, 769-780.
104. Pedersen, K. O. Binding of Calcium to Serum-Albumin .4. Effect of Temperature and Thermodynamics of Calcium-Albumin Interaction. *Scand J Clin Lab Inv* 1972, 30, 89-&.
105. Pedersen, K. O. Binding of Calcium to Serum-Albumin .3. Influence of Ionic-Strength and Ionic Medium. *Scand J Clin Lab Inv* 1972, 29, 427-&.
106. Pedersen, K. O. Binding of Calcium to Serum Albumin .1. Stoichiometry and Intrinsic Association Constant at Physiological Ph, Ionic Strength, and Temperature. *Scand J Clin Lab Inv* 1971, 28, 459-&.
107. Foghandersen, N. Albumin-Calcium Association at Different Ph, as Determined by Potentiometry. *Clin Chem* 1977, 23, 2122-2126.
108. Pedersen, K. O. Binding of Calcium to Serum-Albumin .2. Effect of Ph Via Competitive Hydrogen and Calcium-Ion Binding to Imidazole Groups of Albumin. *Scand J Clin Lab Inv* 1972, 29, 75-&.
109. Masuoka, J.; Saltman, P. Zinc(II) and Copper(II) Binding to Serum-Albumin - a Comparative-Study of Dog, Bovine, and Human Albumin. *J Biol Chem* 1994, 269, 25557-25561.
110. Axelsson, I. Characterization of Proteins and Other Macromolecules by Agarose-Gel Chromatography. *J Chromatogr* 1978, 152, 21-32.
111. Squire, P. G.; Moser, P.; O'Konski, C. T. The hydrodynamic properties of bovine serum albumin monomer and dimer. *Biochemistry-U S* 1968, 7, 4261-72.
112. Ruiz, F. A.; Lea, C. R.; Oldfield, E.; Docampo, R. Human platelet dense granules contain polyphosphate and are similar to acidocalcisomes of bacteria and unicellular eukaryotes. *J Biol Chem* 2004, 279, 44250-44257.
113. Zieve, P. D.; Gamble, J. L., Jr.; Jackson, D. P. Effects of Thrombin on the Potassium and Atp Content of Platelets. *J Clin Invest* 1964, 43, 2063-9.
114. Samuel, M.; Pixley, R. A.; Villanueva, M. A.; Colman, R. W.; Villanueva, G. B. Human Factor-XII (Hageman-Factor) Autoactivation by Dextran Sulfate - Circular-Dichroism, Fluorescence, and Ultraviolet Difference Spectroscopic Studies. *J Biol Chem* 1992, 267, 19691-19697.

115. Corretge, E.; Nigretto, J. M. Molecular Weight-Dependent Contact Activation of Plasma Induced by Soluble Polystyrene and Dextran Derivatives. *Thromb Res* 1990, 59, 463-473.
116. Silverberg, M.; Diehl, S. V. The Autoactivation of Factor-Xii (Hageman-Factor) Induced by Low-Mr Heparin and Dextran Sulfate - the Effect of the Mr of the Activating Polyanion. *Biochem J* 1987, 248, 715-720.
117. Yeon, J. H.; Mazinani, N.; Schlappi, T. S.; Chan, K. Y. T.; Baylis, J. R.; Smith, S. A.; Donovan, A. J.; Kudela, D.; Stucky, G. D.; Liu, Y.; Morrissey, J. H.; Kastrup, C. J. Localization of Short-Chain Polyphosphate Enhances its Ability to Clot Flowing Blood Plasma. *Sci Rep* 2017, 7.
118. Sakariassen, K. S.; Orning, L.; Turitto, V. T. The impact of blood shear rate on arterial thrombus formation. 2015.
119. Sauaia, A.; Moore, F. A.; Moore, E. E.; Moser, K. S.; Brennan, R.; Read, R. A.; Pons, P. T. Epidemiology of trauma deaths: a reassessment. *J Trauma Acute Care Surg* 1995, 38, 185-193.
120. Holcomb, J. B. Methods for improved hemorrhage control. *Crit Care* 2004, 8, S57.
121. Alam, H. B.; Burris, D.; DaCorta, J. A.; Rhee, P. Hemorrhage control in the battlefield: role of new hemostatic agents. *Mil Med* 2005, 170, 63-69.
122. Spahn, D. R.; Cerny, V.; Coats, T. J.; Duranteau, J.; Fernández-Mondéjar, E.; Gordini, G.; Stahel, P. F.; Hunt, B. J.; Komadina, R.; Neugebauer, E. Management of bleeding following major trauma: a European guideline. *Crit Care* 2007, 11, R17.
123. Rossaint, R.; Bouillon, B.; Cerny, V.; Coats, T. J.; Duranteau, J.; Fernández-Mondéjar, E.; Hunt, B. J.; Komadina, R.; Nardi, G.; Neugebauer, E. Management of bleeding following major trauma: an updated European guideline. *Crit Care* 2010, 14, R52.
124. Beekley, A. C. Damage control resuscitation: a sensible approach to the exsanguinating surgical patient. *Crit Care Med* 2008, 36, S267-S274.
125. Murday, J. S.; Siegel, R. W.; Stein, J.; Wright, J. F. Translational nanomedicine: status assessment and opportunities. *Nanomed Nanotech Biol Med* 2009, 5, 251-273.
126. Peer, D.; Karp, J. M.; Hong, S.; Farokhzad, O. C.; Margalit, R.; Langer, R. Nanocarriers as an emerging platform for cancer therapy. *Nat Nanotechnol* 2007, 2, 751-60.
127. Meng, F.; Zhong, Z.; Feijen, J. Stimuli-responsive polymersomes for programmed drug delivery. *Biomacromolecules* 2009, 10, 197-209.
128. Kovacs, E. W.; Hooker, J. M.; Romanini, D. W.; Holder, P. G.; Berry, K. E.; Francis, M. B. Dual-surface-modified bacteriophage MS2 as an ideal scaffold for a viral capsid-based drug delivery system. *Bioconjugate Chem* 2007, 18, 1140-1147.
129. Huh, K. M.; Lee, S. C.; Cho, Y. W.; Lee, J. W.; Jeong, J. H.; Park, K. Hydrotropic polymer micelle system for delivery of paclitaxel. *J Control Release* 2005, 101, 59-68.
130. Gref, R.; Domb, A.; Quéllec, P.; Blunk, T.; Müller, R. H.; Verbavatz, J. M.; Langer, R. The controlled intravenous delivery of drugs using PEG-coated sterically stabilized nanospheres. *Adv Drug Deliv Rev* 2012, 64, 316-326.
131. Jain, R. K.; Stylianopoulos, T. Delivering nanomedicine to solid tumors. *Nat Rev Clin Oncol* 2010, 7, 653-664.
132. Papahadjopoulos, D.; Allen, T. M.; Gabizon, A.; Mayhew, E.; Matthey, K.; Huang, S. K.; Lee, K. D.; Woodle, M. C.; Lasic, D. D.; Redemann, C.; Martin, F. J. Sterically Stabilized Liposomes - Improvements in Pharmacokinetics and Antitumor Therapeutic Efficacy. *Proc Natl Acad Sci U.S.A.* 1991, 88, 11460-11464.

133. Allen, T. M. The Use of Glycolipids and Hydrophilic Polymers in Avoiding Rapid Uptake of Liposomes by the Mononuclear Phagocyte System. *Adv Drug Deliv Rev* 1994, 13, 285-309.
134. Zhou, Z.; Anselmo, A. C.; Mitragotri, S. Synthesis of protein-based, rod-shaped particles from spherical templates using layer-by-layer assembly. *Adv Mater* 2013, 25, 2723-7.
135. Donovan, A. J.; Kalkowski, J.; Smith, S. A.; Morrissey, J. H.; Liu, Y. Size-Controlled Synthesis of Granular Polyphosphate Nanoparticles at Physiologic Salt Concentrations for Blood Clotting. *Biomacromolecules* 2014, 15, 3976-3984.
136. Docampo, R.; Moreno, S. N. Acidocalcisome: A novel Ca^{2+} storage compartment in trypanosomatids and apicomplexan parasites. *Parasitol Today* 1999, 15, 443-8.
137. Muller, F.; Mutch, N. J.; Schenk, W. A.; Smith, S. A.; Esterl, L.; Spronk, H. M.; Schmidbauer, S.; Gahl, W. A.; Morrissey, J. H.; Renne, T. Platelet Polyphosphates Are Proinflammatory and Procoagulant Mediators In Vivo. *Cell* 2009, 139, 1143-1156.
138. Engel, R.; Brain, C. M.; Paget, J.; Lionikiene, A. S.; Mutch, N. J. Single-chain factor XII exhibits activity when complexed to polyphosphate. *J Thromb Haemost* 2014, 12, 1513-22.
139. Egerton, R. F. *Electron Energy-Loss Spectroscopy in the Electron Microscope*. Springer: 2011.
140. Wu, J. S.; Kim, A. M.; Bleher, R.; Myers, B. D.; Marvin, R. G.; Inada, H.; Nakamura, K.; Zhang, X. F.; Roth, E.; Li, S. Y.; Woodruff, T. K.; O'Halloran, T. V.; Dravid, V. P. Imaging and elemental mapping of biological specimens with a dual-EDS dedicated scanning transmission electron microscope. *Ultramicroscopy* 2013, 128, 24-31.
141. Park, J.; Park, H.; Ercius, P.; Pegoraro, A. F.; Xu, C.; Kim, J. W.; Han, S. H.; Weitz, D. A. Direct Observation of Wet Biological Samples by Graphene Liquid Cell Transmission Electron Microscopy. *Nano Lett* 2015, 15, 4737-44.
142. Wojcik, M.; Hauser, M.; Li, W.; Moon, S.; Xu, K. Graphene-enabled electron microscopy and correlated super-resolution microscopy of wet cells. *Nat Commun* 2015, 6, 7384.
143. Chen, Q.; Smith, J. M.; Park, J.; Kim, K.; Ho, D.; Rasool, H. I.; Zettl, A.; Alivisatos, A. P. 3D motion of DNA-Au nanoconjugates in graphene liquid cell electron microscopy. *Nano Lett* 2013, 13, 4556-61.
144. Chen, Q.; Smith, J. M.; Rasool, H. I.; Zettl, A.; Alivisatos, A. P. Studies of the dynamics of biological macromolecules using Au nanoparticle-DNA artificial molecules. *Faraday Discuss* 2014, 175, 203-14.
145. Kashyap, S.; Woehl, T. J.; Liu, X.; Mallapragada, S. K.; Prozorov, T. Nucleation of iron oxide nanoparticles mediated by Mms6 protein in situ. *ACS Nano* 2014, 8, 9097-106.
146. Favron, A.; Gaufrès, E.; Fossard, F.; Lévesque, P.; Phaneuf-L'Heureux, A.; Tang, N.; Loiseau, A.; Leonelli, R.; Francoeur, S.; Martel, R. Exfoliating pristine black phosphorus down to the monolayer: photo-oxidation and electronic confinement effects. *arXiv preprint arXiv:1408.0345* 2014.
147. Broos, K.; Feys, H. B.; De Meyer, S. F.; Vanhoorelbeke, K.; Deckmyn, H. Platelets at work in primary hemostasis. *Blood Rev* 2011, 25, 155-167.
148. Coughlin, S. R. Sol Sherry lecture in thrombosis: how thrombin 'talks' to cells: molecular mechanisms and roles in vivo. *Arterioscler Thromb Vasc Biol* 1998, 18, 514-8.
149. Coughlin, S. R. Thrombin signalling and protease-activated receptors. *Nature* 2000, 407, 258-64.
150. Furie, B.; Furie, B. C. Mechanisms of thrombus formation. *N Engl J Med* 2008, 359, 938-49.

151. Brass, L. F.; Shaller, C. C.; Belmonte, E. J. Inositol 1,4,5-Triphosphate-Induced Granule Secretion in Platelets - Evidence That the Activation of Phospholipase-C Mediated by Platelet Thromboxane Receptors Involves a Guanine-Nucleotide Binding Protein-Dependent Mechanism Distinct from That of Thrombin. *J Clin Invest* 1987, 79, 1269-1275.
152. Flaumenhaft, R. Molecular basis of platelet granule secretion. *Arterioscler Thromb Vasc Biol* 2003, 23, 1152-1160.
153. Taylor, S. J.; Chae, H. Z.; Rhee, S. G.; Exton, J. H. Activation of the beta 1 isozyme of phospholipase C by alpha subunits of the Gq class of G proteins. *Nature* 1991, 350, 516-8.
154. Rittenhouse-Simmons, S. Production of diglyceride from phosphatidylinositol in activated human platelets. *J Clin Invest* 1979, 63, 580-7.
155. Titball, R. W. Bacterial phospholipases. *J Appl Microbiol* 1998, 84, 127s-137s.
156. Roberts, M. F.; Otnaess, A. B.; Kensil, C. A.; Dennis, E. A. The specificity of phospholipase A2 and phospholipase C in a mixed micellar system. *J Biol Chem* 1978, 253, 1252-7.
157. Nevalainen, T. J.; Haapamaki, M. M.; Gronroos, J. M. Roles of secretory phospholipases A(2) in inflammatory diseases and trauma. *Biochim Biophys Acta* 2000, 1488, 83-90.
158. Jorgensen, K.; Davidsen, J.; Mouritsen, O. G. Biophysical mechanisms of phospholipase A2 activation and their use in liposome-based drug delivery. *FEBS Lett* 2002, 531, 23-7.
159. Majewski, J.; Kuhl, T.; Gerstenberg, M.; Israelachvili, J.; Smith, G. Structure of phospholipid monolayers containing poly (ethylene glycol) lipids at the air-water interface. *The J Phys Chem B* 1997, 101, 3122-3129.
160. Bernardo, M. M.; Day, D. E.; Olson, S. T.; Shore, J. D. Surface-Independent Acceleration of Factor-Xii Activation by Zinc Ions .1. Kinetic Characterization of the Metal-Ion Rate Enhancement. *J Biol Chem* 1993, 268, 12468-12476.
161. Bernardo, M. M.; Day, D. E.; Halvorson, H. R.; Olson, S. T.; Shore, J. D. Surface-Independent Acceleration of Factor-Xii Activation by Zinc Ions .2. Direct Binding and Fluorescence Studies. *J Biol Chem* 1993, 268, 12477-12483.
162. Bock, P. E.; Srinivasan, K. R.; Shore, J. D. Activation of intrinsic blood coagulation by ellagic acid: insoluble ellagic acid-metal ion complexes are the activating species. *Biochemistry* 1981, 20, 7258-66.
163. Choi, S. H.; Collins, J. N.; Smith, S. A.; Davis-Harrison, R. L.; Rienstra, C. M.; Morrissey, J. H. Phosphoramidate end labeling of inorganic polyphosphates: facile manipulation of polyphosphate for investigating and modulating its biological activities. *Biochemistry* 2010, 49, 9935-41.
164. Browne, W. R.; Feringa, B. L. Making molecular machines work. *Nature Nanotechnology* 2006, 1, 25-35.
165. Hartl, F. U.; Hayer-Hartl, M. Converging concepts of protein folding in vitro and in vivo. *Nat Struct Mol Biol* 2009, 16, 574-581.
166. Dill, K. A.; MacCallum, J. L. The Protein-Folding Problem, 50 Years On. *Science* 2012, 338, 1042-1046.
167. Rossky, P. J. Protein denaturation by urea: Slash and bond. *Proc Natl Acad Sci U.S.A.* 2008, 105, 16825-16826.
168. Morimoto, R. I. Cells in stress: transcriptional activation of heat shock genes. *Science* 1993, 259, 1409-1409.
169. Jakob, U.; Gaestel, M.; Engel, K.; Buchner, J. Small Heat-Shock Proteins Are Molecular Chaperones. *J Biol Chem* 1993, 268, 1517-1520.

170. Hartl, F. U.; Bracher, A.; Hayer-Hartl, M. Molecular chaperones in protein folding and proteostasis. *Nature* 2011, 475, 324-332.
171. Diamant, S.; Eliahu, N.; Rosenthal, D.; Goloubinoff, P. Chemical chaperones regulate molecular chaperones in vitro and in cells under combined salt and heat stresses. *J Biol Chem* 2001, 276, 39586-39591.
172. Terraube, V.; O'Donnell, J. S.; Jenkins, P. V. Factor VIII and von Willebrand factor interaction: biological, clinical and therapeutic importance. *Haemophilia* 2010, 16, 3-13.
173. Zimmerman, B.; Valentino, L. A. Hemophilia: in review. *Pediatr Rev* 2013, 34, 289-294.
174. Gilbert, G. E.; Furie, B. C.; Furie, B. Binding of human factor VIII to phospholipid vesicles. *J Biol Chem* 1990, 265, 815-822.
175. Foster, P. A.; Fulcher, C. A.; Houghten, R. A.; Zimmerman, T. S. Synthetic Factor-Viii Peptides with Amino-Acid-Sequences Contained within the C2 Domain of Factor-Viii Inhibit Factor-Viii Binding to Phosphatidylserine. *Blood* 1990, 75, 1999-2004.
176. Anraku, Y.; Kishimura, A.; Oba, M.; Yamasaki, Y.; Kataoka, K. Spontaneous formation of nanosized unilamellar polyion complex vesicles with tunable size and properties. *J Am Chem Soc* 2010, 132, 1631-1636.
177. Black, K. A.; Priftis, D.; Perry, S. L.; Yip, J.; Byun, W. Y.; Tirrell, M. Protein Encapsulation via Polypeptide Complex Coacervation. *ACS Macro Lett* 2014, 3, 1088-1091.
178. Overbeek, J. T. G.; Voorn, M. Phase separation in polyelectrolyte solutions. Theory of complex coacervation. *J Cell Physio* 1957, 49, 7-26.
179. Priftis, D.; Tirrell, M. Phase behaviour and complex coacervation of aqueous polypeptide solutions. *Soft Matter* 2012, 8, 9396-9405.
180. Szymusiak, M.; Donovan, A. J.; Smith, S. A.; Ransom, R.; Shen, H.; Kalkowski, J.; Morrissey, J. H.; Liu, Y. Colloidal Confinement of Polyphosphate on Gold Nanoparticles Robustly Activates the Contact Pathway of Blood Coagulation. *Bioconjugate Chem* 2016, 27, 102-109.
181. Gregoriadis, G. Engineering liposomes for drug delivery: progress and problems. *Trends Biotechnol* 1995, 13, 527-537.
182. Webb, M. S.; Harasym, T. O.; Masin, D.; Bally, M. B.; Mayer, L. D. Sphingomyelin-Cholesterol Liposomes Significantly Enhance the Pharmacokinetic and Therapeutic Properties of Vincristine in Murine and Human Tumor-Models. *Br J Cancer* 1995, 72, 896-904.
183. Zucker, D.; Marcus, D.; Barenholz, Y.; Goldblum, A. Liposome drugs' loading efficiency: A working model based on loading conditions and drug's physicochemical properties. *J Control Release* 2009, 139, 73-80.
184. Michelson, A. D.; Barnard, M. R.; Krueger, L. A.; Valeri, C. R.; Furman, M. I. Circulating monocyte-platelet aggregates are a more sensitive marker of in vivo platelet activation than platelet surface P-selectin - Studies in baboons, human coronary intervention, and human acute myocardial infarction. *Circulation* 2001, 104, 1533-1537.
185. Wolberg, A. S. Thrombin generation and fibrin clot structure. *Blood Rev* 2007, 21, 131-142.
186. Saelman, E. U. M.; Nieuwenhuis, H. K.; Hese, K. M.; Degroot, P. G.; Heijnen, H. F. G.; Sage, E. H.; Williams, S.; Mckeown, L.; Gralnick, H. R.; Sixma, J. J. Platelet-Adhesion to Collagen Type-I through Type-Viii under Conditions of Stasis and Flow Is Mediated by Gpia/Iia (Alpha(2)Beta(1)-Integrin). *Blood* 1994, 83, 1244-1250.
187. Tagawa, T.; Awane, K.; Nagaike, K. Phospholipid derivatized with PEG bifunctional linker and liposome containing it. Google Patents: 1996.

188. Kung, V. T.; Redemann, C. T. Protein-liposome conjugates. Google Patents: 1988.
189. Ruggeri, Z. M. von Willebrand factor and fibrinogen. *Curr Opin Cell Biol* 1993, 5, 898-906.
190. Modery-Pawlowski, C. L.; Tian, L. L.; Pan, V.; McCrae, K. R.; Mitragotri, S.; Sen Gupta, A. Approaches to synthetic platelet analogs. *Biomaterials* 2013, 34, 526-541.
191. Schlimp, C. J.; Khadem, A.; Klotz, A.; Solomon, C.; Hochleitner, G.; Ponschab, M.; Redl, H.; Schochl, H. Rapid measurement of fibrinogen concentration in whole blood using a steel ball coagulometer. *J Trauma Acute Care Surg* 2015, 78, 830-836.
192. Hauser, C. J. Preclinical models of traumatic, hemorrhagic shock. *Shock* 2005, 24, 24-32.
193. Vilahur, G.; Padro, T.; Badimon, L. Atherosclerosis and thrombosis: insights from large animal models. *BioMed Res Int* 2011, 2011.
194. Jordan, S. W.; Haller, C. A.; Sallach, R. E.; Apkarian, R. P.; Hanson, S. R.; Chaikof, E. L. The effect of a recombinant elastin-mimetic coating of an ePTFE prosthesis on acute thrombogenicity in a baboon arteriovenous shunt. *Biomaterials* 2007, 28, 1191-1197.